# DEVELOPMENT OF LOW DIMENSIONAL COBALT-IRON BASED HEUSLER ALLOY SYSTEMS FOR MAGNETIC AND MAGNETO-OPTICAL APPLICATIONS

**MD REJAUL KARIM**

*A thesis submitted for the partial fulfillment of*
*the degree of Doctor of Philosophy*

Institute of Nano Science and Technology
Knowledge City, Sector 81, SAS Nagar, Manauli PO, Mohali 140306, Punjab, India

Indian Institute of Science Education and Research
Knowledge city, Sector 81, SAS Nagar, Manauli PO, Mohali 140306, Punjab, India

March 2022

**Dedicated to my parents and Grandmother**

# Declaration

The work presented in this thesis has been carried out by me under the guidance of Dr. Indranil Sarkar at the Institute of Nano Science and Technology, Mohali. This work has not been submitted in part or in full for a degree, a diploma, or a fellowship to any other university or institute. Whenever contributions of others are involved, every effort is made to indicate this clearly, with due acknowledgement of collaborative research and discussions. This thesis is a bona fide record of original work done by me and all sources listed within have been detailed in the bibliography.

Md Rejaul Karim

In my capacity as the supervisor of the candidate's thesis work, I certify that the above statements by the candidate are true to the best of my knowledge.

Dr. Indranil Sarkar

# Acknowledgements

Where the mind is without fear and the head is held high
Where knowledge is free
Where the world has not been broken up into fragments
By narrow domestic walls
Where words come out from the depth of truth

**-Rabindranath Tagore (Nobel Prize in Literature)**

First and foremost I would like to thank Almighty Allah, the Lord of the Universe, who showered the gracious blessings upon me and gave me the ardor and strength to complete this work.

I would like to take this opportunity to express my deepest gratitude and sincere thanks to my Ph.D. supervisor **Dr. Indranil Sarkar** (Scientist-E, Institute of Nano Science and Technology, Mohali, Punjab, India) for guiding me and showing me the right direction to achieve my goals. I am very lucky and privileged that I am his first Ph.D. student. His insightful understanding and vast knowledge about the subject along with the scientific approach to tackle the research problems have always provided me a constant source of encouragement. I cannot forget his persistent efforts and guidance from day one at INST till date. He has always stood by my side in my odd and even situations. I will be grateful to him for always understanding the critical situations and providing sustained encouragement. Once again, I would like to thank him from the core of my heart for always being so supportive and having faith in me.

I also would like to acknowledge my Ph.D. committee members Prof. Abir De Sarkar and Dr. Sanyasinaidu Boddu for their time and valuable suggestions during the evaluation of my work progress. I also want to thank Dr. Subhendu Sarkar (Scientist, IIT Ropar) for evaluating my SRF presentation and providing useful suggestion to improve my work.

I would like to thank our collaborators, Prof. Anjan Barman, A. Adhikari, S. N. Panda (Department of Condensed Matter Physics and Material Sciences, S. N. Bose National Centre for Basic Sciences, Kolkata), Prof. Subhankar Bedanta, P. Sharangi (School of Physical Sciences, NISER, Bhubaneswar), Prof. Sajal Ghosh from Shiv Nadar University, Tehsil Dadri, UP and Prof. P. S. Anil Kumar, S. Kayal from Department of Physics, Indian Institute of Science, Bangalore.

I would sincerely thank Prof. Amitava Patra, The Director, INST for making a great working atmosphere and all the facilities required to complete this thesis work. I would extend my gratitude to our founding director Prof. A. K. Ganguli and former acting director Prof. H. N. Ghosh for their support.

I would like to give my special thanks to all SHaPED lab group members. I am grateful to all the present members such as Debasish, Priyanka, Kirana, Yash and former members Arindam, Sourav, Suman, and Madhur for their support and constant cooperation during my Ph.D. journey.

Friends are an integral part of life and in the last four years, I was always in close contact with four of my best friends Manisha, Raihan, Ritika, and Varun. We call our group as ‘Mad Bunch’. We have spent a lot of time together, we partied together, and we always cared for each other. I thank all of them for making my stay so easy and memorable.

I would further like to thank my Qaum brothers from INST, Dr. Bilal, Dr. Naimat, Dr. Tarik, Dr. Anas, Dr. Arif, Selim, Atikur, Khalid, Mujib, Nadim, Aneesh, Aquib, Farhan Bhai, Zubair, Kashif, Naushad, Shumile, Afsan.

I owe a deep sense of gratitude to my AMU friends, including Dr. Riyaj, Dr. Shahariar, Batin, Sher Alam, Ruhul, and Dr. Ramiz, with whom I have spent a great and memorable days of my life.

I am also thankful to my classmates from INST, Ashish, Anamika, Hari, Himadri, Ayushi, Manish, Chirag, and many others.

I would further like to extend my sincere gratitude towards my seniors, Navpreet, Rohit, Nandan, Deepika, Krishna, Navneet, Sunaina, Ravi, Dr. Dipanjan, Dr. Dipankar, and others.

I am also grateful to my juniors such as, Tashmeen for hyperthermia measurements, Tapaswini, Akash, Vikas, KK, Shikha, Mridu, Zinia, Vidya.

Apart from friends at INST, I am very grateful to my childhood friends, Mukter, Rakim, Mokim, Milton. I am also thankful to my schoolmates, Kaji, Ajmal, Mehebub, Moni, Albiruni, Sabir, Linkon, Chinmoy, Suchi, Priya, Mijanur, and many more.

I am also grateful to all the non-teaching staff, including Ms. Reena, Mrs. Gurveen Mr. Vikram, Mr. Deepak, and security staff members.

Last but definitely not the least, my deep and sincere gratitude to my family for their continuous and infinite love and support, which always counts as my strength. It is due to their unconditional trust and faith in me that has inspired me to reach this position. I would like to express my gratitude and love towards my parents, **Mr. Abdul Matin** and **Mrs. Mashuda Bibi** for letting me achieve my goals. This degree is theirs as much as it is mine. I don’t have words to thank my siblings, Mojaffar, Segufa, Nilufa and my niece Jarin, Rifat for their moral support, togetherness and love. I will be always indebted to my Nanu (Mr. Yasin Sahab), who always taught me to help others and practice humanity. I hereby, want to acknowledge my brother-in-law (Mr. Soriful), for so much love and care for me and my family since his arrival to our family.

Finally, I would like to thank, all those people whose names I missed here, despite their unconditional love and support to make my journey successful. Thank you all for being there as blessings. Indeed, it was a wonderful journey.

**Md Rejaul Karim**

# Table of Contents

# List of Figures

# List of Tables

# Abstract

Heusler alloy (HA) materials are an extremely important class of magnetic material that are expected to have a wide range of spintronics or spin based electronics applications such as, in magnetic recording medium, in thermoelectricity, magneto-optical device applications, shape memory alloy etc. In this thesis, we have worked towards development of $Co_2Fe$-based HAs thin films and nanocrystals using novel growth schemes. $Co_2Fe$-based HAs are an exciting Heusler class of materials having high magnetic ordering temperature, with capability to support large spin polarization current and are also predicted to exhibit interesting topological properties. This thesis presents new approaches towards alternative methods beyond conventional techniques to grow HA nanostructures. The thesis further presents evaluation and understanding of the magnetic properties of these HA nanostructures for magneto-optical and magneto thermal applications. The deposited films show a large degree of magneto-optical Kerr rotation as well as high saturation magnetization at room temperature. The Kerr measurements show rotation reaching up to a maximum value of $\approx 0.3°$ on polycrystalline copper substrate and $\approx 0.8°$ on a single crystalline platinum substrate which is comparable with the films grown by conventional techniques. Using Kerr microscopy studies we understand the formation and evolution of the magnetic domains in these electrodeposited films. Through these studies we develop an understanding of surface magnetization reversal in the electrodeposited films. The static MOKE measurements also reveal that electrodeposited samples possess strong uniaxial magneto-crystalline anisotropy which is very important for device applications. Furthermore, angle dependent MOKE measurements reveal a two-fold symmetry in the electrodeposited $Co_2FeSn$ films that can be expected in highly ordered crystalline Heusler alloy phase. We also synthesized highly B2 ordered $Co_2FeSn$ and $L2_1$ ordered $Co_2FeAl$ HA nanocrystals. These studies show the possibility of growing highly crystalline and well-ordered Heusler nanoparticles. The structural optimization is found to lead to improved magnetic properties for both cases. Magneto thermal measurements under oscillating magnetic field show that these Heusler nanoparticles are capable of generating heat that can be useful for hyperthermia studies.

# List of Abbreviations

| | |
|---|---|
| AMR | Anisotropic magnetoresistance |
| AF | Antiferromagnetic |
| DOS | Density of states |
| FMR | Ferromagnetic resonance |
| AFM | Atomic force microscopy |
| AC | Alternating current |
| DC | Direct current |
| PMA | Perpendicular magnetic anisotropy |
| DW | Domain wall |
| EA | Easy axis |
| EDX | Energy-dispersive X-ray |
| SAR | Specific absorption rate |
| FC | Field cooling (Cooled) |
| ZFC | Zero field cooling |
| FM | Ferromagnetic |
| HA | Hard axis |
| FTIR | Fourier Transform Infrared |
| XRD | X-ray Diffraction |
| TEM | Transmission electron microscopy |
| $H$ / $H_{ext}$ | External magnetic field |
| $H_C$ | Coercive field |
| $H_K$ | Anisotropy field |
| MOKE | Magneto optical Kerr effect |

| | |
|---|---|
| SEM | Scanning electron microscopy |
| TR-MOKE | Time resolved magneto optical Kerr effect |
| $M_R$ | Remanent magnetization |
| $M_S$ | Saturation magnetization |
| NPs | Nanoparticles |
| SAED | Selected area electron diffraction pattern |
| MHT | Magnetic hyperthermia therapy |
| HRTEM | High resolution transmission electron microscopy |
| MFM | Magnetic force microscopy |
| $K_S$ | Surface anisotropy constant |
| XPS | X-ray photoelectron spectroscopy |
| VSM | Vibrating sample magnetometer |
| $K_V$ | Volume anisotropy constant |
| M | Magnetization |
| eV | Electron-volt |
| $K_B$ | Boltzmann constant |
| RT | Room temperature |
| $\alpha$ | Gilbert damping coefficient |
| VESTA | Visualization of electronic and structural analysis |
| GIXRD | Grazing incident X-ray diffraction |
| KPFM | Kelvin probe force microscopy |
| d | Inter-planar distances |
| K / $K_{eff}$ | Total / effective anisotropy constant |
| Å | Angstrom |
| $T_C$ | Curie temperature |
| h | Plank’s constant |
| JCPDS | Joint Committee on Powder Diffraction Standards |

| | |
|---|---|
| HMF | Half-metallic ferromagnet |
| $K_4$ | Cubic / four-fold anisotropy constant |
| $K_2$ | Uniaxial / two-fold anisotropy constant |
| Pd | Palladium |
| Pt | Platinum |
| LLG | Landau-Lifshitz-Gilbert |
| SQUID | Superconducting Quantum Interference Device |
| MTJ | Magnetic tunnel junction |
| AMF | Alternating magnetic field |
| TF | Thin film |
| LCP | Left- circularly polarized |
| RCP | Right- circularly polarized |
| RF | Radio frequency |

# Chapter 1

# Introduction to Heusler alloys and their Properties

In this chapter, the background of Heusler alloy, their types, and properties along with different applications has been discussed. The application of Heusler alloy in the field of spintronics, thermoelectricity, shape memory alloy, and magneto-optical devices are also being reviewed. The importance of cobalt iron based Heusler alloys and challenges in growing their thin films and nanostructures, especially for those that are thermodynamically difficult to prepare is introduced. Finally an overview of the thesis work is presented by briefly introducing the various chapters of this thesis.

## 1.1 Background of Heusler alloy:

Since the discovery of a new class of intermetallic material by Friedrich Heusler [1] in 1903, research in this field has strongly developed because of their interesting electronic, optical, magnetic, magneto-optical properties. Heusler compounds are multifunctional magnetic materials and have been extensively studied due to their potential spintronics applications. The first Heusler alloy was a mixture of three non-magnetic metal Cu, Mn and Al (formula- $Cu_2MnAl$) [2]. Depending upon the stoichiometric ratio, there could be two types of Heusler alloys, Half Heusler (XYZ) and Full Heusler alloys ($X_2YZ$) where, X, Y are the transition metal elements and Z belongs to sp elements group of the periodic table.

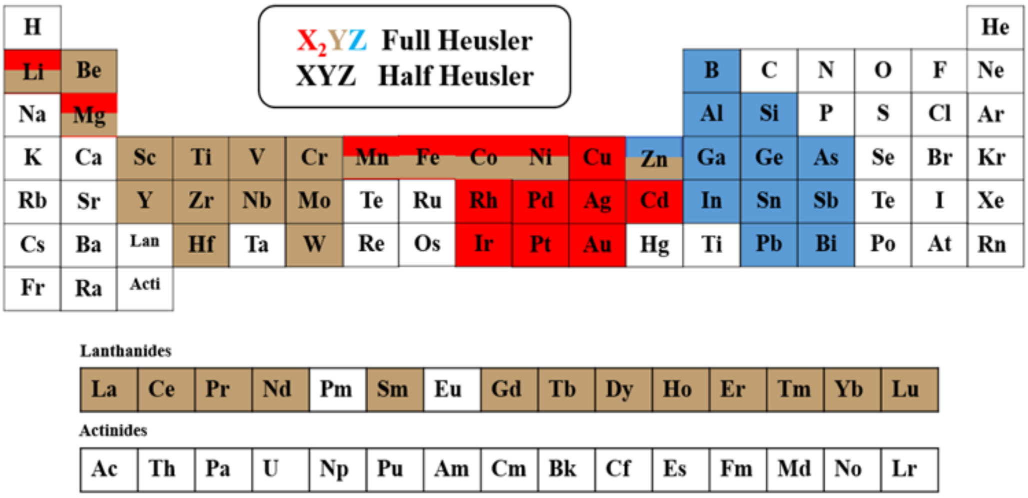

***Figure 1.1:*** *The periodic table showing the X, Y, Z components for the formation of Heusler alloy.*

From the periodic table (Fig. 1.1), it is clear that an enormous number of Heusler alloys can be designed but unfortunately not all of them are stable. The first Heusler alloy was ferromagnetic at room temperature, but later on, it was found that those alloys could exhibit antiferromagnetic [3,4], paramagnetic [5], ferrimagnetic [6,7] as well. Those alloys have wide applications including topological insulators [8,9] superconductivity [10,11], magneto-calorics [12,13], magnetic-tunnel junctions [14], thermo-electrics [15,16]. The detail application of Heusler alloy will be discussed in the later part of this chapter.

## 1.2 Different properties of Heusler alloy:

### 1.2.1 Crystal structure of Heusler alloys

There are over 2000 known compositions of Heusler alloy and those alloys can be semiconductors, ferromagnets, half-metallic ferromagnets, superconductors, shape memory alloys etc. After the discovery of Heusler alloy in 1903, its crystal structure was unknown for a long duration because X-ray diffraction of crystalline structure was not discovered at that time. It took several decades to understand the crystal structure of Heusler alloy. In 1934, O. Heusler [17], son of F. Heusler was the first to determine the crystal lattice of this type of compound. Heusler alloy consists of four interpenetrating face-cantered cubic (fcc) lattices. In the same year, A.J. Bradley and J.W. Rodgers also proved that indeed Heusler alloy consists of four interpenetrating face-cantered cubic (fcc) lattices [18]**.**

The physical properties and electronic structure of Heusler alloys heavily depend on their degree and type of crystal structures. The Heusler materials family is basically divided into 2 large subclasses: half-Heusler compounds (XYZ) and full Heusler compounds ($X_2YZ$). The full Heusler ($X_2YZ$) and half-Heusler (XYZ) alloy crystal structures are shown in figure 1.2. Full Heusler alloy consists of four interpenetrating fcc sublattices in which two are equally occupied by X atoms. The unit cell contains total eight cubes with four X atoms at its centre while Y and Z atoms sit at the corner so the lattice constituents 4 interpenetrating sublattices. Generally, full Heusler $X_2YZ$ compound crystallizes in the cubic $Cu_2MnAl$ structure (space group no. 225: $Fm\bar{3}m$, $L2_1$) with 2:1:1 stoichiometry [19–21]. The most electronegative transition metal X occupy Wyckoff position 8c (1/4, 1/4, 1/4), less electronegative transition metal Y atom occupying the 4b (1/2, 1/2, 1/2) while the non-magnetic main group element Z occupies the 4a (0, 0, 0) Wyckoff position. This crystal structure is generally called as $L2_1$ cubic structure which is considered as a highly ordered structure for a full Heusler alloy material. On the other hand, the non-centrosymmetric cubic structure so called half-Heusler alloy (space group no. 216, $F\bar{4}3m$, $C1_b$) with formula XYZ has 1:1:1 stoichiometry. The half-Heusler lattice can be visualized as three interpenetrating fcc sublattices. The Z atom occupies the 4a (0, 0, 0) Wyckoff position, the Y atom occupying the 4b (1/2, 1/2, 1/2) position and X atom occupy Wyckoff position 4c (1/4, 1/4, 1/4).

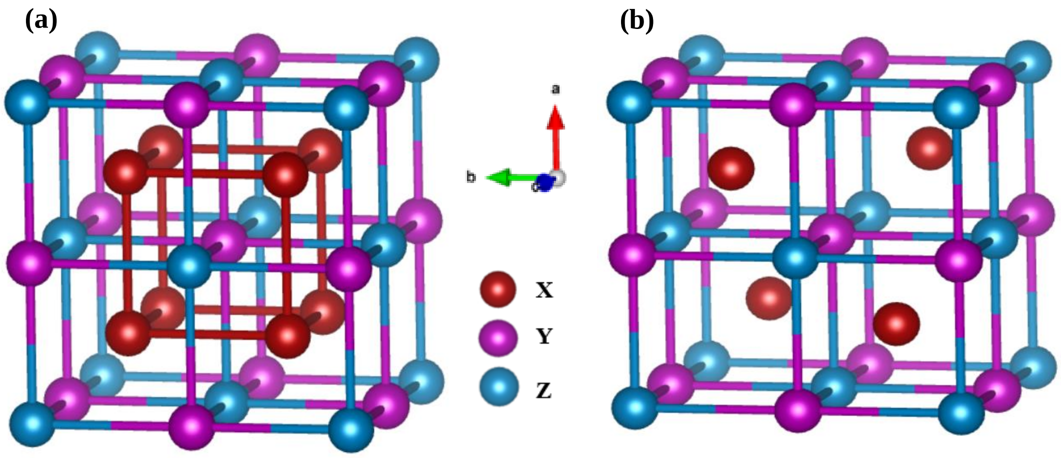

***Figure 1.2:*** *Depiction of the crystal structures of (a) cubic full-Heusler,* $X_2YZ$ *and (b) cubic half Heusler, XYZ compounds described in the face-cantered cubic space groups* $Fm\bar{3}m$ *and* $F\bar{4}3m$ *respectively.*

There are two more types of Heusler alloy, one is inverse Heusler alloy and another one is quaternary Heusler alloy. Figure 1.3 (a-b) shows the crystal structure of inverse and quaternary Heusler alloy, respectively. The $CuHg_2Ti$-type inverse-Heusler alloy has space group $F\bar{4}3m$ similar to the half-Heusler crystal structure and it has the 2:1:1 stoichiometry like the full Heusler. In this structure, X atoms only change the Wyckoff position. The Wyckoff positions of atoms are similar to the half-Heusler alloy where X atom sits at 4c (1/4, 1/4, 1/4) and the Y atom occupy 4d (3/4, 3/4, 3/4) position and 4b (1/2, 1/2, 1/2) Wyckoff position and the Z atom at 4a (0, 0, 0) Wyckoff position.

The prototype of LiMgPdSn (XX′YZ, space group $F\bar{4}3m$, space group no. 216) structure, generally known as quaternary Heusler alloy [22–24] shown in figure 1.3-b. The quaternary Heusler structure has no inversion symmetry and is called Y-type structure. In this structure, the Wyckoff positions are 4c (1/4, 1/4, 1/4), 4d (3/4, 3/4, 3/4), 4b (1/2, 1/2, 1/2) and 4a (0, 0, 0) for X, X′, Y and Z atoms respectively. Figure 1.4 shows how the different Heusler alloys can transform from each other depending upon the addition, substitution or exchange of different elements.

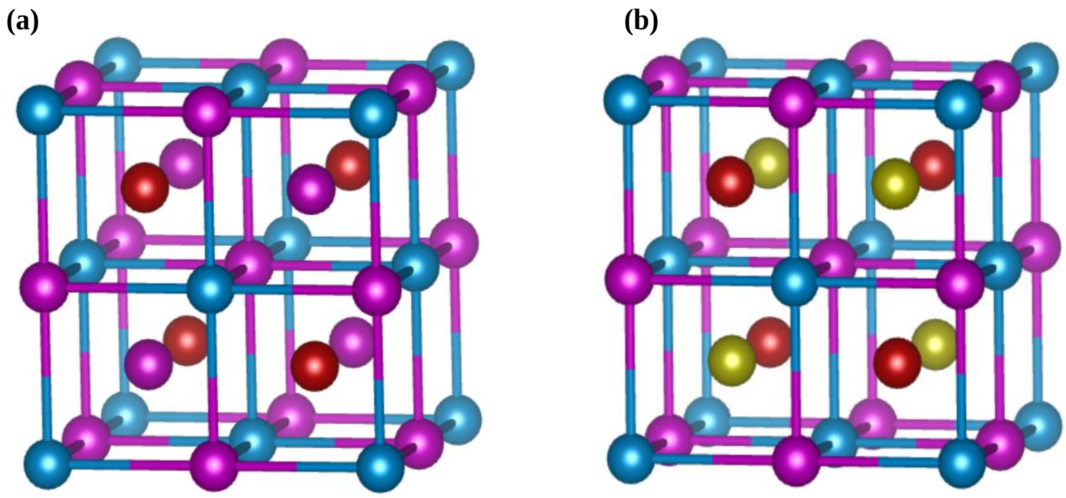

***Figure 1.3:*** *The crystal structures of (c) Inverse Heusler,* $XY_2Z$ *and (d) Quaternary Heusler, XX'YZ compounds.*

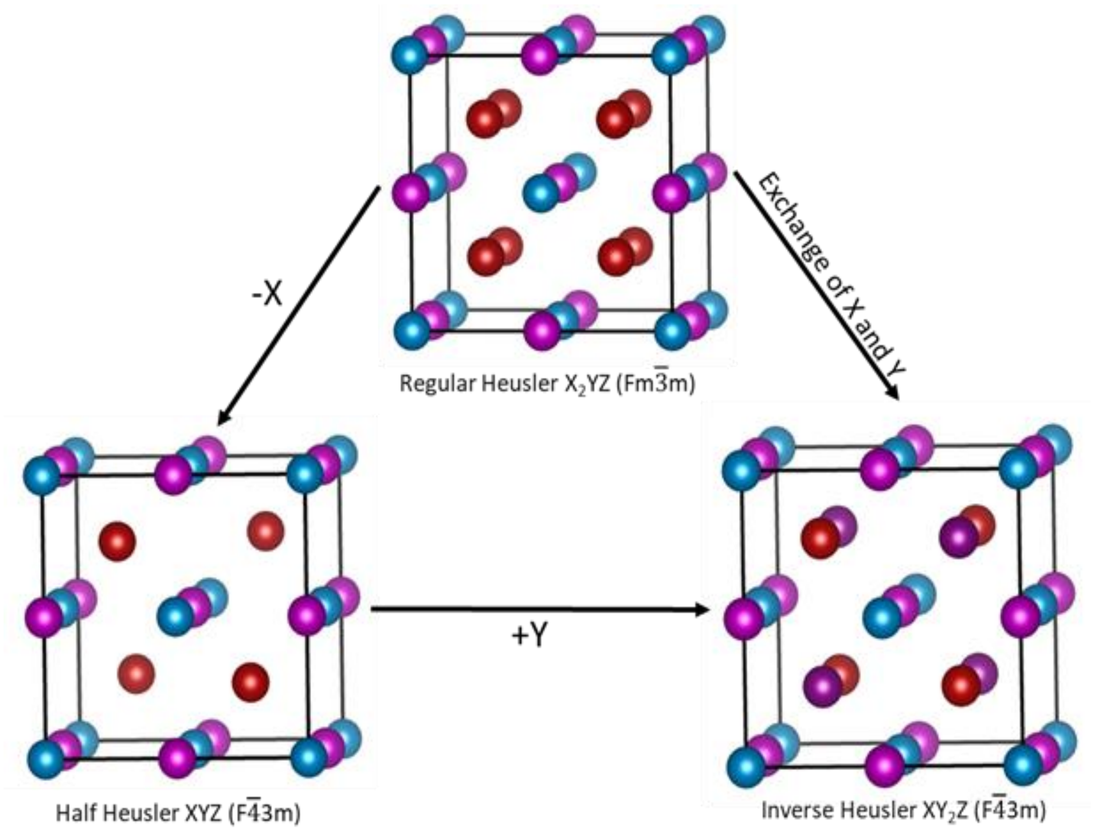

***Figure 1.4:*** *The transformation of different Heusler alloys depending on the exchange of X, Y and Z elements.*

### 1.2.2 Types of chemical disorders in crystal structure of Heusler alloys

Based on different atom positions, various types of site disorders have been observed in Heusler alloys. The most ordered structure $L2_1$, partially ordered B2, $DO_3$ and fully disordered A2 are shown in figure 1.5. For the B2 disorder structure, a small degree of half-metallic properties are maintained but for A2 and $DO_3$ disorder structures the half-metallic behavior is destroyed [25]. The atomic disorder also heavily affects different properties of alloys such as the electronic, structural, magnetic, and transport properties of the material [19,26,27]. Even for few cases, it is also observed that the magnetic moment per unit cell and the lattice parameters are also very sensitive to crystal structure [28].

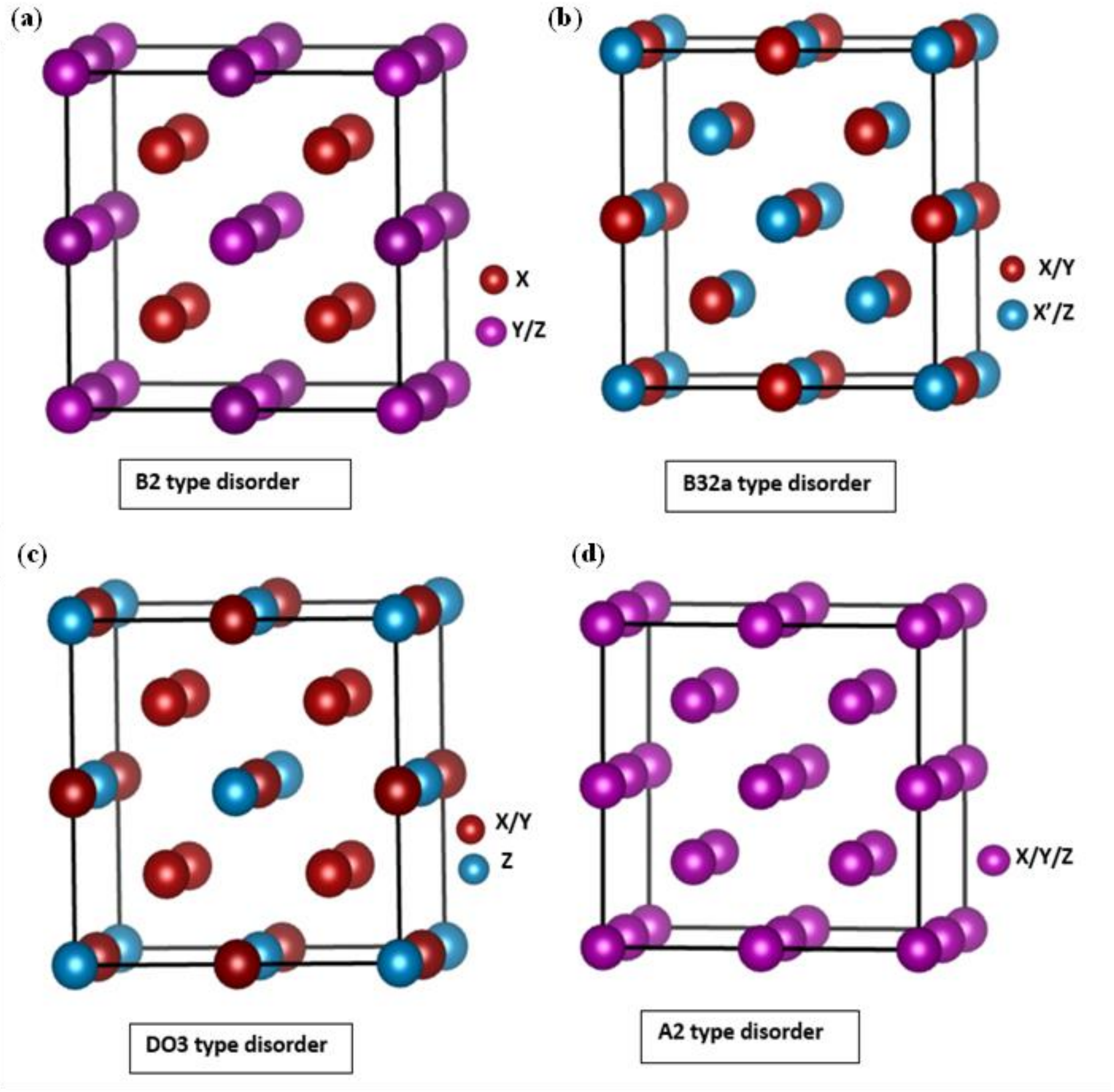

***Figure 1.5:*** *Crystal structures of preferential types of disorder: B2 (CsCl), B32a (NaTl),* $DO_3$ *(*$BiF_3$*) and A2 (W).*

Although, there is an infinite number of ways in which X, Y and Z atoms can be distributed among the four sublattices, but there are only 4 types of disorder observed in Heusler alloy. In the case of B2 type-disorder structure, the Y and Z atoms are randomly intermixed with each other, which results in a CsCl like structure. For B32a disorder, prototype to NaTl-structure, the X atoms which occupy one fcc sublattices is mixed with the Y atoms whereas the X′ atoms on the other sublattices are mixed with the Z atoms. However, this type of disorder is very difficult to realize experimentally. When the X and Y atomic positions are mixed, the lattice reduces to the D03 crystal structure. This structure can be attributed to $BiF_3$-type disorder. When all the atomic sites become intermixed with each other, the structure becomes the A2 type crystal structure. The X, Y and Z sites become equivalent leading to a body-centered cubic lattice, which is also known as a tungsten-type structure which is the most disordered structure of Heusler alloy material. Table 1.1 denotes the crystalline symmetry of the various ordered and disordered structures of Heusler alloys including structure type and space group.

***Table 1.1:*** *This table denotes the site occupancy, general formula, space group and space group number for all Heusler type compounds. ICSD is the nomenclature used for Inorganic Crystal Structure Database and SB is the Strukturberichte.*

| ***Site occupancy*** | ***General formula*** | ***Structure type (ICSD)*** | ***Structure type (SB)*** | ***Structure type (Pearson)*** | ***Space group*** |
|---|---|---|---|---|---|
| **X, X′, Y, Z** | **XX′ YZ** | **LiMgPdSn** | **Y** | **cF16** | **F-43m (no. 216)** |
| **X=X, Y, Z** | **$X_2YZ$** | **$Cu_2MnAl$** | **$L2_1$** | **cF16** | **Fm3m (no. 225)** |
| **X, X′=Y, Z** | **$XX'_2Z$** | **$CuHg_2Ti$** | **X** | **cF16** | **F-43m (no. 216)** |
| **X=X′=Y, Z** | **$X_3Z$** | **$BiF_3$** | **$DO_3$** | **cF16** | **Fm-3m (no. 225)** |
| **X=X′, Y=Z** | **$X_2Y_2$** | **CsCl** | **B2** | **cP2** | **Pm-3m (no. 221)** |
| **X=X′=Y=Z** | **$X_4$** | **W** | **A2** | **cI2** | **Im-3m (no. 229)** |
| **X=Y, X′=Z** | **$X_2X'_2$** | **NaTl** | **B32a** | **cF16** | **Fd-3m (no. 227)** |

The simulated powder XRD pattern using *VESTA* software of $Co_2FeSn$ under different crystal structures is shown in figure 1.6- a. Figure 1.6- b shows the zoom view of (111) and (200) reflections which are most important peaks for distinguishing different types of ordered and disordered in the crystal structures.

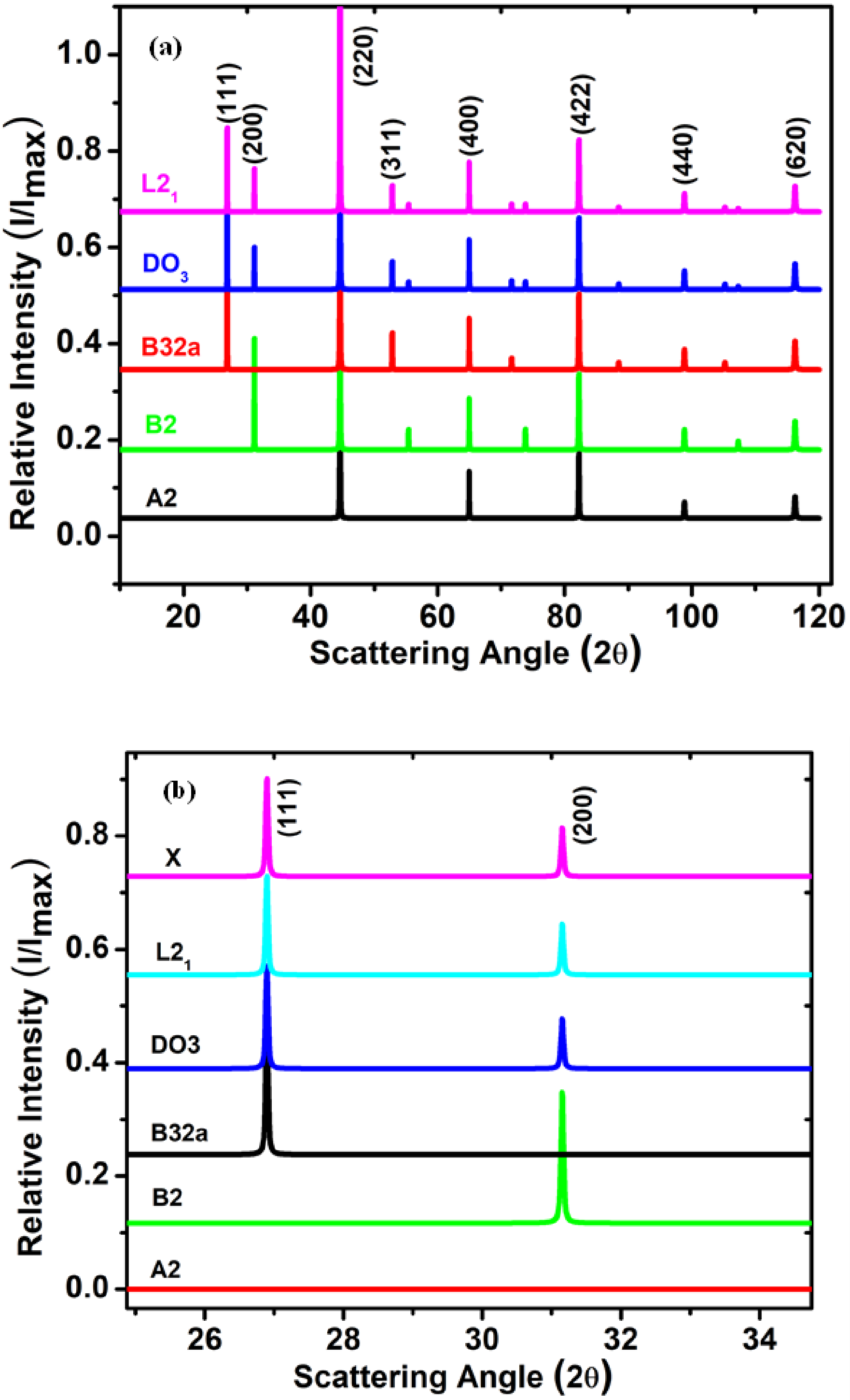

***Figure 1.6:*** *Calculated X-ray diffraction patterns of $Co_2FeSn$ in different order types: (a) Full range spectra; (b) Zoom-in of the (111) and (200) reflections. X-ray photon wavelength: 1.54 Å.*

A full Heusler ($L2_1$) and inverse Heusler (X) structure is identified by looking at the fcc-typical (111) and (200) reflections and their relation to the (220) reflection. However, the (111) and (200) reflections are very low in many alloys that's why much care has to be taken to visualize those reflections. Sometimes distinguishing between $L2_1$ and X becomes difficult due to intermixing of atoms and fcc-like symmetry. In B2 type structure, only (111) reflection vanishes whereas (200) reflection appears. In the case of B32a, the (200) reflection disappear and for A2 type both (111) and (200) reflections disappear. The difference between $L2_1$ and DO3 is very difficult using powder X-ray diffractions. A technique known as anomalous XRD can be utilized to distinguish between them. For some cases, a small disorder in an ordered compound cannot be detected by normal XRD so some other valuable techniques such as EXAFS [29], Mössbauer spectroscopy [30,31], nuclear magnetic resonance (NMR), neutron diffraction (ND) [32] are required to get the detail information of the Heusler alloys.

### 1.2.3 Slater-Pauling rule for magnetic moment

Most of the half and full Heusler alloy compounds follow a generalized rule for the prediction of magnetic and electric properties, which is widely known as the Slater-Pauling (S-P) rule [32,33]. They showed that the ferromagnetism in Heusler alloy originated from the spin on the electrons in the 3d-orbitals. Despite being 3d based compounds they show localized magnetism and integer magnetic moments in terms of μB /f.u.. Slater-Pauling behavior provides the method to estimate the magnetic moment ($M_t$) of alloy per unit cell as a function of the total number of valence electrons ($Z_t$) per atom. For the half-metallic full Heusler compounds such as $Co_2MnSn$, the Slater-Pauling rule is,

$$\mathbf{M_t = Z_t - 24} \qquad (1.1)$$

When the total number of valence electrons is more than 24, it is assumed that the gap in the density of states at $E_F$ is in the minority band. When the number of valence electrons is less than 24 (which leads to a negative magnetic moment), the half-metallicity is caused by a band gap in the majority band at $E_F$. In the case of half Heusler alloy such as NiMnSb, the generalized Slater-Pauling rule [34,35] is,

$$\mathbf{M_t = Z_t - 18} \qquad (1.2)$$

Figure 1.7 shows the total spin magnetic moments for the full Heusler alloys as a function of the total number of valence electrons ($Z_t$). Theoretically, it was found that half-metallic Heusler compounds follow the Slater-Pauling rule rigorously, and later on, it was proved experimentally [30,36,37] . In figure 1.7, the dashed line is the perfect Slater-Pauling line and it is clear that most of the alloys lie on the line except for a few exceptions. Rh-based Heusler alloy and a couple of Co-based Heusler alloys are out of the line. We also can observe that there is no element with a magnetic moment of more than 7μB, this is because in the minority spin band there are only 7 unoccupied states above the Fermi level. $Fe_2VAl$ is non-magnetic [38,39] because it has total 24 number of valence electrons so the magnetic moment for this alloy is zero from the S-P rule. $Co_2TiAl$ and $Co_2TiSn$ show deviation in magnetic moment from the S-P rule because of the Ti atom. In both cases, it is experimentally [40] proved that Co atom is only responsible for total magnetic moment of the system and Ti atom is nonmagnetic being very difficult to magnetize. Cobalt based Heusler alloys have almost all the properties which make them promising material for spintronics applications. Table 1.3 shows a few cobalt-based Heusler alloy and their experimental magnetic moments and theoretical moments from S-P rule.

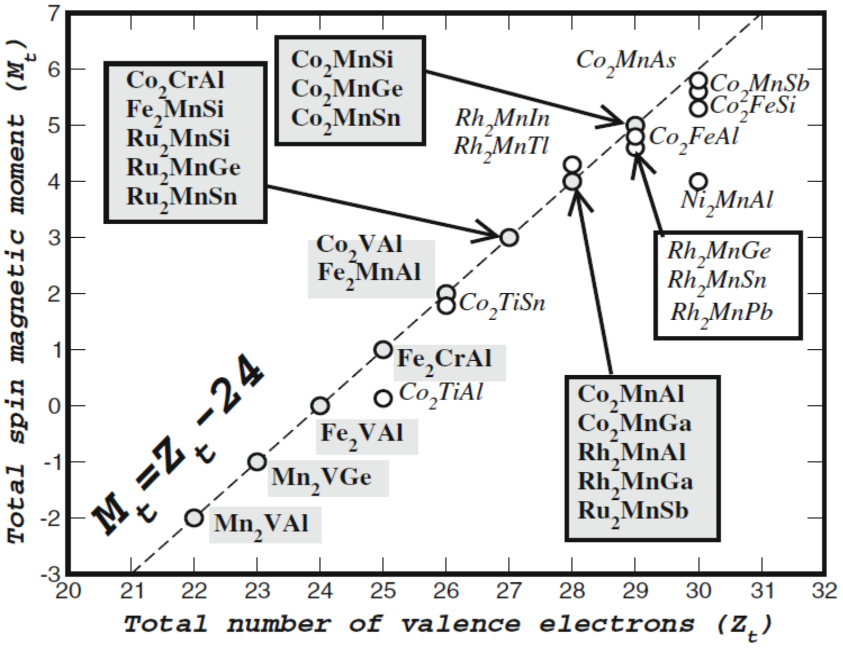

***Figure 1.7:*** *The Slater-Pauling curve for the half-metallic full Heusler alloy. Dashed line represents the Slater- Pauling behavior and the hollow circles represents the compounds deviating from the SP curve. (Adapted from [33]).*

***Table 1.2:*** *Summary of a few cobalt based Heusler alloy with theoretical and experimental magnetic moments.*

| ***Heusler compounds*** | $N_v$ | $m_{Co}$ | $m_Y$ | $m_Z$ | $m_{tot}$ | $m_{exp}$ | ***Ref.*** |
|---|---|---|---|---|---|---|---|
| $Co_2MnAl$ | 28 | 0.768 | 2.530 | -0.096 | 3.970 | 4.04 | [33,41,42] |
| $Co_2MnSi$ | 29 | 1.02 | 2.97 | -0.07 | 4.94 | 4.90 | [41,43,44] |
| $Co_2MnSn$ | 29 | 0.97 | 3.23 | -0.08 | 5.03 | 5.08 | [43,45] |
| $Co_2MnGe$ | 29 | 0.98 | 3.04 | -0.06 | 5.00 | 4.93 | [41,43] |
| $Co_2CrAl$ | 27 | 0.755 | 1.536 | -0.10 | 2.95 | 1.55 | [46,47] |
| $Co_2FeAl$ | 29 | 1.129 | 2.730 | -0.099 | 4.89 | 4.96 | [48,49] |
| $Co_2FeSi$ | 30 | 1.39 | 2.85 | -0.031 | 6.0 | 5.59 | [49,50] |
| $Co_2FeGa$ | 29 | 1.142 | 2.795 | -0.044 | 5.035 | 5.042 | [51,52] |

The contributions of magnetic moments from different elements have also been shown in table 1.2. It can be concluded from table 1.2 that, most of the Co-based alloy follows the generalized S-P rule. So, the spin density of states at the Fermi level can be control easily and material can be studied accordingly to get a specific magnetic moment. On the other hand, one can replace any element from alloy by substitution with other elements and magnetic moment can be calculated with the help of S-P rule.

### 1.2.4 Curie temperature

Curie temperature ($T_C$) is one of the most important parameter for any kind of applications of any type of ferromagnetic materials. Curie temperature is defined as that temperature above which a ferromagnetic material behaves like a paramagnetic one because the net magnetic moment is zero due to random thermal fluctuations of the moments. High Curie temperature is always expected for any device point of view. Whenever, the Curie temperature goes less than room temperature the importance and applications of the material goes down drastically.

***Table 1.3:*** *Crystalline structure, Curie temperature and lattice parameters of mostly used Co-based Heusler alloys.*

| ***Heusler compounds*** | ***Lattice parameter (Å)*** | ***Curie temperature (K)*** | ***Crystalline structure*** |
|---|---|---|---|
| $Co_2MnAl$ | 5.756<br>[53] | 693<br>[41,46] | B2 |
| $Co_2MnSi$ | 5.654<br>[53] | 985<br>[41,46] | $L2_1$ |
| $Co_2MnSn$ | 5.984<br>[54] | 829<br>[41,46] | |
| $Co_2MnGe$ | 5.743<br>[53] | 905<br>[41,46] | $L2_1$ |
| $Co_2CrAl$ | 5.727<br>[55] | 334<br>[47] | |
| $Co_2FeAl$ | 5.730<br>[54] | 1000<br>[55] | B2 |
| $Co_2FeSi$ | 5.640<br>[55] | 1100<br>[55] | $L2_1$ |
| $Co_2FeGe$ | 5.737<br>[51] | 1093<br>[51] | |

The lattice parameter and Curie temperature of a few Co-based alloy have been shown in the table 1.3. Most of them show Curie temperature more than room temperature except for $Co_2TiAl$ and $Co_2VSn$ (from figure 1.8- a). Co-based ($Co_2YZ$) Heusler alloy show very high Curie temperature comparable with the 3d metals elements because of very strong interaction between Co-Y and Co-Co on different sublattices. From figure 1.8, it is interesting to note that Curie temperature of Co-based alloy follow linear dependence with number of valence electron and magnetic moment per atom. There is a little variance for those alloys which have 27 number of valence electrons. The origin of linear dependency and the discrepancy has been investigated using ab-initio calculations in the local spin density approximations within the frozen magnon approach by Kubler et al. [56,57]. The authors have used the following equation to calculate the Curie temperature,

$$k_B T_C = \frac{2}{3}\sum_{\tau}\zeta_{\tau}^{2}\left[\frac{1}{N}\sum_{qn}\frac{1}{j_n(\boldsymbol{q})}\right]^{-1} \tag{1.3}$$

In the above equation, $\zeta_\tau$ is the local magnetic moment at site $\tau$ and exchange interactions within a sublattices and between sublattices are denoted by $j_n(q)$. So the term in the square bracket represents the average exchange interaction.

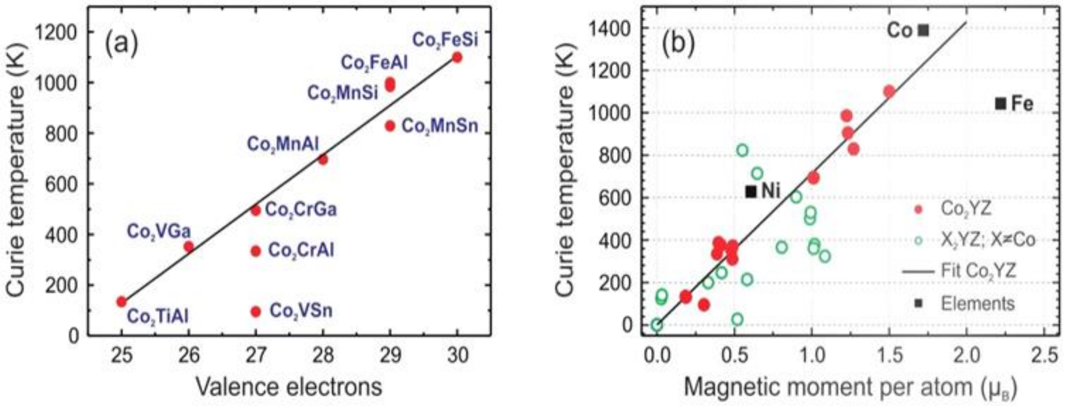

***Figure 1.8:*** *(a) Measured Curie temperature versus valence electron per unit cell for few Co-based Heusler alloy (b) Curie temperature as a function magnetic moment per atom ($T_C$ of Co, Fe, Sn are shown for comparison) (taken from [58,59]).*

### 1.2.5 Half metallic behavior in Heusler alloys

For any device point of view in spintronics, half metallicity is an important parameter. In this section, half metallicity in Heusler alloy is discussed in detailed. In 1983, Groot et.al [60] observed that Mn based Heusler alloy show unusual electronic property using spin-dependent band structure ab-initio calculations. They found that majority spin channel is metallic and minority spin channel is semiconducting or insulating. This property of material is known as half-metallicity. In this type of material Fermi level laid within the gap for the minority spin band and the conduction electrons are 100% spin polarized at the Fermi level. Few other systems such as magnetite $Fe_3O_4$, Cr oxides, the double perovskites ($Sr_2FeReO_6$) [61] has also shown half metallicity.

Before going in detail of half metallic nature, let’s have a look at the density of states of the paramagnet, ferromagnet and half-metallic ferromagnets. The degree of spin polarization is totally dependent on the density of states.

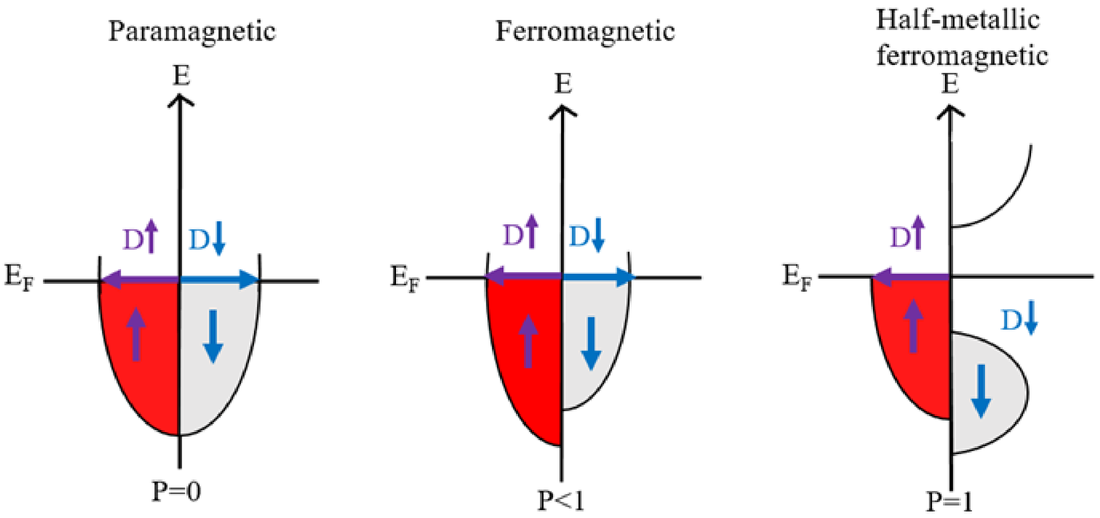

***Figure 1.9:*** *Schematic presentation of density of states of paramagnetic, ferromagnetic and half-metallic ferromagnet.*

The theoretical value of spin polarization for a ferromagnet is given by,

$$P = \frac{D\uparrow(E_F) - D\downarrow(E_F)}{D\uparrow(E_F) + D\downarrow(E_F)} \quad (1.4)$$

Where, P is spin polarization, $D\uparrow(E_F)$ is density of states for spin up electrons near Fermi level and $D\downarrow(E_F)$ is density of states for spin down electrons. From figure 1.9, it is clear that P=0 for paramagnetic as $D\uparrow(E_F) = D\downarrow(E_F)$. For a ferromagnet P < 1 as $D\uparrow(E_F) \neq D\downarrow(E_F)$. On the other hand, for a half metallic ferromagnet P=1 [62,63] because $D\downarrow(E_F)$ =0 as down spin electrons do not cross the Fermi level.

After the discovery of half metallicity in NiMnSb and PtMnSb, people have looked for half metallicity in other types of Heusler alloy and found some of them are indeed half metallic. S. Ishida and his coworkers [64–67] extensively studied the Co-based Heusler alloy and their half metallic property. They investigated $Co_2MnZ$ (Z= Al, Ga, Si, Ge, Sn) using density of states function theory and found that only Z= Si and Ge are half metallic and others are normal metals. They also found that the in case of Z= Al, Ga, Sn, the Fermi level is sitting near the energy gap of spin down band which means one can change the number of electrons per formula unit and get the half metallic behavior. The nonstoichiometric system with $Co_2MnZ_{1-x}Z'_x$ is expected to be half metallic when the number of valence electrons of p-block element per unit formula is 4. Another Co-based system namely $Co_2TiZ$ (Z= Al, Si, Ge, Ga, Sn, Sb) has been widely studied theoretically as well as experimentally for half metallic nature [68–72]. Half metallic nature is observed when Z= Sn, Al, Si and Ge and total moment per unit cell is about $2\mu_B$ and located mostly at the Co atoms. $Co_2TiGa$ is nearly half metallic, and $Co_2TiSb$ shows a large minority DOS at the Fermi energy like a normal metal. Although the half metallicity in $Co_2TiAl$ is little uncertain because Ti–Al disorder significantly degrades the half metallicity [57]. The main problem with $Co_2Ti$ based alloy is their low Curie temperature which makes them unimportant. For example, $Co_2TiSi$ has Curie temperature of 375 ºK but a substitution make their Curie temperature very high. Another interesting low Curie temperature (334 ºK) Heusler alloy $Co_2CrAl$ is expected to show half metallic behavior [73–75].

Figure 1.10 shows the spin projected DOS of $Co_2CrAl$ from which it is clear that for spin down electrons there is zero DOS near Fermi level. It is well known that that in $Co_2CrAl$, the half-metallicity is robust against Cr-Al substitutional disorder. So, with the substitution of Fe namely, Co (Fe, Cr) Al, the Curie temperature can be increased to 630 °K but as the same time Fe will destroy the half-metallicity of the system [25,77].

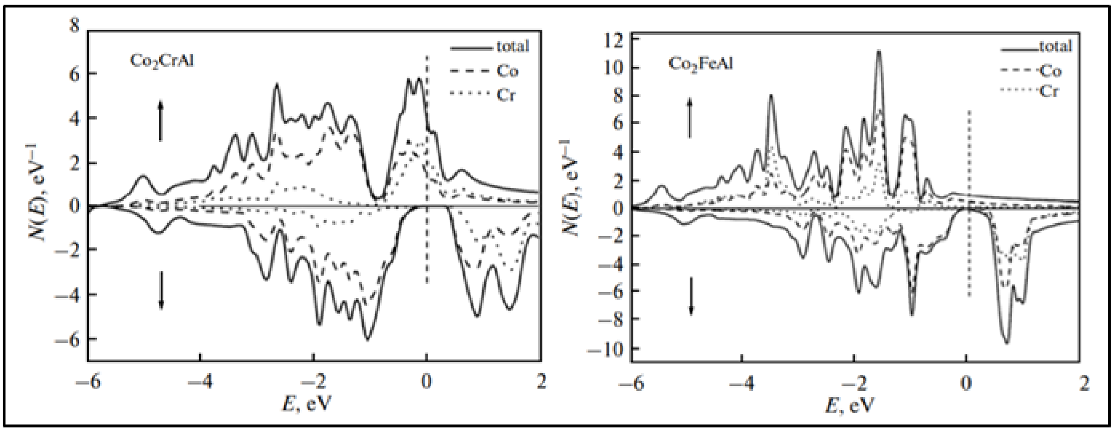

***Figure 1.10:*** *Calculated spin-projected density of states (DOS) for $Co_2CrAl$ and $Co_2FeAl$ [76].*

### 1.2.5.1 The origin of half metallicity

I. Galanakis et al. [33] have discussed the origin of half metallicity and formation of minority gap near the Fermi level using the full-potential screened Korringa-Kohn-Rostoker (KKR) method. In their study, they used $Co_2MnZ$ (Z= Al, Si, Ga, Ge) along with a few other Heusler system and explained their half metallic nature in a systematic way. According to their model, the four *sp*-orbitals sits below the Fermi level so they don’t contribute to the minority gap in channel of these materials. The strong d-orbitals hybridization of all X, Y, Z elements leads to the gap in the band structure of those materials. In the case of $Co_2MnZ$ the hybridization of Co-Co d-states and d-orbitals of Mn atom creates the gap in the minority gap.

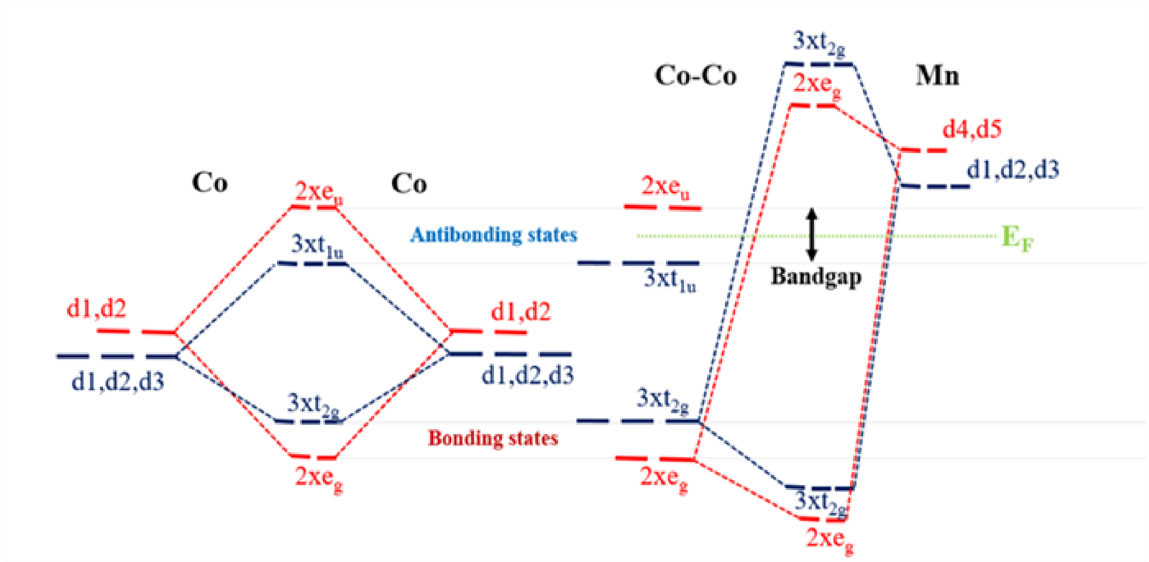

***Figure 1.11:*** *Schematic representation of hybridization of different elements in Heusler type materials. The number in front of the orbitals is the degeneracy of each orbital. (Taken from ref. [33]).*

Figure 1.11 shows the possible hybridization scheme of different d-electrons and presents them systematically. The d1, d2, d3, d4, d5 orbitals of Co atoms correspond to $d_{xy}$, $d_{yz}$, $d_{zx}$, $d_{3z^2-r^2}$ and $d_{3x^2-y^2}$ respectively. The d4 and d5 orbitals of the interacting Co atoms form low energy double- degenerated bonding $e_g$ and high energy antibonding $e_u$ orbitals. On the other hand, d1, d2, d3 form triple-degenerated less energy bonding $t_{2g}$ and high energy antibonding $t_{1u}$ orbitals. Now, the contribution of Mn 3d-orbitals comes into picture. The 3d-orbitals of Mn hybridize with Co-Co. It can be clearly seen from figure 1.11 that the d4, d5 of transition element Mn hybridize with doubly degenerate $e_g$ of Co-Co to give low energy bonding $e_g$ which is again doubly degenerate and doubly degenerate anti-bonding $e_g$ which lies above the Fermi level. Similarly $t_{2g}$ of Co-Co interact with d1, d2, d3 triply degenerate high energy anti-bonding $t_{2g}$ and less energy bonding $t_{2g}$. The band gap is created between higher $t_{2g}$ states or valence band and lower

$e_g$ states of conduction band. The anti-bonding states $e_u$ and $t_{1u}$ do not interact with the Mn d-orbitals. However, the Fermi level in situated between this two anti-bonding of Co orbitals with a gap in the minority spin band which leads to the halt-metallic behavior. The main-block element Z has sp- orbitals which have with less energy so it does not contribute in the gap. Although Galanakis [33] showed that the Z-element act as electron reservoir and it could easily shift the Fermi level. Finally a single elemental half-metallicity concept is not possible because of requirements of ordering in the 3d and 4s orbitals in the band structure.

## 1.3 Magneto Optical Kerr Effect (MOKE):

Magneto Optical (MO) effect is the interaction between magnet and light. It was Michael Faraday in early 1845 [78] who discovered that plane of polarization of linearly polarized light rotated when transmitting through a piece of lead borosilicate glass in presence of magnetic field. This effect is known as Faraday Effect according to his name. He also verified that the rotation of plane of polarization of the transmitted light is totally dependent on the strength of the magnet. Initially, Faraday Effect was explained classically by Lorentz in 1884 because quantum mechanics was not discovered at that time. He proposed that left and right circularly polarized light coupled differently to classical electron oscillators in the solid so there is change in the plane of polarization.

Later on, in 1932, H. R. Hulme et al. [79] proposed that the spin polarized electron motion in the presence of spin orbit (SO) coupling causes the Faraday Effect. The problem with H. R. Hulme's theory was that he only included the spin orbit induced splitting of the energy eigenvalues, but he neglected the effect of spin orbit coupling on the wave functions. Finally, P. N Argyres [80] in 1955 gives the complete formulation where he includes both spin orbit interaction and spin polarization. The application of Faraday Effect was proposed by him, he suggested that this can be used to characterize the magnetic material as the rotation of plane of polarization is proportional to applied magnetic field [81]**.** Unfortunately, study of Faraday effect on ferromagnetic cobalt, iron films proved that the linear dependence is no longer valid [82]**.** Figure 1.12 shows the Schematic representation of Faraday effect.

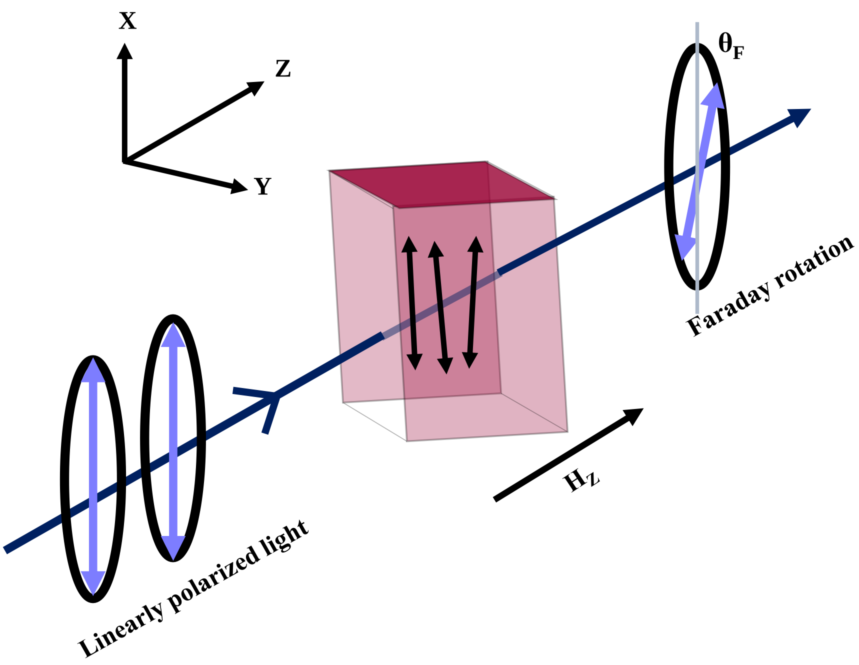

***Figure 1.12:*** *Schematic representation of Faraday Effect.*

Another type of MO phenomena is Zeeman effect [83,84] which says that there is a splitting in the spectral lines of Na atom in presence of a magnetic field. Another effect is Cotton-Mouton effect [85] where the occurrence of magnetic double refractions is observed in paramagnetic liquids. Among all the MO effects only Kerr effect and Faraday effect are linearly proportional to the magnetization of material or applied magnetic field.

MOKE, widely known as magneto optical Kerr effect [86] is another type of magneto optical effect. It was discovered by Scotch scientist John Kerr in 1875. He observed the rotation of polarization plane of linearly polarized light when the light is reflected from the surface of magnetic piece of iron. The electric and magnetic component of incident light interacts with magnetic surface and this way the plane of polarization rotate. The amount of rotation of plane of polarization is proportional to the magnetization of the sample. This makes the MOKE very efficient for surface magnetization study at very low scale. MOKE is also used to study the magnetic reversible process in magnetic thin films. This effect is used to obtain the hysteresis loops. This technique is also useful for the visualizing surface and subsurface magnetic domains. In 1962 Conger et al. [87] showed that it could be employed to readout suitably stored magnetic information. Since then, MO recording has become a leading technology in the data storage industry [88]. This technique is highly sensitive and it can influence the subatomic layer magnetism within the skin depth region, typically 10-30 nm for metals.

MOKE is comparatively simple technique compared to other technique for magnetic study but one has to understand the different terminology related to this. Light is a transverse electromagnetic wave by nature but one can manipulate this nature and convert it into plane polarized, circularly polarized or elliptically polarized by using different polarizer. The term polarization was first depicted by Étienne-Louis Malus in 1811 and since then this term has been used for not only in optics but also in other branch of physics. In optics, plane of polarization is refereed to that plane which contains the electric field **E** and direction of propagation **k**. So, based on the polarization of electric field there could be two type of polarization i.e. p-polarize and s-polarize. In p-polarized light the electric field is polarized in the plane of the incidence. When the electric field is polarized in the perpendicular to the plane of incidence is known as s-polarized light. As we know circularly polarized light can be consists of two perpendicular plane wave equal magnitude but 90 degree difference in phase. So, there could be two type of circularly polarized light namely right circularly and left circularly. Right circularly polarized (R-polarized) means the electric field is rotating in the anticlockwise direction with respect to the direction of propagation whereas Left circularly polarized (L-polarized) means the electric field is rotating in the clockwise direction with respect to the direction of propagation.

## 1.4 Magneto Thermal Effect:

Magneto-thermal (MT) effect is the heat generation by the application of AC magnetic field. This effect has been studied extensively especially for applications related to the field of magnetic hyperthermia therapy (MHT) to treat cancer and other diseases. The required heat to destroy the affected cell is generated by different magnetic nanoparticles, fully dispersed in solution, by exposing in a high frequency AC magnetic field [89–93]. Different kinds of alloys, such as FeCo, NiCo, spinel oxides $CoFe_2O_4$, $MnFe_2O_4$ have been studied extensively for magnetic hyperthermia treatments [94–97]. In this thesis, we have shown the Magneto-thermal effect in $Co_2FeSn$ and $Co_2FeAl$ Heusler alloy nanoparticles that may be useful for MHT application.

A deep understanding of physics, development of magnetic nanoparticles having precisely controlled shape, size and magnetic properties of nanoparticles and dynamics of nanoparticles in the solution are essential to develop MHT. On the other hand, it is also very important to understand the possible mechanism that produces heat in the MHT. The concentration of nanoparticles in the solution should be high so that it can generate enough heat to damage the cell. For MHT application, the nanoparticle should have high saturation magnetization ($M_S$) which will produce large amount of heat by the application of alternating magnetic field (AMF). The heat generation is also dependent on the magnetic moment per atom, coercivity ($H_C$), magnetic anisotropy ($H_K$), viscosity of fluid, remanent magnetization ($M_R$) and Curie temperature ($T_C$). Figure 1.13 shows a typical hysteresis loop for a ferromagnetic material and all the parameters related to the loop. The particle size should be 10-80 nm so that it should not have any other side effects.

There are possible three mechanisms in which the magnetic materials dissipate magnetic energy in the form of thermal energy. Those mechanisms are (a) Hysteresis loss: Most of the ferromagnetic materials are multi domain [98] and hysteresis loss is the dominant mechanism for heat generation in multi domain magnetic nanoparticles. To minimize the magnetic energy loss in a magnetic material, domains are being formed and when we apply an external magnetic field those domains interact with the field. Some domains expand and some shrink as long as they align themselves to the external field.

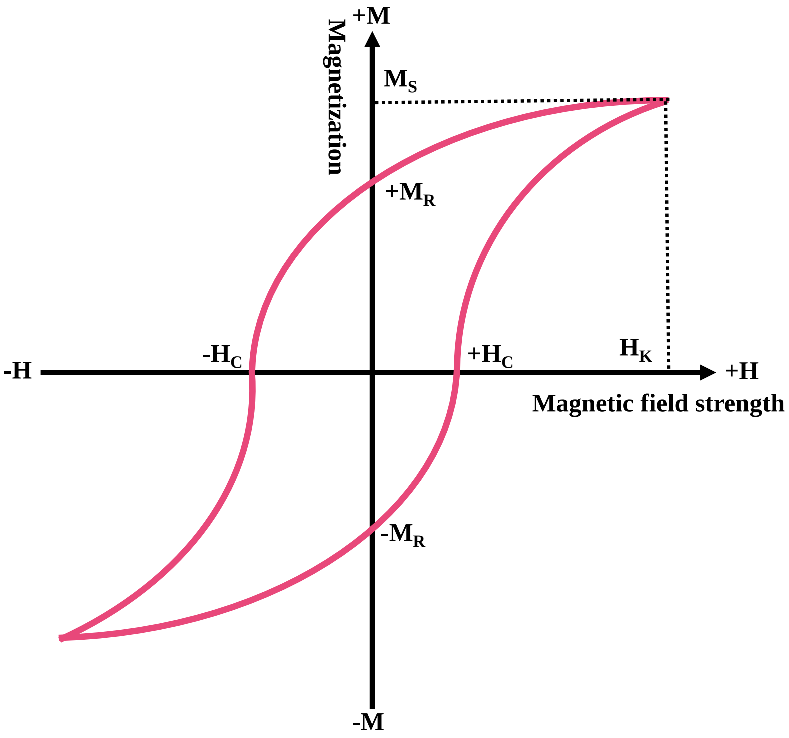

***Figure 1.13:*** *Representative figure of the B-H curve with important parameters of a ferromagnetic material.*

The domain wall motion in multi domain materials is accompanied by the loss which causes the heat generation. Enhanced magneto-crystalline anisotropy of the nanoparticles also contributes to increased hysteretic losses results in more heat generation. (b) Eddy current loss: When a magnetic materials are exposed to a magnetic field the material produces a circular current known as Eddy current. This current then generates a magnetic field which then tries to oppose the source of the current. In this way, the waste magnetic energy produces heat. Although, such losses have not been so effective to create efficient heat for the MHT application. (c) Relaxation loss: When the particle size is less than a critical value known as single domain limit the required energy to form the domain wall is higher than the magneto elastic energy loss so the nanoparticles prefer to form a single domain. In single domain nanoparticles the heat is generated via two process i.e. Neel relaxation and Brown relaxation. In Neel relaxation, the heat is generated by the magnetic anisotropy energy which hinders the reorientation of the super-spin. In Brown relaxation, heat is generated by the friction of shear stress in the viscous fluid.

## 1.5 Applications of Heusler alloys:

### 1.5.1 Spintronics

The understanding of magnetism in nanoscale region such as electrons is purely a relativistic quantum effect. Spintronics widely known as spin electronics deals not only with the charge of electrons but their spin degree of freedom as well. This field gained a huge thrust after the experimental discovery of giant magnetoresistance (GMR) in 1988 by Albert Fert [99] and Peter Grünberg [100] (independently), later they won the Nobel Prize in Physics in 2007. They have realized the GMR in Fe/Cr multilayers later on in 1996 magnetic tunnel junctions (MTJ) consists of tri-layer hetero-structures composed of two ferromagnetic (FM) layers separated by a very thin non-magnetic (NM) insulating barrier layer. After a few years of the discovery of GMR, it was the IBM Company that first introduced GMR based read heads commercially, which can very sensitively detect small magnetic fields.

On the other hand, tunnel magnetoresistance (TMR) was discovered by Julliere in 1975 [101] where he observed a 14% of resistance change at 4.2K in an amorphous insulating layer. The TMR ratio in the ferromagnetic/insulator/ferromagnetic layer can be estimated by the Jullière model [101] using the following equation,

$$TMR = \frac{R_{ap}-R_p}{R_p} = \frac{2P_1P_2}{1-P_1P_2}.100 \quad (in\ \%) \tag{1.5}$$

Where, $R_{ap}$ is the resistance when two magnetic layers are magnetized antiparallel to each other and $R_p$ is the resistance when the layers are magnetized in parallel. $P_1$ is the spin polarization of one electrode and $P_2$ is the spin polarization of other electrode. $P$ is defined by the following equation,

$$P = \frac{N_{\uparrow}-N_{\downarrow}}{N_{\uparrow}+N_{\downarrow}} \tag{1.6}$$

Where, $N_{\uparrow}$ is the majority density of states at Fermi energy and $N_{\uparrow}$ is minority density of states at Fermi energy. The GMR and TMR ratios are directly proportional to the spin polarization of the electrodes so the electrode should possess a high value of spin polarization. Spin polarization of conventional 3d-elements are less than 50% so there has been a huge demand to increase this value to get closer to 100%. In 1983 R. A. de Groot [60] revealed that some Heusler compounds are 'half metals' (theoretically 100% spin polarized) using band structure calculations. Since then there are so many full and half Heusler alloy have been reported as half metals. A TMR ratio of 550% at low temperature was reported by Y. Sakuraba et.al [14] in $Co_2MnSi$ Heusler alloy with amorphous aluminium oxide spacer. Another report on $Co_2MnSi/MgO/Co_2MnSi$ by T. Ishikawa et.al [102] shows a tunnel magnetoresistance ratios up to 180% at room temperature and 700% at 4.2 K temperature. $Co_2FeAl$ is considered to have the highest spin polarization among all the Heusler alloy and MTJ consisting of $Co_2FeAl/MgO/CoFe$ showed a magnetoresistance ratio of 330% at room temperature and 700% at 10 K temperature [103]. Along with the half metallicity, Heusler alloy also have high Curie temperature $T_C$ more than room temperature, large band gap at the Fermi level which makes Heusler alloy a perfect candidate for spintronics applications.

### 1.5.2 Magneto-optical application

The surface magnetization is generally studied by Kerr rotation or circular dichroism which is also known as magneto-optical effect. Half Heusler PtMnSb [104] shows a huge Kerr rotation of 2.5 degrees at 720 nm in room temperature which is the highest in all Heusler families. Later on PdMnSb, NiMnSb, and PtMnSn were also studied but they showed less response compared to the PtMnSb [105] because of the unnatural electronic structure of this alloy. In PtMnSb, one spin channel is metallic while is semiconducting is the reason for such a high magneto-optical response. In 2001 R. Carey [106] found the giant Kerr rotation of 5 degrees in PtMnSb at low temperature. $Co_2$-based Heusler alloy [54,107] also shows high and interesting magneto-optical properties. Although the magneto-optical effect can be enhanced with doping [108,109] or some external stimuli**.** Such a giant Kerr rotation is very important for next generation high density magneto-optical applications.

### 1.5.3 Thermoelectricity

Heusler compound also holds an important application in thermoelectricity. When the total number of valence electron is 18, the compound is expected to be semiconducting [110,111] and these compound show a high Seebeck coefficient and low electrical resistivity. Mostly the half Heusler alloy based on Ti- and Zr- are the candidates for the thermoelectric applications [112–117]. There are few full Heusler alloy with valence electron of 24 also showed an enhanced Seebeck coefficient [118–120]. The Heusler alloy with martensitic transition have interesting properties like large shape memory effect and large magneto-caloric effect as well. Figure 1.14 shows all the possible application of Heusler alloy.

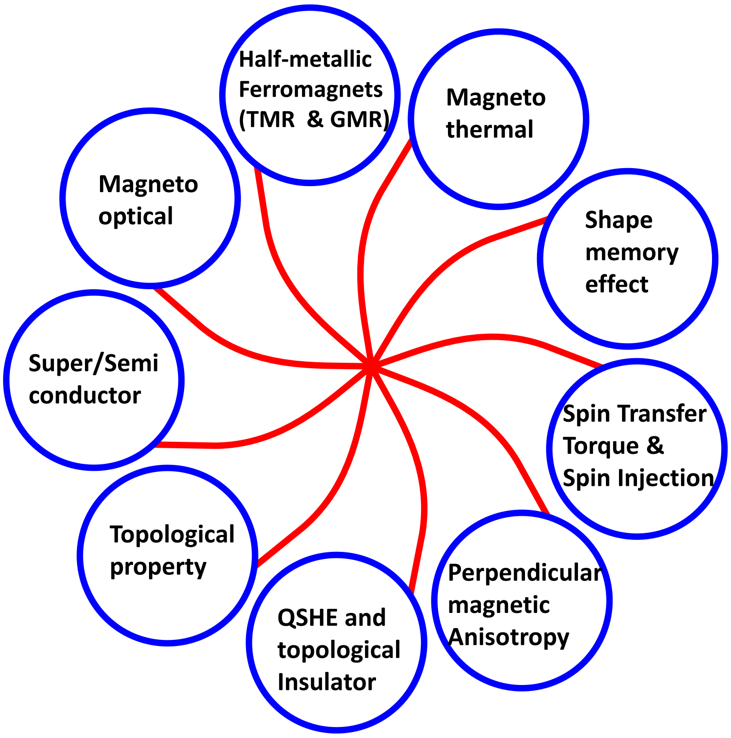

***Figure 1.14:*** *Possible application of Heusler alloy*

## 1.6 Literature review on $Co_2FeSn$ Heusler alloy:

$Co_2FeSn$ is expected to be a versatile spintronic material due to large spin polarization [122, 123] and possible topological property [124]. According to the Slater-Pauling rule $Co_2FeSn$ Heulser alloy ($Co_2FeSn$) should have large magnetic moment of $6\mu_B$. K. Özdoğan et al. [121] theoretically calculated the moment which is $5.52\mu_B$. N. I. Kourov group [122] showed that bulk $Co_2FeSn$ has Curie temperature of ≈ 968 K. In 2015, H. L. Huang et al. [123] theoretically studied anomalous Hall Effect and current spin polarization in the cubic $L2_1$ structure of $Co_2FeSn$) by using the highly accurate all-electron FLAPW method. According to them, the spin polarization of the longitudinal current (PL) in $Co_2FeSn$ is ≈ 100% and the static spin polarization (PD) is less with differing in sign from PL. The calculated anomalous Hall conductivities (AHCs) is 200 S/cm according to their study. Three years later in 2018, J. Noky et al. [124] proposed that Heusler compound $Co_2FeSn$ exhibit only very small anomalous Hall conductivities (AHC) but a strong anomalous Nernst conductivity (ANC). Moreover, $Co_2FeSn$ is expected to host a nodal line structure with strong Berry curvature around 100 meV above the Fermi level. Due to this distance from $E_F$, the topological property cannot be detected in the anomalous Hall conductivity. Thus it gives a strong anomalous Nernst conductivity near the Fermi level, which they explained via a detailed analysis of the underlying mechanisms of the two effects in a real system and a minimal effective model.

However, a major challenge in realizing $Co_2FeSn$ stems from the fact that it has positive formation energy that makes it thermodynamically difficult to prepare [125]. As a result thin film growth of $Co_2FeSn$ has been found to be untenable using ultra high vacuum based physical vapor deposition (PVD) methods [126]. On the other hand, the formation energy of binary phases like CoFe, FeSn and CoSn that leads to phase segregation. Hence it is important to look beyond conventional PVD growth methods and it is proposed that a non-equilibrium method like electrodeposition can lead to successful growth of $Co_2FeSn$. Previously C. Chisholm et al. [127] deposited amorphous Sn–Co–Fe ternary alloys using an electrodeposition method and studied their structural and magnetic properties. Later on, in 2013 J. Duan et al. successfully deposited $Co_2FeSn$ film [128] using constant current mode (chrono-potentiometry) and later on in 2015, N. Watanabe et al. [129] also deposited $Co_2FeSn$ films using constant voltage mode (chrono-amperometry). The problem with all those deposited films is that they were deposited at high voltage or current which leads to thick film with poor morphology.

Also these films had A2 type fully disordered crystal structure. There has been few reports on the growth of $Co_2FeSn$ nanowires by electrodeposition technique. In 2018, H. Lu et al. [130] first reported the successful deposition of nanowires which have soft ferromagnetism and their easy magnetization axis is perpendicular to the long axis of nanowires and the nanowires show magnetic reversal as well. This was followed by growth of $Co_2FeSn$ nanowires by L. Galdun el al. [131]. These nanowires were show to have high spin polarization values of better than 0.85%.

## 1.7 Overview of thesis work:

This thesis presents new methods and critical understanding for the development cobalt-iron based Heusler alloy nanostructures namely that of $Co_2FeSn$ and $Co_2FeAl$ for possible magneto-optical and magneto thermal applications. Following is an overview of the chapters presented in this thesis work:

**(1) Introduction:** In this chapter, the introduction and the background of Heusler alloy including all the fundamental aspects as well all the possibilities of applications are elaborated. Different properties such as crystal structure, types of disorder in HA, Slater-Pauling rule for magnetic moment, Curie temperature and origin of half metallicity, etc. are also discussed. In the end, this chapter concludes with a brief summary of previous studies and importance of $Co_2FeSn$ Heusler alloys and the difficulties to grow them using the conventional vapour deposition techniques.

**(2) Film deposition and characterization techniques:** Chapter 2 presents various experimental methods used in this thesis work. This include different techniques used for synthesis, deposition and characterization of the Heusler alloy systems presented in this thesis. The structural characterization techniques such as X-Ray Diffraction (XRD), Transmission Electron Microscopy (TEM), and Atomic Force Microscopy (AFM), Scanning electron microscope (SEM) are also described in this chapter. The basis and working principle of vibrating sample magnetometer (VSM) and superconducting quantum interference device (SQUID), Magneto-optical Kerr effect (MOKE) technique and MOKE microscopy method for studying magnetic properties is discussed in details.

**(3) Electrodeposited Heusler alloy films with enhanced magneto-optical property:** A major challenge in the realization of thin films of Heulser alloys is to grow systems that are thermodynamically unstable using the conventional physical vapor deposition method. Chapter 3 discusses a novel scheme developed in this thesis [132] to electrodeposit high quality $Co_2FeSn$ films. The chapter describes a modified three-step electrochemical growth method for thin film deposition of thermodynamically unstable Heusler alloys. Using this scheme we have successfully grown $Co_2FeSn$ thin films on polycrystalline copper substrate. The chapter also presents the magneto optical property study of these films [132]. These electrochemically grown films are found to show excellent magneto–optical property using the magneto-optical Kerr effect (MOKE) technique.

**(4) Growth of $Co_2FeSn$ thin film on single crystalline silicon substrate and their magneto-optical applications:** Chapter 4 of this thesis presents a scheme for improvement of crystalline quality and roughness of $Co_2FeSn$ films by developing a method for electrodeposition of $Co_2FeSn$ thin films on a single crystalline substrate [133]. These electrodeposited film show good morphology with a finite $L2_1$ ordering as confirmed by the high-resolution hard X-ray diffraction. The deposited films show a large degree of magneto-optical Kerr rotation (MOKE) as well as high saturation magnetization at room temperature. The Kerr measurements show rotation reaching up to a maximum value of $\approx 0.8°$ on a single crystalline substrate which is comparable with the films grown by conventional techniques [133]. Using Kerr microscopy studies we understand the formation and evolution of the magnetic domains in these electrodeposited films. Through these studies, we develop an understanding of surface magnetization reversal in electrodeposited films [133]. The static MOKE measurements also reveal that electrodeposited samples possess strong uniaxial magneto-crystalline anisotropy which is very important for device application point of view. Furthermore, angle dependent MOKE measurements reveal a two-fold symmetry in the electrodeposited $Co_2FeSn$ Films that is typical of highly ordered crystalline Heusler alloy phase.

**(5) Strain and crystallite size controlled ordering of Heusler nanoparticles having high heating rate for magneto-thermal application:** Yet another challenge in the development of Heusler alloy nanostructures is to grow structurally ordered nanoparticles. In this chapter the thesis presents development of highly B2 ordered $Co_2FeSn$ HA nanocrystals [134]. $Co_2FeSn$ nanoparticles were synthesized using the reduction and decomposition method embedded in silica matrix. We have shown that by controlling the product of strain and coherent crystallite size of the nanoparticles the crystalline and structural ordering in Heusler nanoparticles can be optimized. The structural optimization is found to lead to improved magnetic property. Furthermore to evaluate the heat generation efficiency of the Heusler nanoparticles, magnetic hyperthermia efficiency was performed. A large specific absorption rate (SAR) value of about 112 W/gm was obtained at moderate strength of the alternating magnetic field.

**(6) Growth of $L2_1$ ordered $Co_2FeAl$ Heusler nano-crystals for magneto-thermal applications:** This chapter discusses growth, magnetic property and hyperthermia studies of highly crystalline $Co_2FeAl$ nanocrystals. The $Co_2FeAl$ nanoparticles were grown in PEG matrix that crystalizes in $L2_1$ phase. To study the magneto-thermal property, the hyperthermia measurements were employed. The nanoparticles shows a good heat generation capability leading to rise in the temperature with high SAR value under application of alternating magnetic field.

**(7) Conclusion:** This chapter briefly presents the conclusion and future outlook of the research work carried out in this thesis.

## 1.8 References:

[1] F. Heusler, Verhandlungen Der Dtsch. Phys. Gesellschaft **5**, 219 (1903).

[2] F. Heusler, W. Starck, and E. Haupt, Verh. DPG **5**, 220 (1903).

[3] D. P. Oxley, R. S. Tebble, C. T. Slack, and K. C. Williams, Nature **194**, 465 (1962).

[4] F. Kuroda, T. Fukushima, and T. Oguchi, J. Appl. Phys. **127**, 193904 (2020).

[5] P. J. Webster and K. R. A. Ziebeck, Phys. Lett. A **98**, 51 (1983).

[6] J. Winterlik, G. H. Fecher, B. Balke, T. Graf, V. Alijani, V. Ksenofontov, C. A. Jenkins, O. Meshcheriakova, C. Felser, and G. Liu, Phys. Rev. B **83**, 174448 (2011).

[7] G. Bonfiglio, K. Rode, K. Siewerska, J. Besbas, G. Y. P. Atcheson, P. Stamenov, J. M. D. Coey, A. V Kimel, T. Rasing, and A. Kirilyuk, Phys. Rev. B **100**, 104438

(2019).

[8] B. Yan and C. Felser, Annu. Rev. Condens. Matter Phys. **8**, 337 (2017).

[9] S. Chadov, X. Qi, J. Kübler, G. H. Fecher, C. Felser, and S. C. Zhang, Nat. Mater. **9**, 541 (2010).

[10] J. Winterlik, G. H. Fecher, A. Thomas, and C. Felser, Phys. Rev. B **79**, 64508 (2009).

[11] F. F. Tafti, T. Fujii, A. Juneau-Fecteau, S. R. de Cotret, N. Doiron-Leyraud, A. Asamitsu, and L. Taillefer, Phys. Rev. B **87**, 184504 (2013).

[12] F. Hu, B. Shen, J. Sun, and Z. Cheng, Phys. Rev. B **64**, 12409 (2001).

[13] A. Planes, L. Mañosa, and M. Acet, J. Phys. Condens. Matter **21**, 233201 (2009).

[14] Y. Sakuraba, a M. Hattori, M. Oogane, Y. Ando, H. Kato, A. Sakuma, T. Miyazaki, and H. Kubota, Appl. Phys. Lett. **88**, 192508 (2006).

[15] X. Yan, G. Joshi, W. Liu, Y. Lan, H. Wang, S. Lee, J. W. Simonson, S. J. Poon, T. M. Tritt, and G. Chen, Nano Lett. **11**, 556 (2011).

[16] G. Joshi, X. Yan, H. Wang, W. Liu, G. Chen, and Z. Ren, Adv. Energy Mater. **1**, 643 (2011).

[17] O. Heusler, Ann. Phys. **411**, 155 (1934).

[18] A. J. Bradley and J. W. Rodgers, Proc. R. Soc. London. Ser. A, Contain. Pap. a Math. Phys. Character **144**, 340 (1934).

[19] T. Graf, C. Felser, and S. S. P. Parkin, Prog. Solid State Chem. **39**, 1 (2011).

[20] I. Galanakis, *Springer International Publishing, Switzerland* (2016).

[21] A. Hirohata, M. Kikuchi, N. Tezuka, K. Inomata, J. S. Claydon, Y. B. Xu, and G. Van der Laan, Curr. Opin. Solid State Mater. Sci. **10**, 93 (2006).

[22] V. Alijani, S. Ouardi, G. H. Fecher, J. Winterlik, S. S. Naghavi, X. Kozina, G. Stryganyuk, C. Felser, E. Ikenaga, and Y. Yamashita, Phys. Rev. B **84**, 224416 (2011).

[23] V. Alijani, J. Winterlik, G. H. Fecher, S. S. Naghavi, and C. Felser, Phys. Rev. B **83**, 184428 (2011).

[24] L. Bainsla and K. G. Suresh, Appl. Phys. Rev. **3**, 31101 (2016).

[25] Y. Miura, K. Nagao, and M. Shirai, Phys. Rev. B **69**, 144413 (2004).

[26] Z. Gercsi and K. Hono, J. Phys. Condens. Matter **19**, 326216 (2007).

[27] J. M. Shaw, E. K. Delczeg-Czirjak, E. R. J. Edwards, Y. Kvashnin, D. Thonig, M. A. W. Schoen, M. Pufall, M. L. Schneider, T. J. Silva, and O. Karis, Phys. Rev. B **97**, 94420 (2018).

[28] K. Inomata, N. Ikeda, N. Tezuka, R. Goto, S. Sugimoto, M. Wojcik, and E. Jedryka, Sci. Technol. Adv. Mater. **9**, 14101 (2008).

[29] B. Ravel, M. P. Raphael, V. G. Harris, and Q. Huang, Phys. Rev. B **65**, 184431 (2002).

[30] S. Wurmehl, G. H. Fecher, H. C. Kandpal, V. Ksenofontov, C. Felser, H.-J. Lin, and J. Morais, Phys. Rev. B **72**, 184434 (2005).

[31] C. Wang, F. Casper, Y. Guo, T. Gasi, V. Ksenofontov, B. Balke, G. H. Fecher, C. Felser, Y.-K. Hwu, and J.-J. Lee, J. Appl. Phys. **112**, 124314 (2012).

[32] B. Ravel, J. O. Cross, M. P. Raphael, V. G. Harris, R. Ramesh, and L. V Saraf, Appl. Phys. Lett. **81**, 2812 (2002).

[33] I. Galanakis, P. H. Dederichs, and N. Papanikolaou, Phys. Rev. B **66**, 174429 (2002).

[34] X. M. Zhang, X. F. Dai, G. F. Chen, H. Y. Liu, H. Z. Luo, Y. Li, W. H. Wang, G. H. Wu, and G. D. Liu, Comput. Mater. Sci. **59**, 1 (2012).

[35] T. Graf, J. Winterlik, L. Müchler, G. H. Fecher, C. Felser, and S. S. P. Parkin, *Magnetic Heusler Compounds* (2013).

[36] J. Kübler, A. R. William, and C. B. Sommers, Phys. Rev. B **28**, 1745 (1983).

[37] H. C. Kandpal, G. H. Fecher, C. Felser, and G. Schönhense, Phys. Rev. B **73**, 94422 (2006).

[38] Y. Nishino, H. Kato, M. Kato, and U. Mizutani, Phys. Rev. B **63**, 233303 (2001).

[39] A. Matsushita, T. Naka, Y. Takano, T. Takeuchi, T. Shishido, and Y. Yamada, Phys. Rev. B **65**, 75204 (2002).

[40] W. Pendl Jr, R. N. Saxena, A. W. Carbonari, J. Mestnik Filho, and J. Schaff, J. Phys. Condens. Matter **8**, 11317 (1996).

[41] P. J. Webster and K. R. A. Ziebeck, Landolt-Brönstein-Group III Condensed Matter (1988).

[42] S. Plogmann, T. Schlathölter, J. Braun, M. Neumann, Y. M. Yarmoshenko, M. V Yablonskikh, E. I. Shreder, E. Z. Kurmaev, A. Wrona, and A. Ślebarski, Phys. Rev. B **60**, 6428 (1999).

[43] H. Ido, J. Magn. Magn. Mater. **54**, 937 (1986).

[44] L. Ritchie, G. Xiao, Y. Ji, T. Y. Chen, C. L. Chien, M. Zhang, J. Chen, Z. Liu, G. Wu, and X. X. Zhang, Phys. Rev. B **68**, 104430 (2003).

[45] W. Zhang, N. Jiko, K. Mibu, and K. Yoshimura, J. Phys. Condens. Matter **17**, 6653 (2005).

[46] M. Kawakami, Hyperfine Interact. **51**, 993 (1989).

[47] A. W. Carbonari, R. N. Saxena, W. Pendl Jr, J. Mestnik Filho, R. N. Attili, M. Olzon-Dionysio, and S. D. De Souza, J. Magn. Magn. Mater. **163**, 313 (1996).

[48] N. I. Kourov, V. V. Marchenkov, Y. A. Perevozchikova, and H. W. Weber, Phys. Solid State **59**, 898 (2017).

[49] B. Balke, S. Wurmehl, G. H. Fecher, C. Felser, and J. Kübler, Sci. Technol. Adv. Mater. (2008).

[50] H. C. Kandpal, G. H. Fecher, C. Felser, and G. Schönhense, Phys. Rev. B - Condens. Matter Mater. Phys. **73**, 1 (2006).

[51] M. Zhang, E. Brück, F. R. de Boer, Z. Li, and G. Wu, J. Phys. D. Appl. Phys. **37**, 2049 (2004).

[52] R. Y. Umetsu, K. Kobayashi, A. Fujita, K. Oikawa, R. Kainuma, K. Ishida, N.

Endo, K. Fukamichi, and A. Sakuma, Phys. Rev. B **72**, 214412 (2005).

[53] P. J. Webster, J. Phys. Chem. Solids **32**, 1221 (1971).

[54] P. G. Van Engen, K. H. J. Buschow, and M. Erman, J. Magn. Magn. Mater. **30**, 374 (1983).

[55] K. H. J. v Buschow, P. G. Van Engen, and R. Jongebreur, J. Magn. Magn. Mater. **38**, 1 (1983).

[56] J. Kübler, J. Phys. Condens. Matter **18**, 9795 (2006).

[57] J. Kübler, G. H. Fecher, and C. Felser, Phys. Rev. B **76**, 24414 (2007).

[58] G. H. Fecher, H. C. Kandpal, S. Wurmehl, C. Felser, and G. Schönhense, J. Appl. Phys. **99**, 08J106 (2006).

[59] O. Gaier, Thesis, A study of exchange interaction, magnetic anisotropies, and ion beam induced effects in thin films of $Co_2$-based Heusler compounds (2009).

[60] R. A. De Groot, F. M. Mueller, P. G. Van Engen, and K. H. J. Buschow, Phys. Rev. Lett. **50**, 2024 (1983).

[61] H. Kato, T. Okuda, Y. Okimoto, Y. Tomioka, K. Oikawa, T. Kamiyama, and Y. Tokura, Phys. Rev. B **69**, 184412 (2004).

[62] P. Dowben, J. Phys. Condens. Matter **19**, 310301 (2007).

[63] C. T. Tanaka, J. Nowak, and J. S. Moodera, J. Appl. Phys. **86**, 6239 (1999).

[64] S. Ishida, T. Masaki, S. Fujii, and S. Asano, Phys. B Condens. Matter **245**, 1 (1998).

[65] S. Ishida, S. Fujii, S. Kashiwagi, and S. Asano, J. Phys. Soc. Japan **64**, 2152 (1995).

[66] S. Fujii, S. Sugimura, and S. Asano, J. Phys. Condens. Matter **2**, 8583 (1990).

[67] S. Ishida, S. Akazawa, Y. Kubo, and J. Ishida, J. Phys. F Met. Phys. **12**, 1111 (1982).

[68] P. Klaer, M. Kallmayer, C. G. F. Blum, T. Graf, J. Barth, B. Balke, G. H. Fecher,

C. Felser, and H. J. Elmers, Phys. Rev. B **80**, 144405 (2009).

[69] V. Sharma, A. K. Solanki, and A. Kashyap, J. Magn. Magn. Mater. **322**, 2922 (2010).

[70] S. C. Lee, T. D. Lee, P. Blaha, and K. Schwarz, J. Appl. Phys. **97**, 10C307 (2005).

[71] P. Mohn, P. Blaha, and K. Schwarz, J. Magn. Magn. Mater. **140**, 183 (1995).

[72] M. C. Hickey, A. Husmann, S. N. Holmes, and G. A. C. Jones, J. Phys. Condens. Matter **18**, 2897 (2006).

[73] N. I. Kourov, A. V Korolev, V. V Marchenkov, A. V Lukoyanov, and K. A. Belozerova, Phys. Solid State **55**, 977 (2013).

[74] K. Nagao, Y. Miura, and M. Shirai, Phys. Rev. B **73**, 104447 (2006).

[75] Y. V Kudryavtsev, V. N. Uvarov, V. A. Oksenenko, Y. P. Lee, J. B. Kim, Y. H. Hyun, K. W. Kim, J. Y. Rhee, and J. Dubowik, Phys. Rev. B **77**, 195104 (2008).

[76] E. I. Shreder, A. D. Svyazhin, and K. A. Belozerova, Phys. Met. Metallogr. **114**, 904 (2013).

[77] S. Wurmehl, G. H. Fecher, K. Kroth, F. Kronast, H. A. Dürr, Y. Takeda, Y. Saitoh, K. Kobayashi, H. J. Lin, G. Schönhense, and C. Felser, J. Phys. D. Appl. Phys. **39**, 803 (2006).

[78] M. Faraday, Philos. Trans. R. Soc. London 1 (1846).

[79] H. R. Hulme, Proc. R. Soc. London. Ser. A, Contain. Pap. a Math. Phys. Character **135**, 237 (1932).

[80] P. N. Argyres, Phys. Rev. **97**, 334 (1955).

[81] W. Voigt, *Magneto-Und Elektrooptik* (BG Teubner, 1908).

[82] H. Du Bois, London, Edinburgh, Dublin Philos. Mag. J. Sci. **24**, 445 (1887).

[83] P. Zeeman, London, Edinburgh, Dublin Philos. Mag. J. Sci. **43**, 226 (1897).

[84] P. Zeeman, Leiden Commun **29**, (1896).

[85] A. Cotton and H. Mouton, CR Hebd Seances Acad. Sci. Paris **145**, 229 (1907).

[86] J. Kerr, London, Edinburgh, Dublin Philos. Mag. J. Sci. **3**, 321 (1877).

[87] R. L. Conger and J. L. Tomlinson, J. Appl. Phys. **33**, 1059 (1962).

[88] R. Carey, D. M. Newman, and B. W. J. Thomas, J. Phys. D. Appl. Phys. **28**, 2207 (1995).

[89] A. H. Habib, C. L. Ondeck, P. Chaudhary, M. R. Bockstaller, and M. E. McHenry, J. Appl. Phys. **103**, 07A307 (2008).

[90] Ö. Çelik, M. M. Can, and T. Firat, J. Nanoparticle Res. **16**, 1 (2014).

[91] R. Hergt, S. Dutz, R. Müller, and M. Zeisberger, J. Phys. Condens. Matter **18**, S2919 (2006).

[92] I. M. Obaidat, B. Issa, and Y. Haik, Nanomaterials **5**, 63 (2015).

[93] K. Mahmoudi, A. Bouras, D. Bozec, R. Ivkov, and C. Hadjipanayis, Int. J. Hyperth. **34**, 1316 (2018).

[94] Y. Jing, H. Sohn, T. Kline, R. H. Victora, and J.-P. Wang, J. Appl. Phys. **105**, 07B305 (2009).

[95] A. A. Kuznetsov, V. G. Leontiev, V. A. Brukvin, G. N. Vorozhtsov, B. Y. Kogan, O. A. Shlyakhtin, A. M. Yunin, O. I. Tsybin, and O. A. Kuznetsov, J. Magn. Magn. Mater. **311**, 197 (2007).

[96] A. B. Salunkhe, V. M. Khot, J. M. Ruso, and S. I. Patil, J. Magn. Magn. Mater. **419**, 533 (2016).

[97] V. M. Khot, A. B. Salunkhe, N. D. Thorat, R. S. Ningthoujam, and S. H. Pawar, Dalt. Trans. **42**, 1249 (2013).

[98] B. D. Cullity and C. D. Graham, *Introduction to Magnetic Materials* (John Wiley & Sons, 2011).

[99] M. N. Baibich, J. M. Broto, A. Fert, F. N. Van Dau, F. Petroff, P. Etienne, G. Creuzet, A. Friederich, and J. Chazelas, Phys. Rev. Lett. **61**, 2472 (1988).

[100] P. Grünberg, R. Schreiber, Y. Pang, M. B. Brodsky, and H. Sowers, Phys. Rev. Lett. **57**, 2442 (1986).

[101] M. Julliere, Phys. Lett. A **54**, 225 (1975).

[102] T. Ishikawa, N. Itabashi, T. Taira, K. Matsuda, T. Uemura, and M. Yamamoto, J. Appl. Phys. **105**, 07B110 (2009).

[103] W. Wang, H. Sukegawa, R. Shan, S. Mitani, and K. Inomata, Appl. Phys. Lett. **95**, 182502 (2009).

[104] P. G. Van Engen, K. H. J. Buschow, R. Jongebreur, and M. Erman, Appl. Phys. Lett. **42**, 202 (1983).

[105] R. A. De Groot, F. M. Mueller, P. G. Van Engen, and K. H. J. Buschow, J. Appl. Phys. **55**, 2151 (1984).

[106] R. Carey, D. M. Newman, and M. L. Wears, Phys. Rev. B **62**, 1520 (2000).

[107] K. H. J. Buschow and P. G. Van Engen, J. Magn. Magn. Mater. **25**, 90 (1981).

[108] J. Van Ek and J. M. Maclaren, Phys. Rev. B **56**, R2924 (1997).

[109] H. Feil and C. Haas, Phys. Rev. Lett. **58**, 65 (1987).

[110] H. C. Kandpal, C. Felser, and R. Seshadri, J. Phys. D. Appl. Phys. **39**, 776 (2006).

[111] F. G. Aliev, Phys. B Condens. Matter **171**, 199 (1991).

[112] Y. Kimura, H. Ueno, and Y. Mishima, J. Electron. Mater. **38**, 934 (2009).

[113] M. Zhou, L. Chen, C. Feng, D. Wang, and J.-F. Li, J. Appl. Phys. **101**, 113714 (2007).

[114] M. Schwall and B. Balke, Appl. Phys. Lett. **98**, 42106 (2011).

[115] W. Xie, Q. Jin, and X. Tang, J. Appl. Phys. **103**, 43711 (2008).

[116] T. Wu, W. Jiang, X. Li, Y. Zhou, and L. Chen, J. Appl. Phys. **102**, 103705 (2007).

[117] C. Uher, J. Yang, S. Hu, D. T. Morelli, and G. P. Meisner, Phys. Rev. B **59**, 8615 (1999).

[118] J. Barth, G. H. Fecher, B. Balke, S. Ouardi, T. Graf, C. Felser, A. Shkabko, A. Weidenkaff, P. Klaer, and H. J. Elmers, Phys. Rev. B **81**, 64404 (2010).

[119] T. Graf, J. Barth, B. Balke, S. Populoh, A. Weidenkaff, and C. Felser, Scr. Mater. **63**, 925 (2010).

[120] B. Balke, S. Ouardi, T. Graf, J. Barth, C. G. F. Blum, G. H. Fecher, A. Shkabko, A. Weidenkaff, and C. Felser, Solid State Commun. **150**, 529 (2010).

[121] K. Özdoğan, B. Aktaş, I. Galanakis, and E. Şaşıoğlu, J. Appl. Phys. **101**, 73910 (2007).

[122] N. I. Kourov, V. V Marchenkov, Y. A. Perevozchikova, and H. W. Weber, Phys. Solid State **59**, 898 (2017).

[123] H.-L. Huang, J.-C. Tung, and G.-Y. Guo, Phys. Rev. B **91**, 134409 (2015).

[124] J. Noky, J. Gooth, C. Felser, and Y. Sun, Phys. Rev. B **98**, 241106 (2018).

[125] M. Meinert and M. P. Geisler, J. Magn. Magn. Mater. **341**, 72 (2013).

[126] M. A. Tanaka, Y. Ishikawa, Y. Wada, S. Hori, A. Murata, S. Horii, Y. Yamanishi, K. Mibu, K. Kondou, T. Ono, and S. Kasai, J. Appl. Phys. **111**, 53902 (2012).

[127] C. Chisholm, E. Kuzmann, M. El-Sharif, O. Doyle, S. Stichleutner, K. Solymos, Z. Homonnay, and A. Vértes, Appl. Surf. Sci. **253**, 4348 (2007).

[128] J. Duan and X. Kou, J. Electrochem. Soc. **160**, D471 (2013).

[129] N. Watanabe, K. Sano, N. Tasugi, T. Yamaguchi, A. Yamamoto, M. Ueno, R. Sumiyoshi, T. Arakawa, and I. Koiwa, APL Mater. **3**, 41804 (2015).

[130] H. Lu, Y. Liu, and X. Kou, J. Electrochem. Soc. **165**, D813 (2018).

[131] L. Galdun, P. Szabo, V. Vega, E. D. Barriga-Castro, R. Mendoza-Reséndez, C. Luna, J. Kovac, O. Milkovic, R. Varga, and V. M. Prida, ACS Appl. Nano Mater. **3**, 7438 (2020).

[132] M. R. Karim, D. Panda, A. Adhikari, P. Sharangi, P. Mandal, S. Ghosh, S. Bedanta, A. Barman, and I. Sarkar, Mater. Today Commun. **25**, 101678 (2020).

[133] M. R. Karim, A. Adhikari, S. N. Panda, P. Sharangi, S. Kayal, G. Manna, P. S. A. Kumar, S. Bedanta, A. Barman, and I. Sarkar, J. Phys. Chem. C **125**, 10483 (2021).

[134] M. R. Karim, S. N. Panda, A. Barman, and I. Sarkar, Nanotechnology (2022) (accepted) https://doi.org/10.1088/1361-6528/ac56f7.

# Chapter 2

# *Experimental techniques*

In this chapter, different techniques used for synthesis, deposition and characterization of the Heusler alloy systems are discussed. Section 2.1 describes different synthesis/deposition techniques for the thin film along with those techniques used for deposition of $Co_2FeSn$ thin films. Section 2.2 devoted to describe the structural characterization techniques such as X-Ray Diffraction (XRD), Transmission Electron Microscopy (TEM), and Atomic Force Microscopy (AFM), Scanning electron microscope (SEM). In section 2.3, discusses the basis of vibrating sample magnetometer (VSM) and superconducting quantum interference device (SQUID). In last section, Magneto-optical Kerr effect (MOKE) technique and MOKE microscopy method will be discussed.

## 2.1 Different synthesis techniques:

### 2.1.1 Arc melting technique

One of the most earliest and important synthesis processes of Heusler alloy is arc melting process [1–4]. Even, F. Heusler used this process to synthesize the $Cu_2MnAl$ bulk alloy in early nineties. Later on, hundreds of alloys have been synthesized using this technique. In a typical arc melting system, polycrystalline sample can be prepared. An arc melting system consists of three main parts- the vacuum chamber, cooling system and the power source. Inside the chamber, a water-cooled cylindrical copper hearth is placed which acts as the anode and also functions as a crucible for melting the samples. The water cooled tungsten sharp tip acts as a cathode. To avoid any oxygen contamination, chamber must be evacuated to a base pressure using the rotary and turbo-molecular pump then argon gas backfilled to achieve the atmospheric pressure. All the metals should be placed inside the copper hearth and tungsten tip should bring close towards the metals. When the distance between them is very less, there will be arc discharge and argon plasma will be formed. As the temperature of the plasma is very high it melts every metal placed inside the hearth. To make sure, the uniform distribution of all metals, it is necessary to re-melt the sample again and again. To achieve the right stoichiometric ratio in the sample, one must consider the mass loss during the meting process because different elemets has mass loss during evaporation.

### 2.1.2 Magnetron Sputtering

Magnetron Sputtering is another famous technique to deposit the thin films of Heusler alloys [5–7]. In this technique, atoms are ejected from the surface of target by bombarding the energetic ions via energy transfer process. This technique can control deposition capability of wide range of material irrespective of its conductivity, deposition over large area, etc.

The Figure 2.1 shows the schematic diagram of a typical sputtering deposition system. Firstly, the chamber is evacuated using pumps to a high vacuum range (base pressure). Then argon gas is filled inside the chamber to get the working pressure. At working pressure, gaseous plasma will be formed and it will sputter the atoms from target material. There are mainly two kinds of sputtering available- DC sputtering and RF sputtering unit. In DC sputtering unit, two electrodes are placed inside the chamber which helps to form the argon plasma. It is useful to deposit any kind of conducting material.

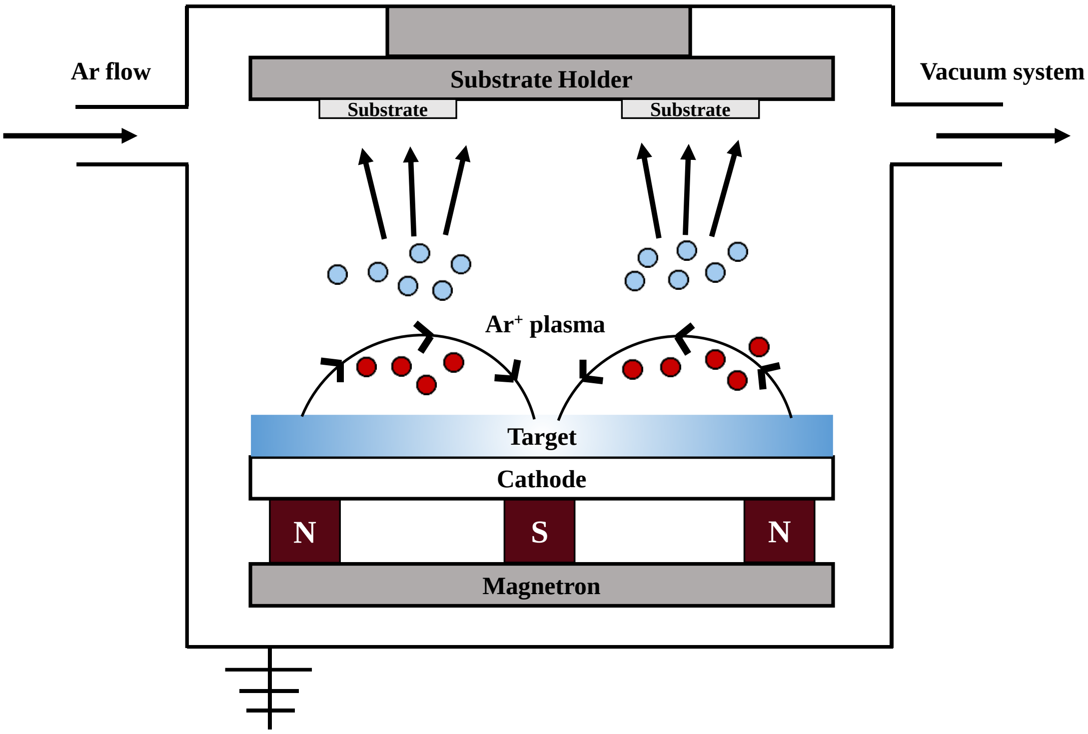

***Figure 2.1:*** *Schematic for sputtering deposition technique in a vacuum chamber. The Ar$^+$ ions (red circles) hits the target after a voltage is applied to it. The target atoms (blue circles) are ejected upon momentum transfer and deposit on the substrate.*

In RF sputtering, an radio frequency is used to form the plasma inside the chamber. RF sputtering is used to deposit non-conducting material mostly different metal oxides.

### 2.1.3 Electrodeposition technique

The electrodeposition technique is widely known as the electroplating. By definition, it is the technique which uses an electrical current to reduce the positive ions of a desired elements from an electrolyte solution and deposit those elements as a smooth thin film onto a conductive substrate surface. This technique has been extensively used in industry coating technology, for decoration and protection, to achieve the desired electrical and corrosion resistance of any surface, to improve the electrical conductivity.

There is two kinds of electrodeposition setup available: one is two electrode system and other one is three electrode system. Figure 2.2 shows the diagram of a three electrode electrodeposition system. In a typical electrochemical workstation, three electrodes are presents namely: working electrode/cathode (red in color), counter electrode/anode (black), reference electrode (blue). The current that passes through the electrolyte is measured across the working electrode and counter electrode. The reference electrode is to control the voltage. For the deposition of materials, cathodic deposition is used because most of the metals are positive ions. The other important component of electrodeposition is electrolyte solution which provides the ions to be deposited on the substrate. Electrolyte can be aqueous or non-aqueous which should contain all the metal salts. Metals salts are mostly positive ions and those ions accelerated towards the cathode which is the substrate. After reaching the cathode, the ions sees a huge electron cloud where ions receive electron and become neutral atoms.

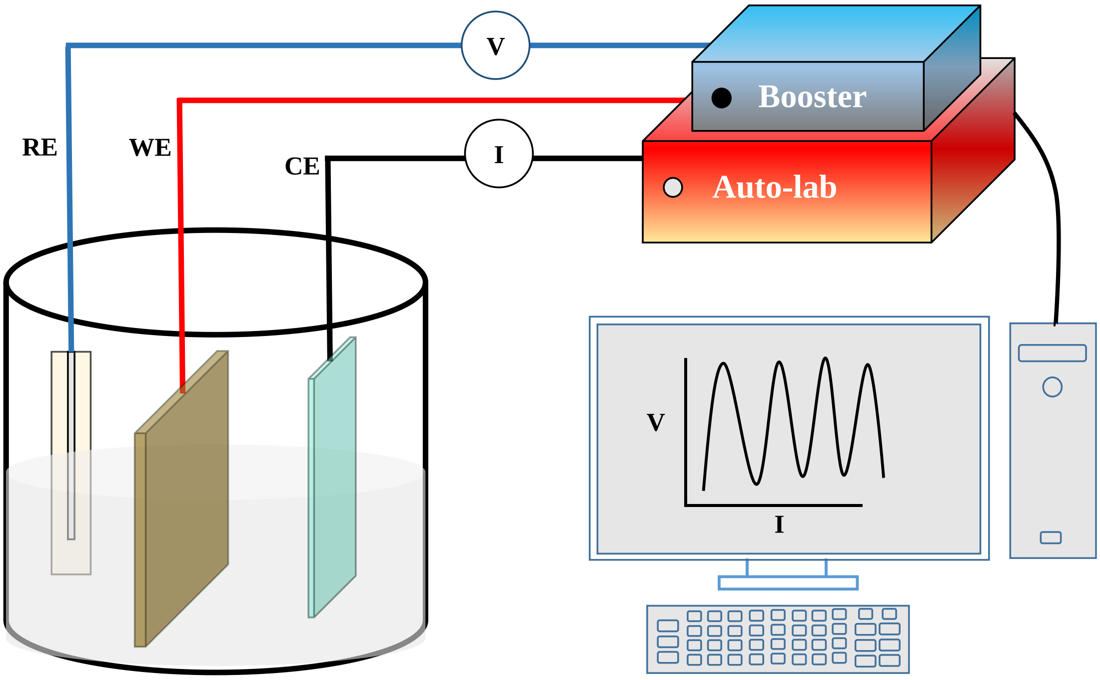

***Figure 2.2:*** *Illustration of the electrodeposition system with potentiostat, booster and conventional three electrode cell.*

pH of the electrolyte is very important factor which controls the deposition rate. Sometimes, different additives are used in the electrolyte to form the complex, to enhance or lower the deposition rate. The third component is power supply to drive the current through the electrolyte. There is three process to deposit the metals ions: (a) at any constant voltage where current will be changed with respect to time is known as potentiostatic mode deposition, (b) at constant current supply where voltage will be changed with respect to time is known as galvanostatic deposition. (c) using a current or voltage waveform known as pulse deposition. The process which is responsible for deposition can be outlined as, at cathode $M^{z+}(aq) + ze^{-} \rightarrow M(s)$ and at anode $M(s) \rightarrow M^{z+}(aq) + ze^{-}$. The Faraday law governs the amount of metals deposited which says that, the amount of chemical change produced by an electrical current is proportional to the quantity of electricity that passes through the electrolyte and the amounts of different substances liberated by a given quantity of electricity are inversely proportional to their chemical equivalent weights. We have used Autolab based PGSTAT302N from Metrohm AG electrochemical workstation for the thin film deposition. This instrument was equipped with the booster for high current deposition.

Other available methods to prepare the single crystal Heusler alloy are Bridgman method, the floating-zone method and the Czochralski technique. Molecular beam epitaxy, plasma quest high target utilization sputtering are also known method to deposit the thin film of Heusler alloy.

## 2.2 Different characterization techniques:

### 2.2.1 X-ray diffraction (XRD)

The X-ray diffraction (XRD) is the most important and non-destructive tool to identify the crystal structure of any kind of oriented materials. Using XRD one can find preferred crystal orientations, lattice spacing, phases, average grain size, crystallinity, crystal defects and strain etc. A schematic diagram of XRD shown in figure 2.3 where two identical beams incident on a crystalline plane and scatter off of two planes of atoms within the crystal.

The X-rays were discovered by Wilhem Röntgen [8] in 1895 and this are electromagnetic radiations wavelength ranging from 0.01-10 nanometers. As the inter planer distance between atoms in any crystal lattice is also in the same order of nanometer so according to diffraction rule the incident x-rays and atomic planes can interact with other. It was Max von Laue who first gave the explanation about this x-rays scattering process from an atomic planes. When the x-ray scattered off from the sample most of the wave cancel each other due to destructive interference. From the figure 2.3, it can be seen that the path difference between to rays is $2d\sin\theta$, where θ is the angle of incidence and d is the inter planer spacing in the crystal. Only constructive interference between rays will give the intensity peak and the condition was given by Bragg's law [9] which states that the path difference needs to be an integer number of wavelengths.

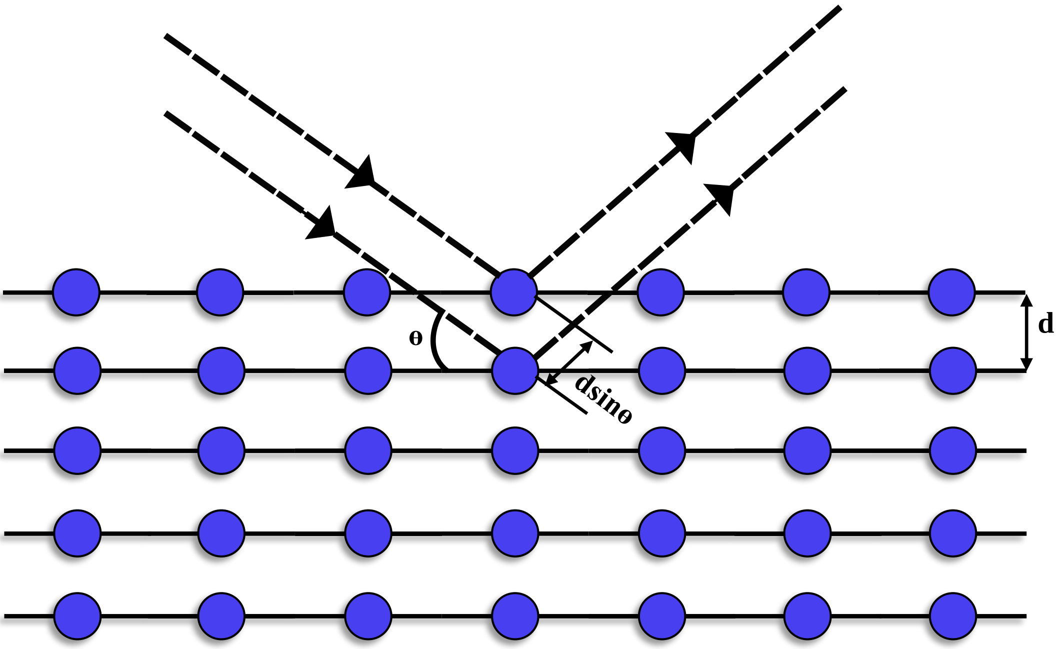

***Figure 2.3:*** *Schematic of XRD showing Bragg's diffraction from atomic planes*

$$2d\sin\theta = n\lambda \tag{2.1}$$

the wavelength of the radiation source is $\lambda$ and $\theta$ is called Bragg's angle. A typical X-ray diffractometer consists of three main components i.e. an X-ray tube, a sample holder, and an X-ray detector. For most of the case x-rays are generated in a cathode ray tube where, electron are produced from a filaments and then the electron are accelerated towards the target material by applying a positive voltage. When the electron are bombarded with the target materials, the inner cell electron of target materials excited giving rise a characteristic wavelength of the target materials. For target materials mostly Fe, Cu, Mo, Cr are used. The characteristic x-rays contain different component so filters are used make the beam monochromatic. The monochromatic x-ray then incident onto the sample and the reflected x-rays are collected at the detector. As the source and detector are rotated a peak in intensity occurs when the incident x-rays satisfy the Bragg's equation. The detector then processed the data and give a sharp intense peak for any highly crystalline sample. The design of the instrument is such that the source is rotated at an angle $\theta$ and detector is mounted on other arm, rotated at an angle $2\theta$. This kind of arrangement is known as goniometer type arrangement.

In this thesis work, Bruker make 8A ADVANCED ECO model powder diffractometer was used for phase analysis of deposited thin films and powder samples. Copper is used as a target material in this instrument, with Cu $K_\alpha$ radiation = 1.5418Å. The x-ray tube in this machine is working at 40kV voltage and 25mA current. For the thin film study, we have used grazing angle incidence XRD (GI-XRD) because the normal θ-2θ mode XRD may not be useful for thin films study and the signal strengths are very week. On the other hand, due to low angle incidence the skin depth is very low and signal strengths are strong in the case of GIXRD.

### 2.2.2 Transmission electron microscopy (TEM)

Transmission electron microscopy (TEM) is a very powerful tool to investigate the internal structural and chemical properties, morphology, and composition of any sample down to the atomic level. In 1926, H. Busch had discovered that the magnetic lenses are able to focus an electron beam in a certain direction. Keeping this in mind, in 1931, E. Ruska and M. Knoll [10] built the first transmission electron microscope (TEM) that consisted of two electromagnetic lenses. For this discovery, Ruska was awarded with Nobel Prize in 1986. Modern TEM have sufficient resolution to image individual atomic planes in crystalline solids.

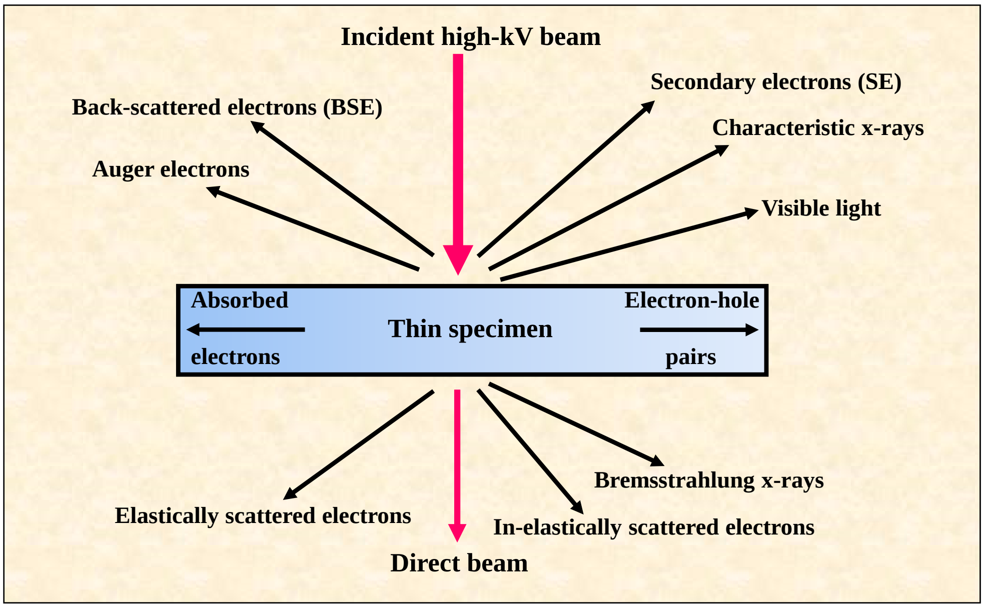

***Figure 2.4:*** *Interaction of an electrons with a specimen and the possible generated signals [11].*

Typically a modern TEM can display a magnified image of a specimen by the range of 2,000x to 1,500,000x. TEM generally works in high vacuum of the order of $10^{-10}$ mbar.

Figure 2.4 shows the interaction of an electron with the specimen. The incident electron (primary electron) scattered by the atom of the positively charged nucleus at an angle more than 90° is known as backscattered electrons. These electron electrons have the same energy as the primary electron. The electrons which are scattered by electrostatic interaction with the positively charged nucleus of an atom at an angle of less than 90º is known as elastically scattered electrons. Those electrons which loose its energy is known as in-elastically scattered electrons. Loosely bounded electrons which are mostly from the conduction band can easily be ejected are known as secondary electrons (SE). All the electrons or the radiation can be detected to get the information about the specimen. Different properties of the specimen such as topography, elemental composition, selected area electron diffraction (SAED) pattern can be deduced depending on the scattered electrons or radiations.

Figure 2.5 shows a schematic diagram of a TEM machine. A typical TEM consists of three major compartments i.e.: (1) an electron gun at the top of the column which produces broad electron beam due to heating of the wire by an electric current (thermo-ionic emission). The electron source generally is made up of tungsten wire or lanthanum hexaboride ($LaB_6$) because the work function id very low of those materials. The cathode and the control grids are kept in a negative potential and is isolated from the rest of the instrument. Then there is electron accelerator which accelerate the electrons. The electrons are accelerated in the range of 100kV-300kV. The condenser coils helps to focus the electron beam onto the specimen (sample). (2) The heart of the system is the objective lens which decides the ultimate resolution of the microscope. This compartment also contains the specimen stage, intermediate lens and projector lens. Projector lens focused the electrons, which are passing through the sample to form the clear and magnified image. The intermediate lens is of different strength so one can image the sample or record the diffraction pattern by changing the strength (3) The final part is called image-recording system. This is also very important part of the instrument where electron images are converted into some form which can be visible to human eye. This part of the instrument is consists of a fluorescence screen and CCD camera. The screen is used to visualize and focus the sample. The charge coupled device (CCD) camera is used to record the images.

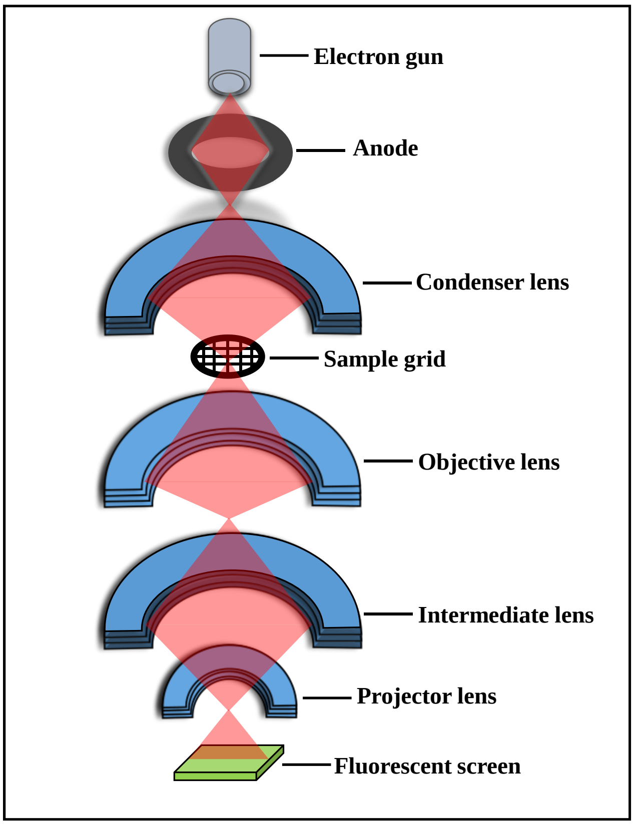

***Figure 2.5:*** *Schematic diagram of a TEM instrument.*

### 2.2.3 Atomic Force Microscopy (AFM)

Scanning Probe Microscopy (SPM) is truly a marvelous tool that provides the surface properties such as the local height, friction, magnetic properties, and constructs a map of this data to form an image of the surface. There are two category SPM that exist i.e. Scanning Tunneling Microscope (STM) and Atomic Force Microscopy (AFM). STM was invented by Gerd Binnig and Heinrich Rohrer [12] in 1981 for which they received the Noble prize in 1986. The problem with STM was it can only image materials that can conduct a tunneling current i.e. samples must be a conducting one like metals and semiconductors. To overcome this problem, Atomic Force Microscopy (AFM) was introduced by Gerd Binnig and Quate [13]**.** AFM is a microscopy technique in which 3-dimensional topographical images of all type of sample surface can be visualized. AFM which is used in laboratories can go down to atomic resolutions of $10^{-10}$ m or one tenth of nanometer. AFM can image all kinds of materials such as single molecules, semiconductor devices, nanoparticles, thin films, biological samples, etc.

A schematic diagram of the setup of the AFM can be seen in figure 2.6. AFM works on the principle that it measures the force between a sharp tip and the surface of the sample at a very short distance typically 0.2-10 nm separation. The sharp tip is connected to a flexible cantilever. The cantilever is made up of a very low spring constant material silicon nitride ($Si_3N_4$) or silicon. When the tip scans the sample surface, the force between tip and sample changes according to the sample surface. The force is measured using Hooke's Law which says that amount of force between the probe and sample is dependent on the spring constant of the cantilever and the distance between the probe and the sample surface.

$$F = -k.x \tag{2.2}$$

Where, F is force, k is spring constant (units of N/m) and x is the cantilever deflection. When the tip scans across the sample surface different types of interaction could occur i.e. capillary, Van der Waals forces, electrostatic, double layer forces, etc. While the tip moves above the sample surface, tip oscillates according to the sample surface topography and this induces a motion in the cantilever. To measure the induced motion in the cantilever, a high-gain transducer of cantilever deflection plus a feedback mechanism is needed.

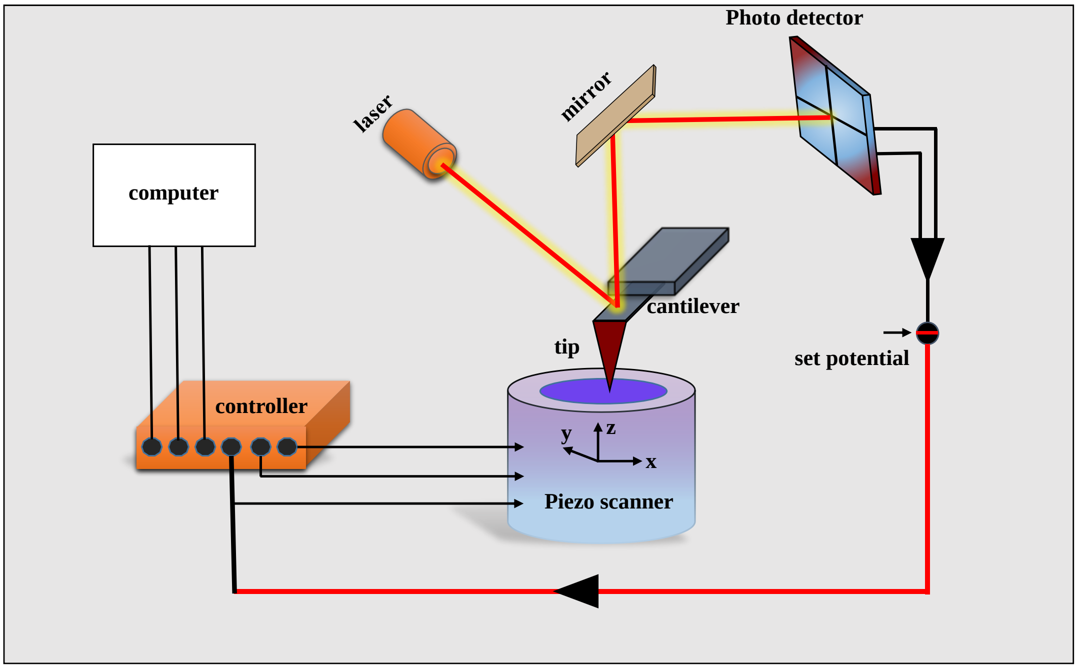

***Figure 2.6:*** *Schematic diagarm of an Atomic force microscopy (AFM).*

Among all techniques the optical beam deflection technique is often used to detect the cantilever deflection. A piezo-electric crystal is also used to maintain a constant bending of the cantilever. To detect the bending of the tip a laser light is used which is reflected from the backside of the cantilever towards a position-sensitive photodetector consisting of four side by side photodiodes. The deflected laser beam has information about the bending at the cantilever and can measure the actual position of the cantilever. There are three types of mode in which AFM generally works: contact mode, tapping mode, non-contact mode. The distance between the tip-sample and different forces is shown in figure 2.7. Contact mode is also known as repulsive mode where the tip is kept in soft physical contact with the sample surface. The tip moves across the samples and the topography of the sample surface is measured. The main drawbacks of this mode are that due to physical contact sample might get damaged and sometimes AFM tip breaks because of physical contact. Tapping mode is known as an attractive mode. This is the most preferred mode for high resolution topographical images for any kind of sample. In this mode, cantilever oscillates at a resonant frequency by a small piezoelectric material connected to the multimode AFM tip holder. The tip lightly touches or taps the surface while scanning and the oscillation vary from 10-100 nm. The last one is non-contact mode which is similar to tapping mode but here tip never touches the sample surface. The tip oscillates with small amplitude but the frequency is larger than its resonance frequency.

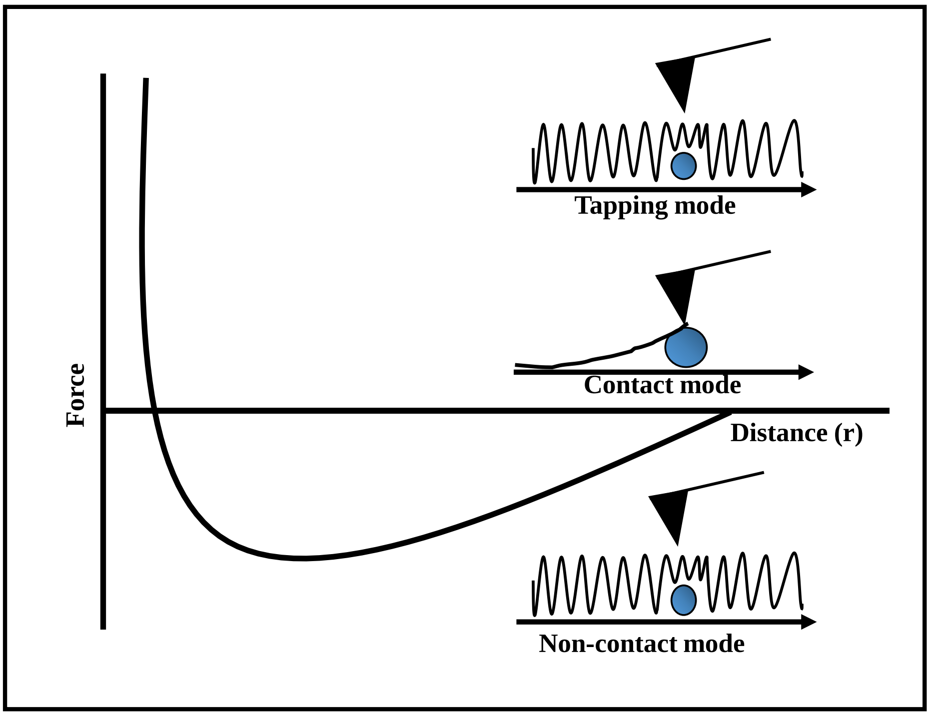

***Figure 2.7:*** *Different modes of AFM and tip-samples distance curve and interacting forces between them (concept from ref. [14]).*

### 2.2.4 Scanning electron microscopy (SEM)

The working principle of the scanning electron microscope (SEM) is very similar to the transmission electron microscope (TEM). SEM also uses the high energy electron beam to generate the signal from the sample after the interaction. The sample-electron interaction produces secondary electrons, backscattered electrons, photons, and diffracted backscattered electrons. Using SEM, we can study different properties of the sample such as morphology (texture), topography, crystalline structure, chemical composition, and orientation of materials.

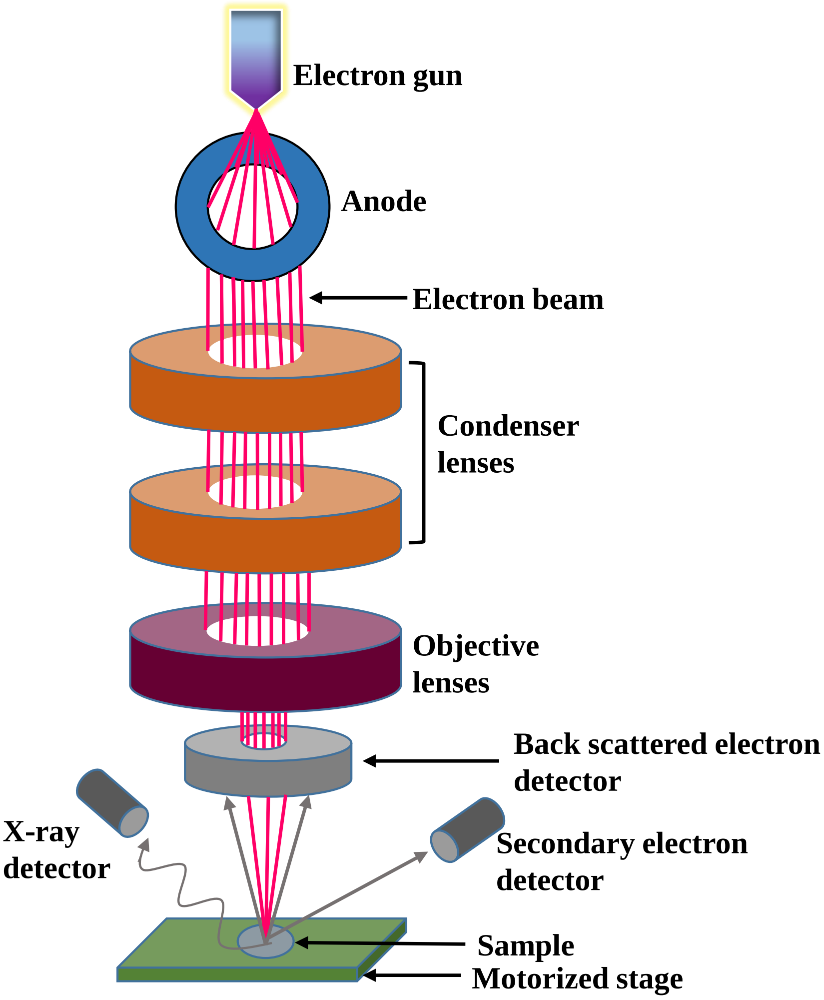

***Figure 2.8:*** *different components of a typical scanning electron microscope.*

Figure 2.8 shows a scanning electron microscopy setup and its different components. The electron gun is kept at top of the instrument which is generally made up of tungsten wire or a LaB6 material. Electron gun continuously produces electrons due to thermo-ionic process or field emission process. The electron then passes through a metal plate (anode) which accelerates the electron towards the lenses. To get high quality images without any aberration, the condenser lenses are used. These lenses make the electron beam as narrow as possible. Generally, one condenser lens is enough but two condenser lenses are used to produce a reduced image of the source. The first lens is strong which is adjustable to change the beam diameter and beam current and the second lens is to focus the electron beam into the objective lens. The main component of SEM is the objective lens which focuses the electron beam onto the sample and then form a primary image of the sample. Focusing of the image is done by changing the strength of the objective lens. Mostly secondary electrons are detected to produce SEM images of the sample. The backscattered electrons give the idea about the crystal structure and orientation of sample on any substrate. Another important feature of SEM is that it can give us the elemental composition of the sample. In this case, the electron has high energy to produce X-rays from the sample and those X-rays are then detected to get the elemental composition of the sample.

## 2.3 Magnetic characterization techniques:

### 2.3.1 Vibrating sample magnetometer (VSM)

Measuring the magnetization **M** (magnetic moment per unit volume) of any magnetic material always required the external magnetic field. Although there are few ways to measure the bulk magnetization of magnetic sample, such as,

(a) Force method: In this method a magnetic dipole is kept in a filed with gradient and the force experienced by the dipole is measured using an analytic balance. The change in the energy of a dipole in a magnetic field is given by,

$$E = -\frac{1}{2}\mu_0 m\boldsymbol{H} \tag{2.3}$$

If the change is in the x-direction then the force is given by,

$$F = -\frac{\partial E}{\partial x} = \frac{1}{2}\mu_0 V\,\frac{\partial(\boldsymbol{MH})}{\partial x} \tag{2.4}$$

For a ferromagnetic material M is constant so

$$F = -\frac{\partial E}{\partial x} = \frac{1}{2}\mu_0 V\boldsymbol{M}\frac{\partial(\boldsymbol{H})}{\partial x} \quad (2.5)$$

An important aspect of force measurement is that applied has been changing with respect to the position. An example which use the force method is alternating gradient magnetometer.

(b) Electrical method: Hall Effect magnetometer is an example of electrical method which measures the magnetization of the magnetic sample. In this method, the magnetic field is measured by measuring the hall voltage within the sample by the applied field then it is used to find out the net magnetization of the sample.

(c) Induction method: The vibrating sample magnetometer (VSM) is an example of the induction method. It is basically the application of Faraday's law induction which states that an electromagnetic force is generated in a loop coil when there is a change in flux through the pick-up coil. The induced e.m.f. is proportional to the rate of change of the field and the direction of the induced current is given by Lenz's law. VSM was first described by S. Foner, in 1959 [15,16] at the Lincoln laboratories. After this there were different types of VSM have been introduced [17–20] but the working principle is same for all the cases. Figure 2.9 shows the Quantum Design make PPMS (Model Evercool II) used in the present work. In a typical VSM, the magnetic sample is placed on a rod inside the cryostat. The chamber is placed inside the electromagnets which produced a uniform external magnetic field of different magnitude. The sample is connected to the rod which could vibrate vertically (vibrating sample magnetometer) at a certain given frequency. The pick-up coils are connected to the poles of the electromagnet. The magnetic flux associated with the pick-up coil changes due to the sample and induces an electromotive force in the coil. The induced flux is given by,

$$\phi(t) = \mu\mu_0\boldsymbol{H} \quad (2.6)$$

Where, μ is the point dipole and H is external applied magnetic field. If the sample is vibrated vertically then the induced voltage is given by,

$$V(t) = -N\frac{\partial\phi(t)}{\partial t}$$

$$V(t) = -N\frac{\partial\phi(t)}{\partial z}\frac{\partial z}{\partial t} \quad (2.7)$$

Where, N is the number of coils in the pick-up coils and z is the position of the sample along the vertical direction. The induced voltage is detected and measured by a lock-in amplifier. If we know the amplitude of the oscillation A, frequency of the oscillation f, where ω=2πf, then one can use the following equation to find out the magnetic moment of the sample,

$$V_{induced} = m\omega Ac \sin \omega t \tag{2.8}$$

Where c is the coupling constant and m is the magnetic moment of the sample. A typical PPMS-VSM has less sensitivity than SQUID but high sensitivity than conventional VSM. With a VSM one can find the complete information of magnetic thin films or nanoparticles or any other nanostructures or bulk samples. Various magnetic parameters such as, magnetic moment, coercivity, saturation magnetization and remanence can be found using a VSM (from M-H plot)

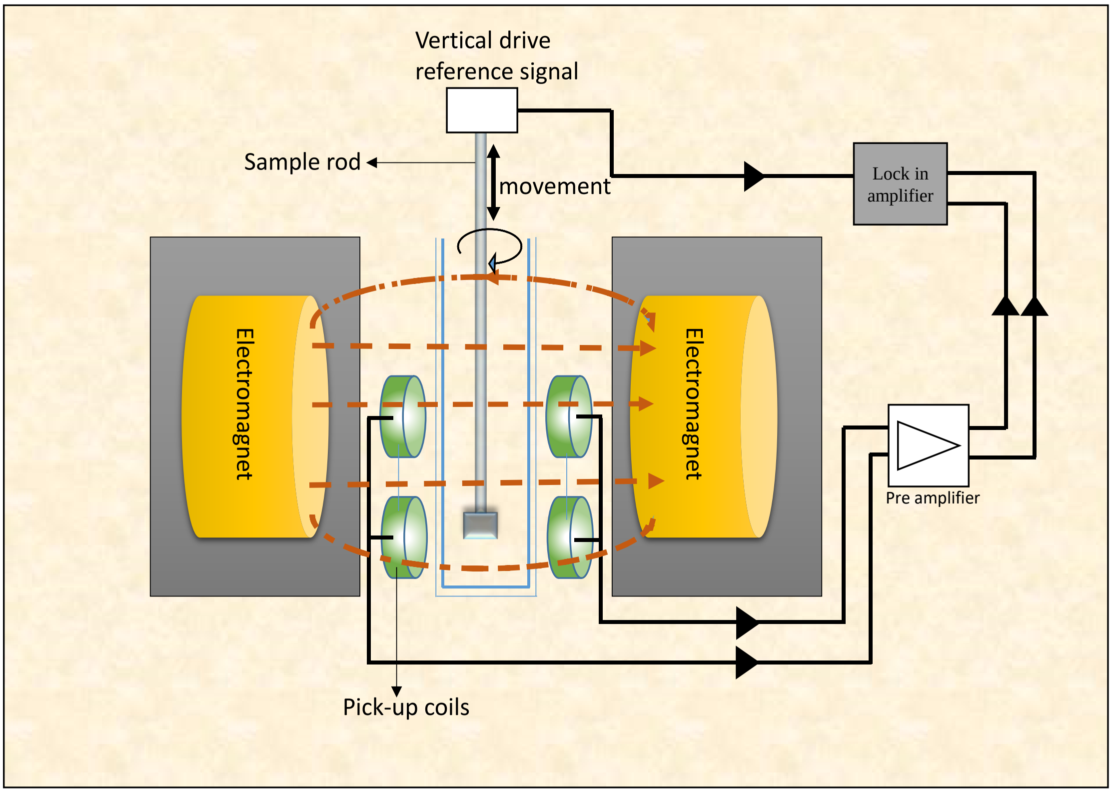

***Figure 2.9:*** *Schematic of a vibrating sample magnetometer (VSM)*

### 2.3.2 Superconducting quantum interference device (SQUID)

A typical SQUID [21,22] uses a Superconducting Quantum Interference Device magnetometer which can detect a tiny change in the magnetic flux. This technique is used to detect the magnetic property (AC and DC both) of magnetic samples. SQUID can detect and measures magnetic moment (m) of any given sample at various applied fields, **H**, and temperatures, T and using m, one can find out the magnetization of the sample. SQUID can also use as an ac susceptometer where a small alternating magnetic field **H** is applied and the time dependent response, m(t), is recorded. From these recorded data, one can calculate the ac susceptibility of the sample. SQUID technique is extremely sensitive and the sensitivity can reach up to $10^{-6}$ flux quanta of $\Phi_0$ variation in magnetic field that makes the SQUID possible to measure all kinds of magnetic samples including impurities even in low magnetic field strength.

The superconducting state, first observed in mercury by Heike Kamerlingh- Onnes in 1911. By cooling the mercury with liquid Helium-4, which boils at 4.2K, the resistance of mercury dropped sharply to a value close to zero at a certain temperature known as critical temperature $T_C$. Most of the normal superconductor has critical temperature almost from 1 K to 23 K. There are few ceramic based materials which have a high critical temperature ranging from 90 K to about 138 K. The most successful theory that explains the superconductivity was given by Bardeen-Cooper-Schrieffer (BCS theory) in 1957. According to BCS theory, lattice vibrations force the electrons to pair up into teams (Cooper pairs) that could pass all of the obstacles which caused resistance in the conductor.

The operation of SQUID is based on the Josephson junction effect [23]. This effect was proposed by B. D. Josephson in 1962 for which he was awarded the Nobel Prize in physics. Later this effect was experimentally observed in 1964 by Anderson and Rowell [24]. When two superconductors are separated by a layer of the insulator which is thin enough, superconducting electrons would be able to tunnel from one superconductor, through the thin gap to the other superconductor, resulting in the flow of a resistance less current through the insulator even with no voltage applied between them. Such currents are called Josephson currents and physical systems composed of two layer of superconductor that exhibit this type of property are called Josephson junctions. Figure 2.10 shown a simplified circuit for a dc SQUID magnetometer.

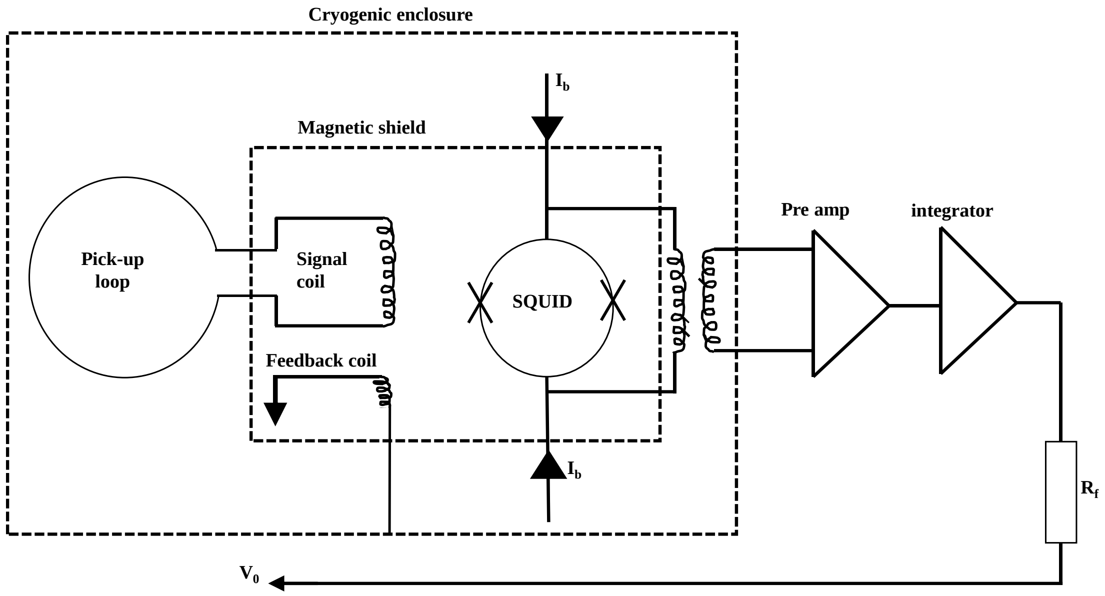

***Figure 2.10:*** *Simplified circuit for a dc SQUID magnetometer*

Flux quantization ($\Phi_0$) plays an important role to understand the dc SQUID working principle. An external magnetic field can penetrate a superconductor if and only if the magnetic field is an integer multiple of the magnetic flux quantum $\Phi_0$,

$$\Phi_0 = \frac{h}{2e} = 2 \times 10^{-15}\, Wb \tag{2.9}$$

where $h$ is the Planck's constant and $e$ is the charge of the electron. Figure 2.11 shows a pick-up-coil geometry along with the superconductor loop. In SQUID, magnetic flux is calculated in terms of voltage. A change in the voltage is monitored in order to determine the magnetic flux that is coupled to the superconducting loop. From Figure 2.11 it can be seen that a sample is mounted inside the pick-up coils (detection coil) and vibration (up down through the pick-up coils) is applied to the sample that leads to an alternating magnetic flux in the pickup coil. The pick-up coil is consists of a superconducting wire wound in a three coil configuration in a second order gradiometer geometry. The upper coil is a single turn wound clockwise, the center coil comprises two turns wound counterclockwise, and the bottom coil is again a single turn wound clockwise. The reason for this kind of configuration is that the detection coil can only sense the magnetic stray fields of the sample and any component coming from the external fields is canceled out. When the sample moves vertically kept inside the pickup coils, the magnetic moment of the sample induces an electric current in the pickup coils. This modification in the detection coil gives rise to a generation of persistent current in the pickup coils which is proportional to the change in the magnetic flux.

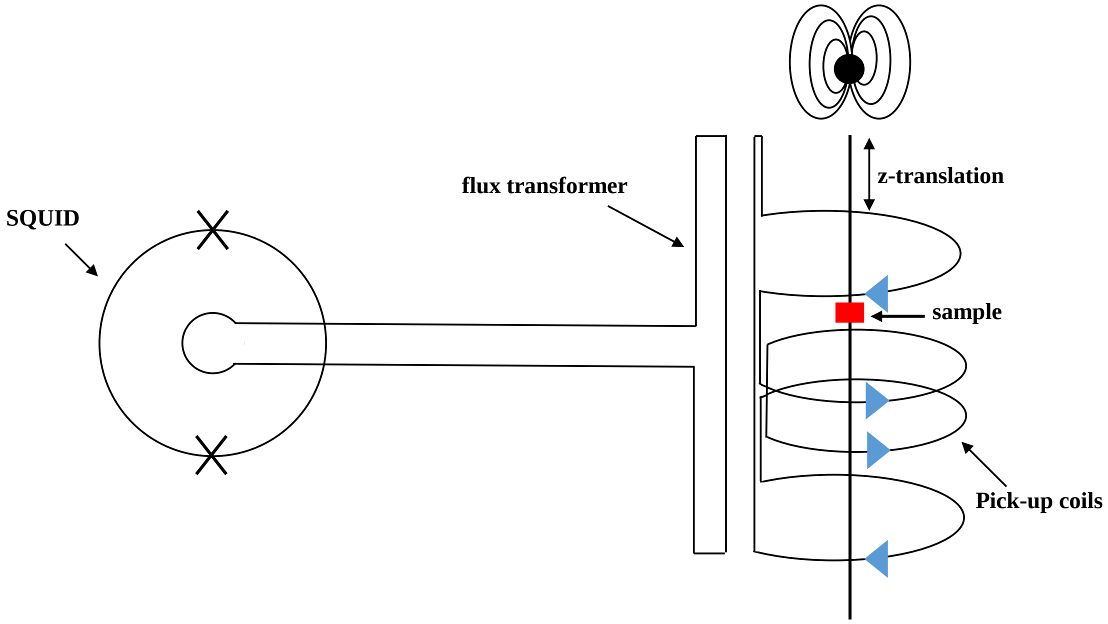

***Figure 2.11:*** *A typical pick-up coils geometry.*

The pickup coils, superconducting wires, and SQUID are connected in a loop so it then converts the magnetic flux into a voltage which is proportional to the magnetic moment of the magnetic sample.

### 2.3.3 Magneto Optical Kerr Effect (MOKE)

The basic and fundamentals of MOKE has already been discussed in the introduction chapter. Here, I will discuss the types and working priciple of MOKE. Depending upon the orientation of magnetization with respect to incident plane and sample plane, there are three types of MOKE effects. J. Kerr in 1875 while discovering Kerr effect, he used a pole of a magnet to reflect the incident light so this called polar MOKE (P-MOKE). So in P-MOKE spontaneous magnetization of the sample lies in perpendicular to the sample surface and parallel to the propagation vector of light. Second type is longitudinal MOKE (L-MOKE) where magnetization of the sample is in parallel to the sample surface. L-MOKE is responsible for both Kerr rotation and Kerr ellipticity and it is sensitive to in-plane component of magnetization. Last one is transverse MOKE (T-MOKE) where magnetization of the sample is parallel to sample surface but perpendicular to the plane of incidence. T-MOKE is responsible for the change in the intensity of reflected light by magnetic reversal.

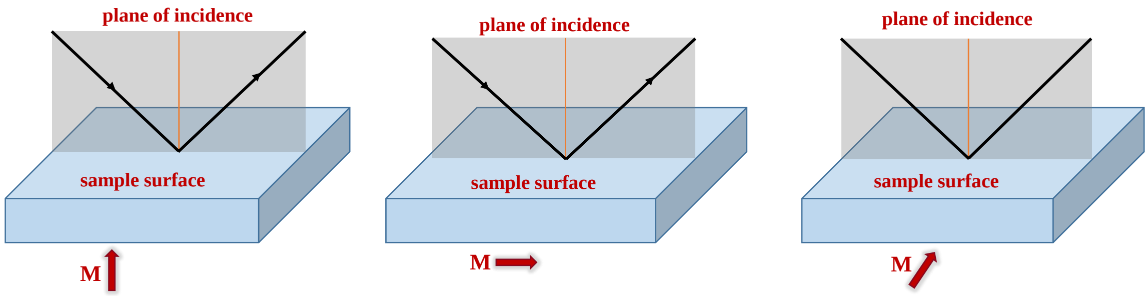

a. Polar MOKE b. Longitudinal MOKE c. Transverse MOKE

***Figure 2.12:*** *Different types of MOKE: (a) Polar MOKE, (b) Longitudinal MOKE, and (c) Transverse MOKE.*

When an incident light comes off from a magnetized sample generally two things happen, firstly its plane of polarization rotated over a small value known as Kerr notations ($\theta_K$) and secondly the reflected light become elliptically polarized known as Kerr ellipticity ($\varepsilon_K$). So, the mathematical equation is something like,

$$\Theta_K = \theta_K + i\varepsilon_K \tag{2.10}$$

Generally MOKE is described macroscopically by a dielectric tensors $\tilde{\varepsilon}$ (DK) [25]. Equation 2.10 can be written as,

$$\Theta_K = \theta_K + i\varepsilon_K = \frac{i\tilde{\varepsilon}_{xy}}{\sqrt{\tilde{\varepsilon}_{xx}}(1-\tilde{\varepsilon}_{xx})} \tag{2.11}$$

Where, $\tilde{\varepsilon}_{xx}$ and $\tilde{\varepsilon}_{xy}$ are diagonal and off-diagonal elements of the DK tensor, respectively. However, the off-diagonal term are linearly dependent on the magnetization. This is responsible for the magneto-optical response because there is different absorption of left and right circularly polarized light. On the other hand, the diagonal elements describes the optical reflectivity. The dielectric tensor in the case of magnetic material is in the form following matrix,

$$\tilde{\varepsilon} = \varepsilon \begin{pmatrix} 1 & iQ_z & -iQ_y \\ iQ_z & 1 & iQ_x \\ iQ_y & -iQ_x & 1 \end{pmatrix} \tag{2.12}$$

Where, $Q_x$ , $Q_y$ and $Q_z$ are proportional to the three components of the magnetization vectorin the material. Figure 2.13- a, b are the conventional MOKE set up for magnetomatry in different types of MOKE effect. At first the light beam passes through the liner polarizer from a laser source and a photo elastic modulator (PEM) superimposes

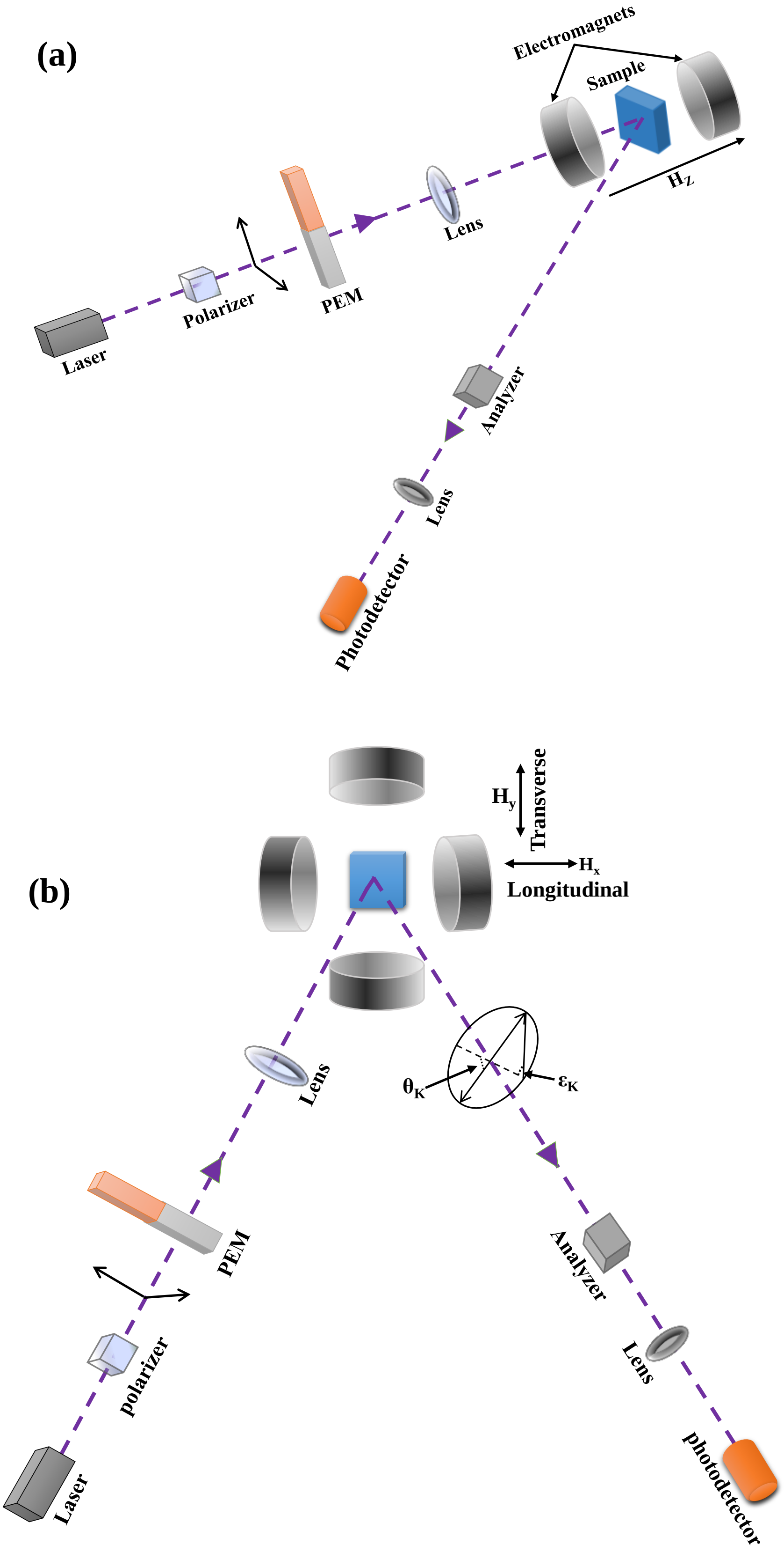

***Figure 2.13:*** *Schematic diagram of a MOKE in different configuration (a) polar and (b) longitudinal/transverse mode.*

periodic quarter-wave retardation (±λ/4 ) to this beam, before it reaches the sample. After the beam is reflected, the light beam again passes through a linear analyzer and then the signal is collected at the detector. Detailed discussion on MOKE technique is discussed in ref. [26,27].

The Kerr microscopy is a technique in which magnetic domain images can be recorded at each point of the hysteresis loop. Initially, this technique was considered weak method and it was difficult to record images of any sample which were not flat and smooth. On the other hand, this method was spatially limited by the diffraction criteria of the visible light. But with the development of imaging technique, Kerr microscopy is now considered as one of the best techniques for imaging magnetic domains because the contrast of non-magnetic background can be digitally subtracted from the contrast of magnetic domains. This technique is also faster than other techniques such as magnetic force microscopy (MFM), Lorentz transmission electron microscopy (LTEM), X-ray photoemission electron microscopy (XPEEM), etc. This technique is also non-destructive with local probing for the study of nanostructures.

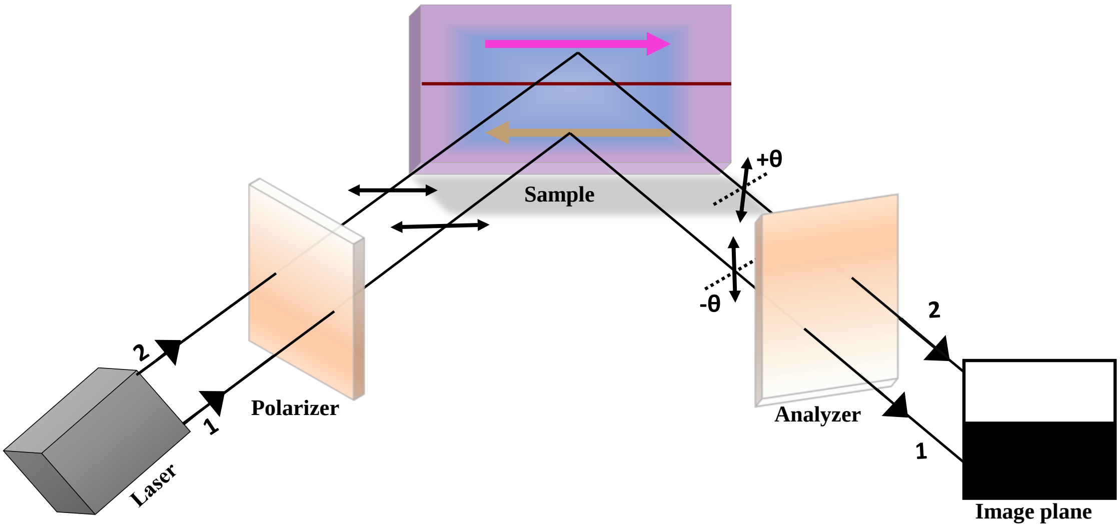

***Figure 2.14:*** *A conventional MOKE-microscopy setup for imaging magnetic domain.*

There are two types of Kerr microscopy, first one is wide-field microscopy which is mostly used and provides an absolute domain image of a certain sample area. Another one is laser-scanning microscopes, in which a laser spot is scanned relative to the sample surface building up the image sequentially. Wide-field microscopy technique is applied to the Köhler illumination technique, which was introduced in 1893 by A. Köhler from Carl Zeiss corporation, to obtain homogeneously illuminated images at maximum resolution. An experimental lay out of Kerr microscopy setup is shown in Fig. 2.14. Typically, light from an LED source passes through a polarizer and becomes plane polarized then the light incident on the magnetic sample. For magnetized sample let consider that the sample has two domain states which is anti-parallel to each other as shown in figure 2.14. After reflection, plane polarized light indicated by 2 might rotate by an angle +θ and the beam indicated by 1 rotated by the same angle but with opposite sign as they have interacted by oppositely magnetized domains. Now, if the analyzer is so adjusted that it is crossed with respect to reflected beam 1, this beam becomes extinguished and it will give the dark domain on the Kerr image. At the same time for beam 2 the analyzer is not crossed. So, beam 2 is not distinguished and hence the domain appears bright color. In this way, one can find the contrast between two different domains by Kerr microscopy. To improve the contrast of the image first one should take the reference image of the film in its saturated state, which was then substrate digitally from the subsequent images which contain the magnetic contrast. The Kerr microscope used for domain imaging in this thesis is manufactured by Evico Magnetic Ltd., Germany. The highest resolution of the microscope is obtained by oil immersion (n = 1.5) based 100X objective lens. For in-plane and out-of-plane magnetized systems, We have studied them in longitudinal and polar mode, respectively.

## 2.4 References:

[1] T. Kanomata, Y. Kitsunai, K. Sano, Y. Furutani, H. Nishihara, R. Y. Umetsu, R. Kainuma, Y. Miura, and M. Shirai, Phys. Rev. B **80**, 214402 (2009).

[2] A. U. B. Wolter, A. Bosse, D. Baabe, I. Maksimov, D. Mienert, H. H. Klauß, F. J. Litterst, D. Niemeier, R. Michalak, and C. Geibel, Phys. Rev. B **66**, 174428 (2002).

[3] M. Zhang, E. Brück, F. R. De Boer, Z. Li, and G. Wu, J. Phys. D. Appl. Phys. **37**, 2049 (2004).

[4] D. Rani, L. Bainsla, K. G. Suresh, and A. Alam, Phys. Rev. B **99**, 104429 (2019).

[5] A. Markou, D. Kriegner, J. Gayles, L. Zhang, Y.-C. Chen, B. Ernst, Y.-H. Lai, W. Schnelle, Y.-H. Chu, and Y. Sun, Phys. Rev. B **100**, 54422 (2019).

[6] G. Bonfiglio, K. Rode, K. Siewerska, J. Besbas, G. Y. P. Atcheson, P. Stamenov,

J. M. D. Coey, A. V Kimel, T. Rasing, and A. Kirilyuk, Phys. Rev. B **100**, 104438 (2019).

[7] S. Bosu, Y. Sakuraba, K. Uchida, K. Saito, T. Ota, E. Saitoh, and K. Takanashi, Phys. Rev. B **83**, 224401 (2011).

[8] W. Conrad, Singapore Med J **50**, 851 (2009).

[9] B. D. Cullity, Reading, MA 100 (1978).

[10] E. Ruska, Angew. Chemie Int. Ed. English **26**, 595 (1987).

[11] B. A. CARTER, D. B. Williams, C. B. Carter, and D. B. Williams, *Transmission Electron Microscopy: A Textbook for Materials Science. Diffraction. II* (Springer Science & Business Media, 1996).

[12] G. Binnig, H. Rohrer, C. Gerber, and E. Weibel, Phys. Rev. Lett. **49**, 57 (1982).

[13] G. Binnig, C. F. Quate, and C. Gerber, Phys. Rev. Lett. **56**, 930 (1986).

[14] M. Marrese, V. Guarino, and L. Ambrosio, J. Funct. Biomater. **8**, 7 (2017).

[15] S. Foner, Rev. Sci. Instrum. **30**, 548 (1959).

[16] S. Foner, J. Appl. Phys. **79**, 4740 (1996).

[17] K. M. Creer, A. De Sa, and W. O'Reilly, J. Sci. Instrum. **44**, 133 (1967).

[18] S. Legl, C. Pfleiderer, and K. Krämer, Rev. Sci. Instrum. **81**, 43911 (2010).

[19] N. F. Oliveira Jr and S. Foner, Rev. Sci. Instrum. **43**, 37 (1972).

[20] V. Lopez-Dominguez, A. Quesada, J. C. Guzmán-Mínguez, L. Moreno, M. Lere, J. Spottorno, F. Giacomone, J. F. Fernández, A. Hernando, and M. A. García, Rev. Sci. Instrum. **89**, 34707 (2018).

[21] C. D. Tesche, Cryogenics (Guildf). **29**, 1135 (1989).

[22] T. Ryhänen, H. Seppä, R. Ilmoniemi, and J. Knuutila, J. Low Temp. Phys. **76**, 287 (1989).

[23] B. D. Josephson, Rev. Mod. Phys. **36**, 216 (1964).

[24] P. W. Anderson and J. M. Rowell, Phys. Rev. Lett. **10**, 230 (1963).

[25] J. Zak, E. R. Moog, C. Liu, and S. D. Bader, J. Appl. Phys. **68**, 4203 (1990).

[26] C. Daboo, J. A. C. Bland, R. J. Hicken, A. J. R. Ives, M. J. Baird, and M. J. Walker, Phys. Rev. B **47**, 11852 (1993).

[27] W. S. Kim, M. Aderholz, and W. Kleemann, Meas. Sci. Technol. **4**, 1275 (1993).

# Chapter 3

## *Electrodeposited Heusler alloy films with enhanced magneto-optical property*

Growth of Heusler alloy films through techniques other than conventional physical vapor deposition presents a challenge for spintronic materials research. In this study, a novel electrochemical deposition scheme is developed for growing Heulser alloy films. By using magneto optic Kerr effect and Kerr microscopy measurements a systematic study of surface magnetization reversal behavior of these films is presented. The results demonstrate that the growth of sub-micron films of $Co_2FeSn$ (CFSn) leads to significant enhancement in magneto optic Kerr rotation. A large Kerr rotation value up to ≈ 300 mdegree was observed for thin films of thickness ≈ 200 nm. The modified scheme reported here opens up a path for exploration of electrochemical method as a facile route for fabricating Heusler alloys with improved surface property.

M. R. Karim, et.al. Mater. Today Commun. **25**, 101678 (2020)

## 3.1 Introduction:

Heusler alloy is an extraordinary class of intermetallic that is expected to be the material of the next generation spintronic devices [1,2]. Heusler compounds of the form $X_2YZ$, with Cobalt (Co) and Iron (Fe) being X and Y respectively, has been at the forefront of spintronic material research due to their useful properties like high Curie temperature, low Gilbert damping coefficient, and large spin polarization [3,4]. Tunnel magnetoresistance greater than 100% has been observed in magnetic tunnel junctions consisting of CoFe based Heusler alloys in combination with magnesium oxide barrier layer [5]. Recently, it has been predicted that CFSn can host topological properties with a large berry curvature [6]. Due to this a strong anomalous Nernst conductivity is expected in CFSn. Such topological properties are vital for spin based thermoelectric applications [7]. Furthermore, CFSn is a promising spintronic material as it is predicted to support large spin polarization current [8]. However, density functional theory calculations show that CFSn has formation energy of 0.05 eV/f.u. which makes it thermodynamically unstable [9]. As a result, CFSn alloy is prone to phase segregation and is challenging to grow even using UHV based physical evaporation methods [10].

As electrodeposition is a non-equilibrium process, it can be employed to grow films of CFSn [11] and $Fe_2CoSn$ alloys [12]. Additionally, the electrochemical method provides a huge advantage of flexibility and ease of growth compared to the vacuum based techniques. Following this, few attempts have been made to electrodeposit thick films of CFSn [11,13]. However, these electrodeposited films have been plagued by poor morphology marked by island-like growth with cracks and exhibited weak magnetic properties. Here we present, a modified three step scheme to electrochemically grow high quality CFSn thin films with excellent morphology. The films show high value of Kerr rotation reaching a value up to 300 mdegree. Intriguingly, our results show a thickness dependent giant enhancement of magneto-optic property of CFSn films.

## 3.2 Experimental methods:

CFSn thin films were electrodeposited on a polycrystalline copper plate. The CFSn films were deposited using a sulphate bath having neutral pH. The pH of the bath was controlled using NaOH solution. The electrochemical bath contained Sodium gluconate (0.57 M), boric acid (0.3 M), peptone (2.5 mg), along with $CoSO_4.7H_2O$ (0.075M), $FeSO_4.7H_2O$ (0.04M) and $SnSO_4$ (0.015M), as metal precursors for Co, Fe and Sn respectively. The solution was stirred for 1 hour to form a well-mixed electrolyte. Sodium gluconate was added to the electrochemical bath to act as a complexing agent that binds metal ions before they are electrodeposited. This reduces the propensity of metal oxide deposition. All the depositions were carried out at a constant voltage of -1.3 V in chrono-amperometry mode, using an electrochemical work-station [Autolab PGSTAT302N from Metrohm AG]. The choice of electrodeposition voltage was guided by the observation that higher voltage caused thicker films with poor morphology [11,13]. Figure 3.1-a shows the dependence of the atomic ratio of Fe:Co and Sn:Co on the electrodeposition voltage. Figure 3.1-(b-c) shows the variation of the atomic ratio of Fe:Co and Sn:Co on the molarity of sodium gluconate and $SnSO_4$ respectively used in the electrochemical bath.

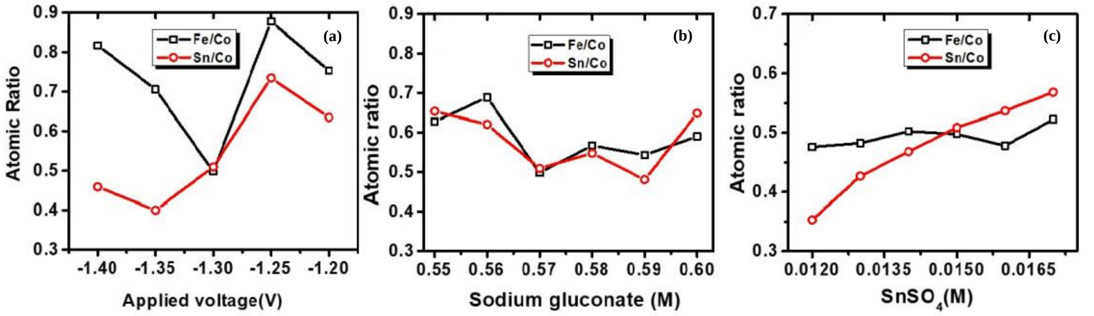

***Figure 3.1:*** *Variation of atomic ratio of Fe:Co and Sn:Co as a function of (a) electrodeposition voltage (b) molarity of sodium gluconate and (c) molarity of* $SnSO_4$

Prior to the growth of the films, the copper substrates were electropolished in a 50% phosphoric acid bath. The electropolishing time and voltage were optimized to fifteen minutes and 1.4 V respectively. A higher value for these parameters were found to enhance surface roughness, while lower values were insufficient to obtain a clean surface (Fig. 3.2 a-c). The introduction of the pre-deposition step was found to be critical in obtaining good quality films. Freshly cleaned substrates were immediately placed in a three electrode electrochemical cell for CFSn film deposition, wherein the electropolished copper was used as the working electrode. A platinum plate served as the counter electrode while Ag/AgCl was used as the reference electrode. The electrodeposited films were subsequently annealed at 200°C in argon (Ar) atmosphere for 2 hours.

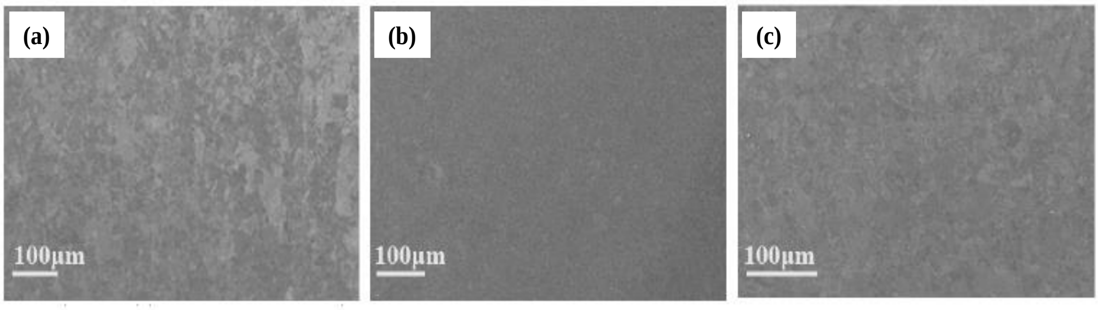

***Figure 3.2:*** *SEM images of copper substrate electropolished for (a) 5 minutes (b) 15 minutes (c) 30 minutes.*

The annealed films were rinsed with DI water to remove any other residual metal ions from the top of the film, leaving behind a smooth and a strongly reflecting intermetallic alloy surface. The three step process of pre-cleaning, electrodeposition and subsequent annealing, leads to a very high quality CFSn film is shown in figure 3.3.

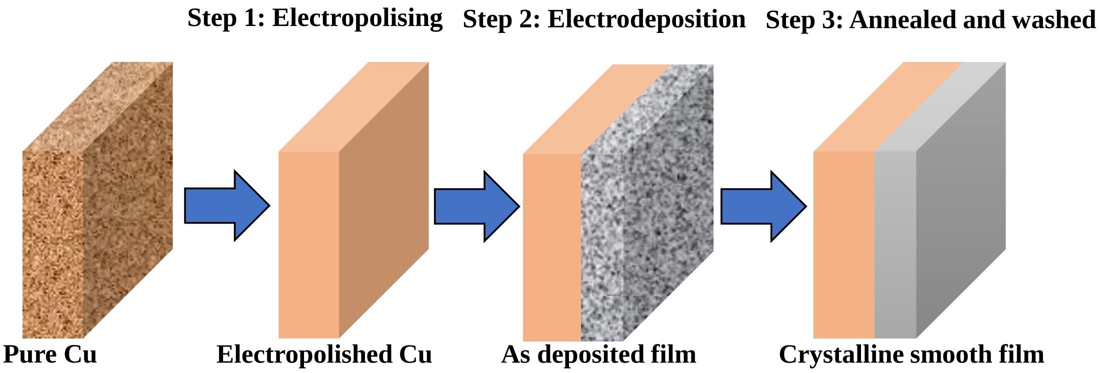

***Figure 3.3:*** *Schematic of three-step process followed to obtain smooth and crystalline Co$_2$FeSn film.*

## 3.3 Results and Discussion:

### 3.3.1 Structural analysis and morphology

The SEM images of rinsed and annealed CFSn film (Fig. 3.4-a), clearly exhibit significant improvement in the surface morphology compared to that of the as-deposited film ((Fig. 3.4-b). Energy dispersive X-ray analysis (Fig. 3.5) shows an elemental ratio of Co:Fe:Sn of 2(±0.1):1((± 0.1)):1(± 0.1) confirming stoichiometric growth of the CFSn films. The EDX spectra has no other peaks except Co, Fe, Sn and the substrate Cu. The quantity of oxygen was found to be negligible which indicate that suraface oxidation is very less on the deposited films.

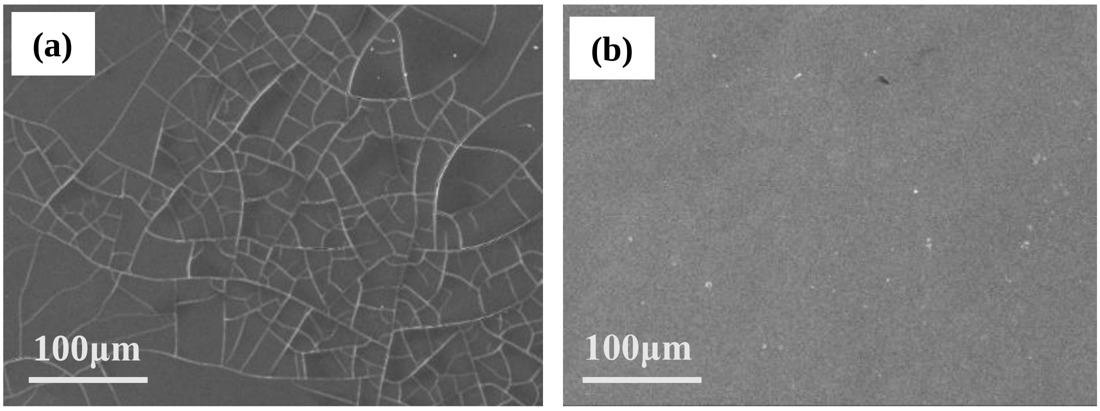

***Figure 3.4:*** *(a) SEM image of as-deposited $Co_2FeSn$ film (b) SEM image of annealed and deionized water rinsed CFSn film.*

The roughness of the CFSn films were found to be varying for different thickness. Roughness for films having thickness of ≈ 200nm and ≈ 1.5µm was found to be about ≈ 2.2nm and ≈ 1.8nm respectively (Fig. 3.6 a-b).

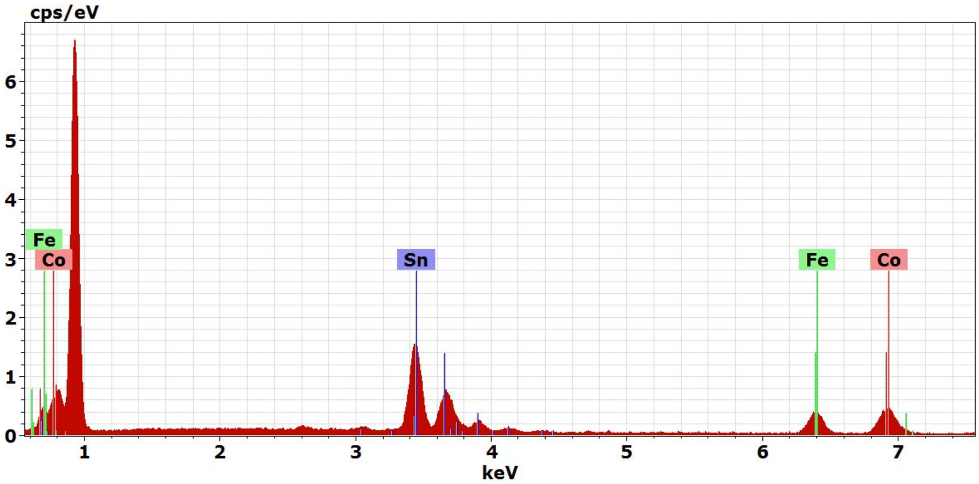

***Figure 3.5:*** *EDX spectra of annealed and deionized water rinsed $Co_2FeSn$ films.*

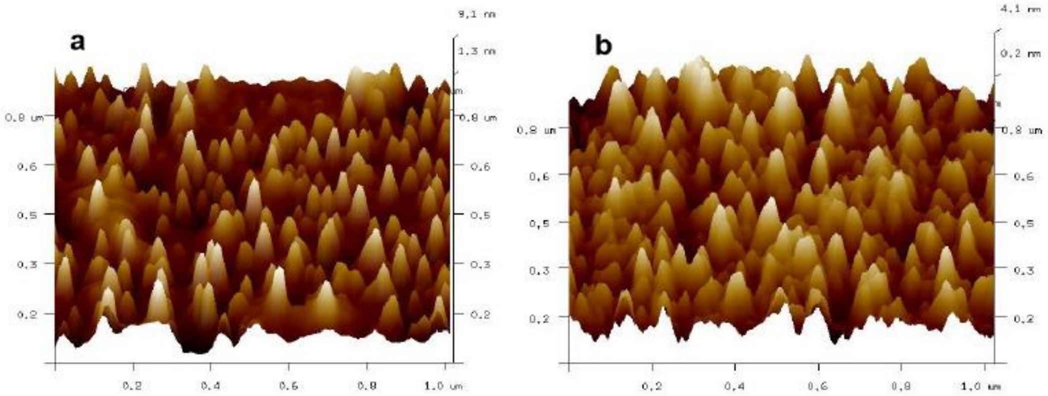

***Figure 3.6:*** *AFM images of $Co_2FeSn$ film having thickness about (a) 200nm and (b) 1.5µm.*

The grazing incidence X-ray diffraction (GIXRD) data (Fig. 3.7-a) show presence of three strong peaks around 43°, 51° and 74.5°. The diffraction peak at 43° (Fig. 3.7 a, b) has two components with one at 43.3° and the other at 43.4°. The intensity of the second peak at 43.4° is found to be more intense in GIXRD measurements (Fig. 3.7-b). As GIXRD is a surface sensitive technique, the observed second diffraction peak is related to the film. Furthermore the intensity of the 43.4° XRD peak is found to increase with the thickness of CFSn film (Fig. 3.7-b). Hence this peak can be associated to the crystalline order of the film. This peak is expected in the cubic B2 ordered CFSn system as the most intense Bragg reflection corresponding to (110) diffraction [14]. No other film related diffraction peaks were conspicuous in the measurements. Thus the XRD results indicate that the electrodeposited CFSn films could be of A2-type or of disordered-B2 type. The corresponding inter-planar spacing for (110) plane is 2.08 Å. No diffraction peaks corresponding to any binary phases of Co-Fe, Fe-Sn or Co-Sn was observed that confirmed absence of any phase segregation in these films.

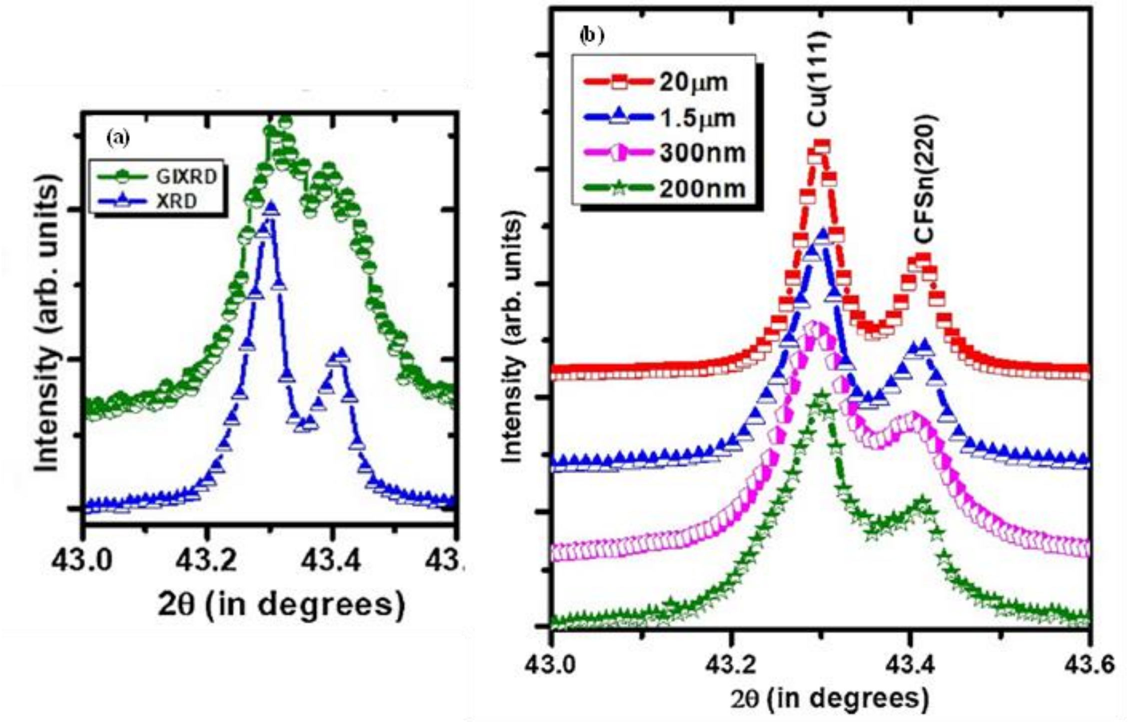

***Figure 3.7:*** *(a) Comparative plot showing both the GIXRD and conventional θ/2θ XRD scans for the same Co$_2$FeSn film. The GIXRD data clearly shows enhancement of peak intensity at 43.4°. (b) XRD of ≈ 20 μm, ≈ 1.5 μm, ≈ 300 nm and ≈ 200 nm thick films.*

The full width half maxima (β) of the film related peak obtained after subtracting instrumental broadening are, ≈0.048° and ≈0.033° for the thin (≤300 nm) and the thick films (≥1.5 μm) respectively. This can be used to roughly estimate a value of the strain (ε) in the film using the formulae $\varepsilon = \beta/4\tan\theta$, neglecting crystallite size broadening [15]. This yields a value of $\varepsilon \approx 0.013$ and ≈ 0.009 for the thin (≤300 nm) and the thick (≥1.5 μm) films, respectively. This indicates that the thin films have higher strain compared to that of the thicker films.

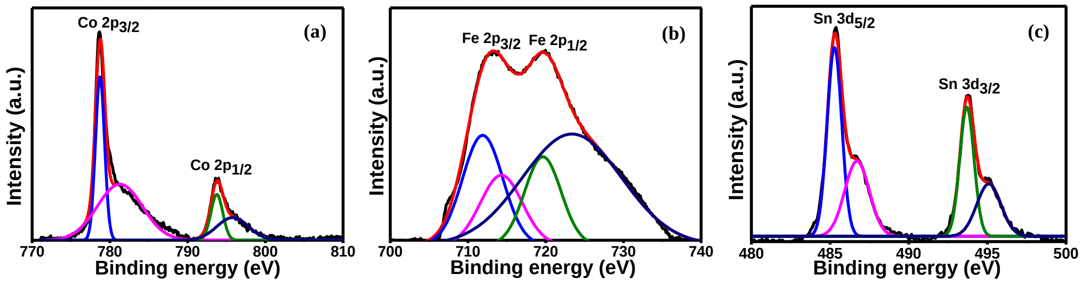

***Figure 3.8:*** *(a) High resolution de-convoluted X-ray photoelectron spectra (XPS) of Co 2p (b) XPS of Fe 2p and (c) XPS of Sn 3d.*

The X-ray photoelectron spectroscopy was performed using a photoelectron spectrometer at a base pressure of $\approx 10^{-7}$ Pa at room temperature with Al $K_\alpha$ x-ray source. The survey scan contains the photo emission peaks of Co, Fe Sn and low intense oxygen because of surface oxidation. To get more insight of the interfacial interaction the de-convoluted spectrum is plotted and shown in the figure 3.8 a-c. The core level of Co 2p is shown in figure 3.8-a. The photoemission of the due to Co $2p_{3/2}$ and Co $2p_{1/2}$ appears at ≈ 779 eV and ≈ 793 eV, respectively, which correspond to metallic phase of Co. The difference in the doublet of 2p is about 14 eV which is close to reported 15 eV energy. Figure 3.8-b shows the de-convoluted spectrum of Fe 2p peak. The spectrum has two peaks around ≈ 712 eV which correspond to $2p_{3/2}$ and ≈ 719.5 eV which is because of $2p_{1/2}$. The last plot (Fig. 3.8-c) shows the core level of Sn 3d peaks. The de-convoluted spectrum shows doublet peaks at ≈ 485 eV and ≈ 493 eV which correspond to $3d_{5/2}$ and $3d_{3/2}$ respectively of Sn.

### 3.3.2 Magneto-optical Kerr measurement (MOKE)

Longitudinal MOKE measurements were carried out on the electrodeposited films using a p-polarized laser light of 632 nm wavelength. The light was incident at an angle of ≈

45° on the film. The film was placed between an electromagnet. The reflected light passed through a photo-elastic modulator and was focused on an optical bridge detector. The reflected signal was measured using a lock-in amplifier. Magnetic domain imaging was carried out using a Kerr microscope equipped with an electromagnet.

The MOKE measurements (Fig. 3.9) of the electrodeposited CFSn films show room temperature ferromagnetism marked by clear appearance of a hysteresis loop. Films having thickness less than 300 nm (Fig. 3.9- a, b) exhibit large Kerr rotation, with a value of ≈0.3° for ≈200 nm film. The Kerr rotation value decreases with increase in film thickness (Fig. 3.9- c, d). For ≈ 1.5 μm film, the Kerr rotation reduces to ≈ 0.04°. Similar thickness dependence is observed for the coercive field that attains a value of 75 Oe for 200 nm film but reduces with increase in thickness. As the film roughness does not significantly vary with thickness, the observed strong magneto-optic response in the thin films indicate enhancement in surface ferromagnetic behavior of the submicron thick films. The variation of magneto optic response with the change in thickness can be related to the associated change in magnetic anisotropy. As the film thickness is reduced the shape anisotropy contribution [16,17] to the total magnetic anisotropy increases. This is also observed in the films grown here and is further discussed in the following paragraph. The shape anisotropy in thin films can lead to strong in-plane magnetization [16]. The strong in-plane magnetization results in enhanced longitudinal MOKE signal.

The hysteresis loops of CFSn thin films (≤300 nm) exhibit mildly wasp-waisted shape with weak signature of steps (marked by arrows in Fig. 3.9- a, b). Multistep loops have been earlier observed in magnetic [18] and Heusler alloy thin films having high degree of crystallinity [19]. This can occur either due to presence of two competing anisotropy [18] or due to complex domain structure comprising of simultaneous presence of different domains such as, 90° and 180° domains [19]. Competing magnetic anisotropy can appear in a well ordered cubic systems like Heusler alloy [19] due to presence of strong intrinsic magneto-crystalline anisotropy and an uniaxial anisotropy. The uniaxial anisotropy can either be caused by substrate-film interaction or by shape anisotropy.

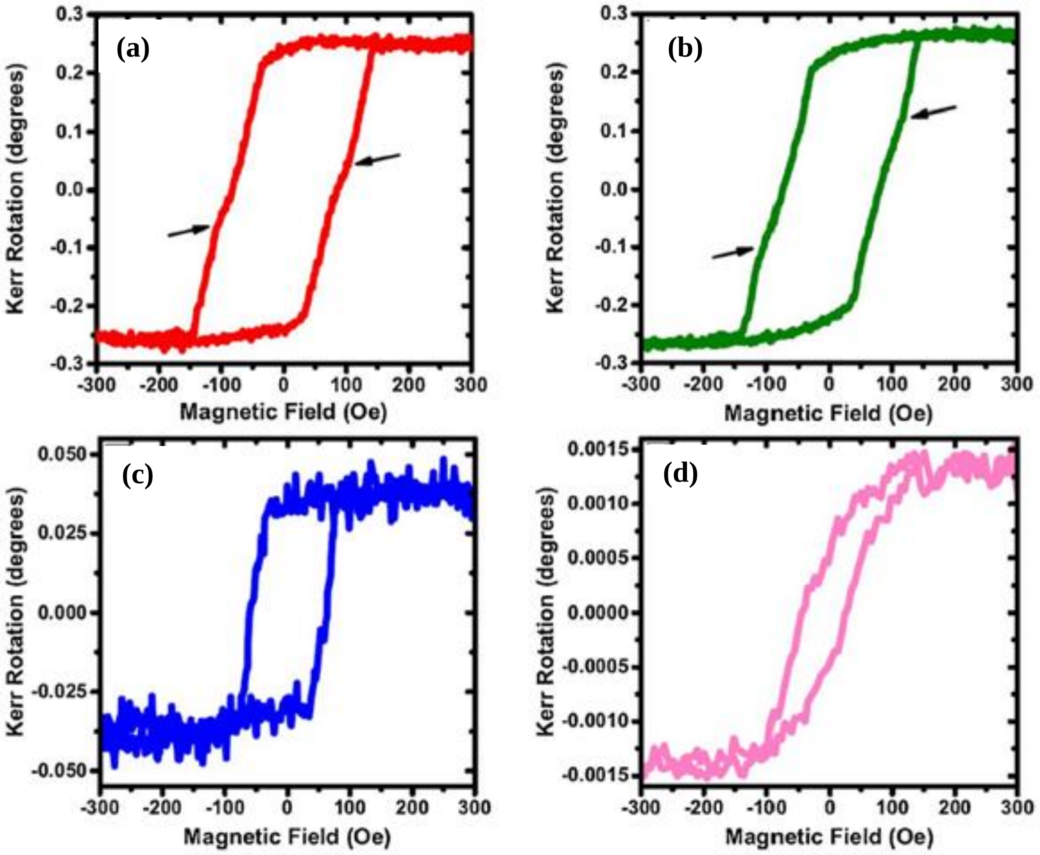

***Figure 3.9:*** *MOKE signal of $Co_2FeSn$ films having thickness (a) ≈ 200 nm, (b) ≈ 300 nm, (c) ≈1.5 μm, (d) ≈ 20 μm. The arrows in (a) and (b) indicates weak step-like feature in the hysteresis loop.*

Substrate mediated strain anisotropy is expected in ultrathin films grown on oriented substrates [20]. In this study the effect of substrate induced anisotropy can be ruled out as the films are grown on poly-crystalline copper. Furthermore, the shape of the hysteresis loop is found to change from wasp-waisted for thin films (Fig. 3.9-a, b) to continuously varying for thicker films (Fig. 3.9- c, d). This indicates that the observed competing anisotropy is thickness dependent. Hence, the observed anisotropy can be related to the shape anisotropy that increases with reduction of film thickness [21]. So, the observed weakly wasp-waisted loops can be attributed to the combination of the shape anisotropy and the magneto-crystalline anisotropy.

The Kerr microscopy images (Fig. 3.10) of magnetic domains in CFSn films show presence of two colors: one dark grey and the other light grey. The two colors show domains oriented in opposite direction without any complex domain structure. At large negative magnetic field a fully saturated dark grey image is observed. As the magnetic field is reduced to zero, the films stay in remanence and a dark grey image is primarily observed. However, as the field direction is reversed both the dark and the light grey regions are observed. This indicates simultaneous presence of opposite domains.

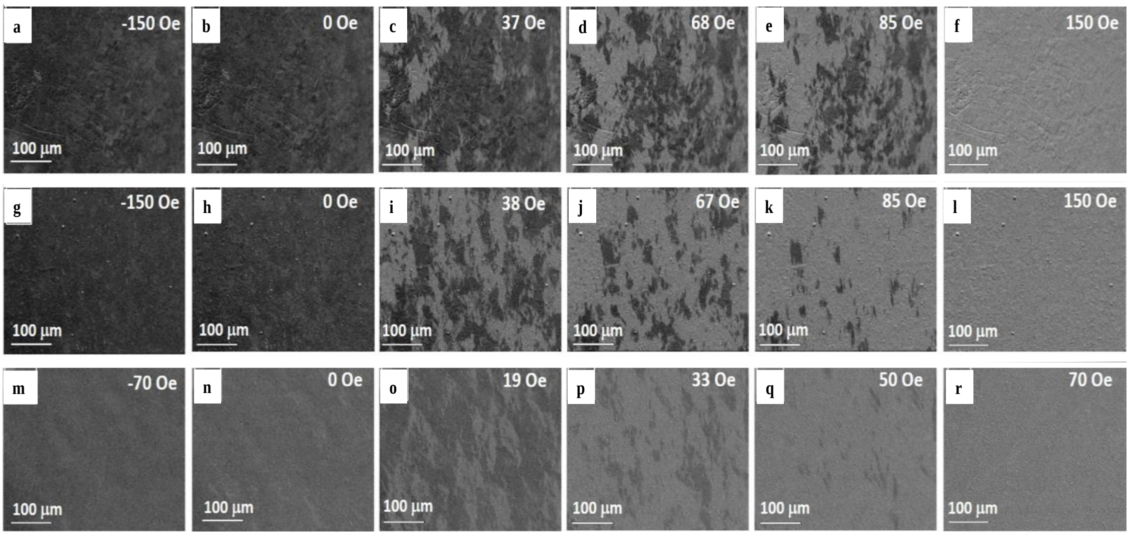

***Figure 3.10:*** *Magnetic domain images recorded at varying magnetic field for $Co_2FeSn$ film having thickness of (a–f) (≈ 200 nm) (g–l) (≈ 300 nm) and (m–r) (≈ 1.5 μm).*

The presence of oppositely oriented domains away from remanence is well known in cubic crystalline thin films [22,23]**.** Such opposite domains may be related to the fact that Heusler alloys are predominantly cubic crystalline system [24]. With the increase of magnetic field the light grey domains expand at the expense of the dark domains (Fig. 3.10 c–e, i–k, o–q). At the saturation field, a full light grey domain appears (Fig. 3.10 f, l, r) which indicates completion of magnetization reversal. This shows that magnetization reversal occurs primarily by domain-wall motion, wherein the domains in the direction of the magnetic field expands due to the domain-wall displacement [25]. The magnetization reversal in the thick (≈ 1.5 μm) film occurs at much lower magnetic field compared to that in the thin films. This occurs because the saturation magnetization field is lower in the case of the thick films compared to that of thin films.

To check the anisotopry, we have changed the angle angle between the sample surface and the angle of applied magnetic field. Interestingly, the hysteresis loop (Fig. 3.11) does not change as such with the applied field.

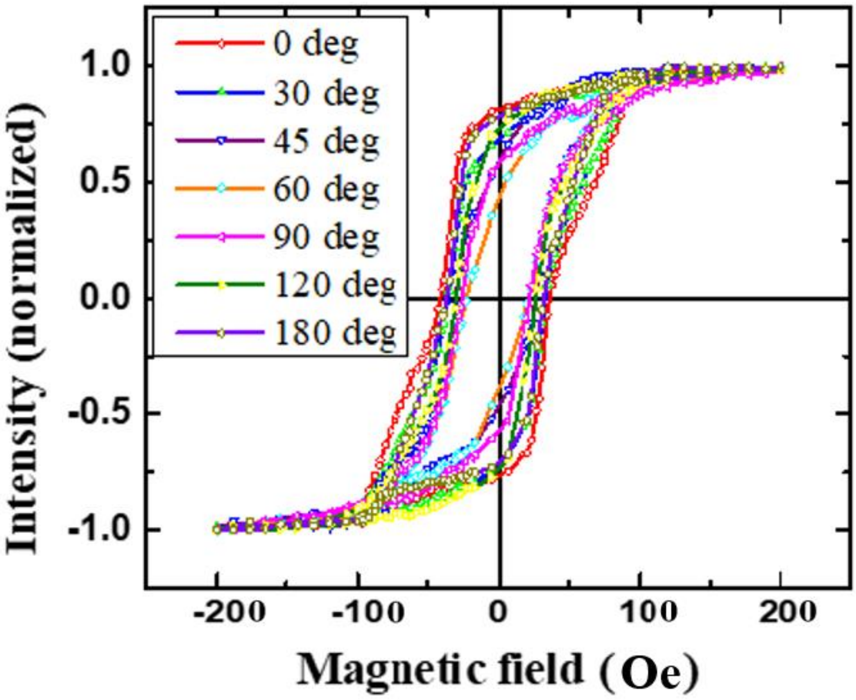

***Figure 3.11:*** *The hysteresis loop of the film with different angle of applied magnetic field with the sample suraface.*

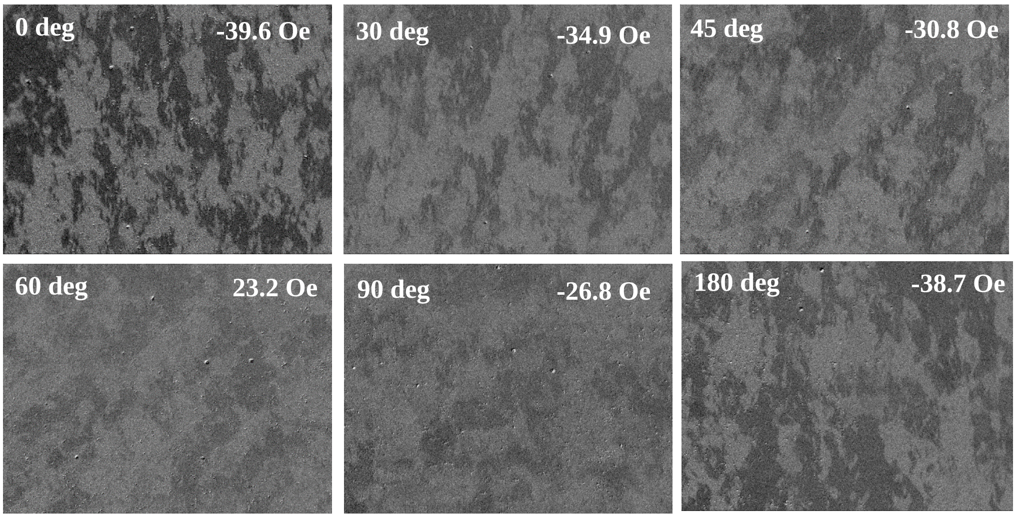

***Figure 3.12:*** *MOKE microscopy images at different angle and coercive field.*

The MOKE microscopy images has aslo been takem at the coercive field of the hysthesis loop (Fig. 3.12). At the coercive field the, the domains are randamly oriented at any direction so the dark grey and the light grey colours are randamly oriented.

### 3.3.3 Vibrating sample magnetometer (VSM) measurements

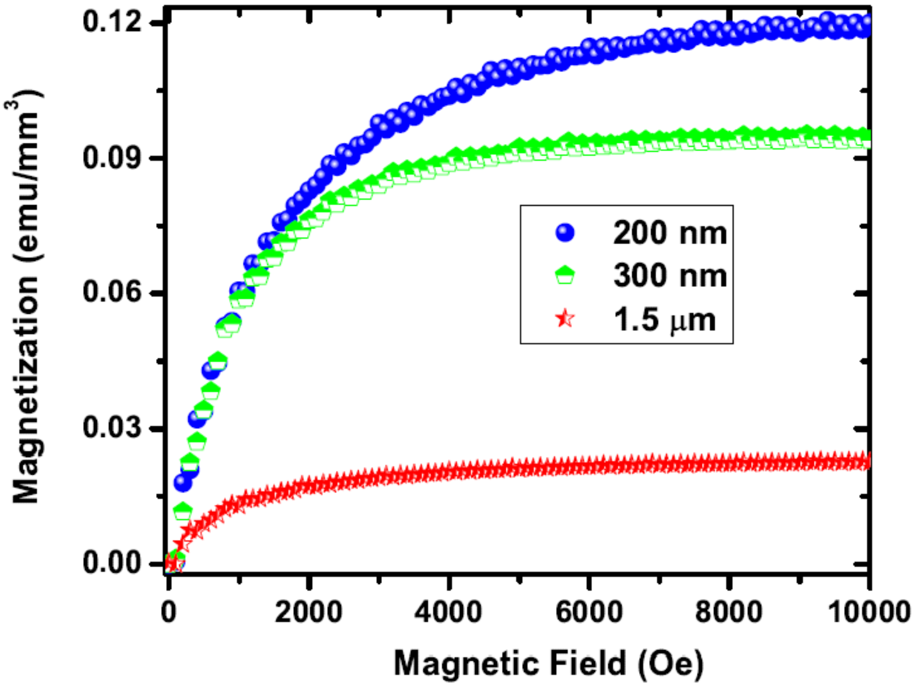

***Figure 3.13:*** *Room temperature magnetization vs magnetic field plot, for $Co_2FeSn$ films of varying thickness.*

Figure 3.13 shows room temperature magnetization (magnetic moment per unit volume) measurement on CFSn films as a function of in-plane applied magnetic field. The saturation magnetization is found to increase with the decrease in the film thickness. The saturation magnetization (saturation magnetic moment per unit volume) value is found to be ≈ 0.12 emu/mm$^3$ for the ≈ 200 nm thick film compared to a value of ≈ 0.02 emu/mm$^3$ in the ≈ 1.5 μm thick film. This enhancement in magnetization is in consistence with the observed thickness dependent increase in magneto-optic response in the thin films. Using the predicted lattice constant of 6 Å for CFSn [8], the corresponding value of magnetic moment for the ≈ 200 nm thick film is about 2.6 $\mu_B$ per unit cell.

## 3.4 Conclusion:

In summary, the possibility of electrochemical growth of Heusler alloy film with sub-micron thickness control without using physical vapor deposition methods has been demonstrated [26]. The results show that electrodeposited CFSn films of sub-micron thickness exhibit magneto-optical Kerr rotation comparable to the values observed in highly ordered Co-based Heusler films grown by conventional vacuum deposition methods [26]. The electrodeposited films show significant improvement in their magneto optical property at sub-micron thickness. This work is paradigm to realize novel intermetallic alloy films for magneto optical applications.

## 3.5 References:

[1] J. Winterlik, S. Chadov, A. Gupta, V. Alijani, T. Gasi, K. Filsinger, B. Balke, G. H. Fecher, C. A. Jenkins, F. Casper, J. Kübler, G.-D. Liu, L. Gao, S. S. P. Parkin, and C. Felser, Adv. Mater. **24**, 6283 (2012).

[2] S. Sanvito, C. Oses, J. Xue, A. Tiwari, M. Zic, T. Archer, P. Tozman, M. Venkatesan, M. Coey, and S. Curtarolo, Sci. Adv. **3**, e1602241 (2017).

[3] X. Zhang, H. Xu, B. Lai, Q. Lu, X. Lu, Y. Chen, W. Niu, C. Gu, W. Liu, and X. Wang, Sci. Rep. **8**, 1 (2018).

[4] J.-P. Wüstenberg, R. Fetzer, M. Aeschlimann, M. Cinchetti, J. Minár, J. Braun, H. Ebert, T. Ishikawa, T. Uemura, and M. Yamamoto, Phys. Rev. B **85**, 64407 (2012).

[5] L. M. Loong, W. Lee, X. Qiu, P. Yang, H. Kawai, M. Saeys, J.-H. Ahn, and H. Yang, Adv. Mater. **28**, 4983 (2016).

[6] J. Noky, J. Gooth, C. Felser, and Y. Sun, Phys. Rev. B **98**, 241106 (2018).

[7] S. N. Guin, P. Vir, Y. Zhang, N. Kumar, S. J. Watzman, C. Fu, E. Liu, K. Manna, W. Schnelle, J. Gooth, C. Shekhar, Y. Sun, and C. Felser, Adv. Mater. **31**, 1806622 (2019).

[8] H.-L. Huang, J.-C. Tung, and G.-Y. Guo, Phys. Rev. B **91**, 134409 (2015).

[9] M. Meinert and M. P. Geisler, J. Magn. Magn. Mater. **341**, 72 (2013).

[10] M. A. Tanaka, Y. Ishikawa, Y. Wada, S. Hori, A. Murata, S. Horii, Y. Yamanishi, K. Mibu, K. Kondou, T. Ono, and S. Kasai, J. Appl. Phys. **111**, (2012).

[11] J. Duan and X. Kou, J. Electrochem. Soc. **160**, D471 (2013).

[12] S. Gao, Y. Liu, and X. Kou, Int. J. Electrochem. Sci. **10**, 8727 (2015).

[13] N. Watanabe, K. Sano, N. Tasugi, T. Yamaguchi, A. Yamamoto, M. Ueno, R. Sumiyoshi, T. Arakawa, and I. Koiwa, APL Mater. **3**, 1 (2015).

[14] T. Li, J. Duan, C. Yang, and X. Kou, Micro Nano Lett. **8**, 143 (2013).

[15] H. P. Klug and L. E. Alexander, *X-Ray Diffraction Procedures: For Polycrystalline and Amorphous Materials* (1974).

[16] J. Bransky and A. A. Hirsch, Physica **34**, 349 (1967).

[17] A. Kehlberger, K. Richter, M. C. Onbasli, G. Jakob, D. H. Kim, T. Goto, C. A. Ross, G. Götz, G. Reiss, T. Kuschel, and M. Kläui, Phys. Rev. Appl. **4**, 14008 (2015).

[18] R. P. Cowburn, S. J. Gray, and J. A. C. Bland, Phys. Rev. Lett. **79**, 4018 (1997).

[19] S. Husain, V. Barwal, A. Kumar, R. Gupta, N. Behera, S. Hait, N. K. Gupta, P. Svedlindh, and S. Chaudhary, J. Magn. Magn. Mater. **486**, 165258 (2019).

[20] O. Thomas, Q. Shen, P. Schieffer, N. Tournerie, and B. Lépine, Phys. Rev. Lett. **90**, 17205 (2003).

[21] N. A. Usov and O. N. Serebryakova, J. Magn. Magn. Mater. **453**, 142 (2018).

[22] S. Mallik, N. Chowdhury, and S. Bedanta, AIP Adv. **4**, 97118 (2014).

[23] R. P. Cowburn, S. J. Gray, J. Ferré, J. A. C. Bland, and J. Miltat, J. Appl. Phys. **78**, 7210 (1995).

[24] A. Hirohata, W. Frost, M. Samiepour, and J. Kim, Materials (Basel). **11**, 105 (2018).

[25] S. Chikazumi, Phys. Ferromagn. Oxford University Press, 249 (1997).

[26] M. R. Karim, D. Panda, A. Adhikari, P. Sharangi, P. Mandal , S. Ghosh , S. Bedanta, A. Barman, and I. Sarkar, Mater. Today Commun. **25**, 101678 (2020).

# Chapter 4

## *Growth and magneto optical response of electrochemically prepared crystalline and ordered Heusler alloy film*

Electrochemical growth of Heusler alloy film with good morphological quality and crystalline order by using single crystalline substrate is demonstrated. The film shows good crystalline property with a finite $L2_1$ ordering. Static magneto optic Kerr effect studies are employed to reveal the surface magnetization reversal of the films. MOKE measurements reveal the presence of strong uniaxial anisotropy. The results presented here open up an opportunity to further explore electrochemically grown intermetallic alloy films on crystalline substrates, for realizing possible magneto optical and spintronics applications.

M. R. Karim, et.al. J. Phys. Chem. C **125**, 10483 (2021).

## 4.1 Introduction:

Intense research over the last decade has established Cobalt (Co) based full Heusler alloys (FHA) as the frontrunner material for various spintronic applications. Especially, $Co_2FeX$ FHAs (X being sp-element), show extremely useful properties of large spin polarization, low magnetic damping and high Curie temperature [1–4]. Due to such exceptional properties, FHAs show large magnetoresistance when used as a spin polarizing layer in magnetic tunnel junction (MTJ**)** [5–7]. Conventionally, high vacuum evaporation methods have been used to grow Heusler alloy. However, some studies have explored the possibility of using electrochemical methods to grow Heusler alloy films, especially for those that are thermodynamically hard to grow using conventional methods [8,9]. Electrochemical method opens up an opportunity of both ease and cost optimization of the growth process. But the earlier attempts of electrochemical growth of Heusler alloy, has shown limited success in achieving crystalline order as well as good morphological quality of the films. This may be related to the fact that these electrochemical growth have been carried out on polycrystalline metallic plates [8–10].

In this study, we explore the possibility of electrochemical growth of $Co_2FeSn$ (CFSn) Heusler alloy films on ultrathin metal films, supported on single crystalline silicon substrate. CFSn is an important candidate in the Co based FHA material class, as recent theoretical calculations predict that it has a large Berry curvature and can exhibit topological effects [11]. The growth of CFSn thin films using sputtering method has been found to be di-cult and prone to phase segregation [12]. It has been proposed that electrodeposition being a non-equilibrium process can be used to grow CFSn films [8,9]. Earlier attempts of electrodeposition of Heusler alloy films have used two possible growth mode. These modes are namely, the constant voltage deposition (potentiostatic) [8] and the constant current deposition (galvanostatic) mode [9]. However, irrespective of the electrodeposition mode employed, the films were grown on polycrystalline copper substrates. These films were found to show poor morphology along with A2 type disordered Heusler phase.

Here we report, the growth of CFSn thin films on Pt(2nm)/Ta(2nm)/Si(111) substrate. Our results show a remarkable improvement in the crystalline quality of the electrochemically grown Heusler alloy films, compared to the earlier studies of growth on polycrystalline substrates. We employ magneto optical measurements to study the surface magnetic behavior of these films using static Magneto optic Kerr effect (MOKE). Angle dependent MOKE is routinely used to study the magnetic anisotropy of Co based Heusler alloys [13]. Angular dependent MOKE measurements on these films show presence of a uniaxial anisotropy.

## 4.2 Experimental methods:

The electrodeposition process requires metallic electrodes for driving stable current through the electrochemical cell. Platinum is a stable electrode material that shows high degree of chemical inertness. A Ta under layer is known promote crystalline growth and adhesion of Pt on Si(111) surface [14]. At first Ta and Pt was deposited on a Si(111) substrate using DC magnetron sputtering. The base pressure prior to sputtering was better than 1 x $10^{-8}$ mbar. The Pt(2nm)/Ta(2nm)/Si(111) substrate was subsequently used as the substrate for the electrodeposition of CFSn films. Immediately prior to the electrodeposition, the substrate were electropolished in a 50% phosphoric acid bath. The CFSn films were electrodeposited from a sulfate solution bath using an electrochemical workstation (Autolab, Metrohm AG). Following previous reports [8,9], the electrochemical bath was composed of a thoroughly mixed solution of sodium gluconate (0.57 M), boric acid (0.3 M), peptone (2.5 mg), along with $CoSO_4.7H_2O$ (0.075M), $FeSO_4.7H_2O$ (0.04M) and $SnSO_4$ (0.015M). The growth of thin films was carried out by employing a modified approach of electrodeposition and subsequent annealing. The annealing was done at 200 °C under argon atmosphere. Annealing at higher temperature was found to be detrimental for the sample. The annealed samples were mildly dipped in and out of distilled water to remove any unreacted residual metal ions from the surface. During the electrodeposition, the substrate acted as the working electrode while a platinum plate served as the counter electrode along with a Ag/AgCl as the reference electrode.

X ray diffraction (XRD) measurements of these films were carried out at the high resolution hard X-ray diffraction (BL-18B) beamline, using the synchrotron light source of the photon factory, Japan. The XRD data was collected using monochromatic X ray photons having wavelength of 0.884 Å. The details of XRD results are discussed later. Magnetization versus temperature measurements were carried out using SQUID magnetometer (MPMS3) designed by Quantum design, US. Measurements were carried out following two protocols, namely, zero field cool (ZFC) and field cool (FC). ZFC and

FC measurements were respectively carried out by cooling the sample in absence and presence of magnetic field. In both cases, magnetization was measured during the warming cycle at 30 Oe magnetic field. Magneto optic measurements were carried out on ≈ 100nm thick CFSn films at room temperature. Static MOKE measurements were carried out in longitudinal geometry, with simultaneous recording of the hysteresis loops along with magnetic domain images. The MOKE data was collected under the application of variable in-plane magnetic field using Kerr magnetometer and microscope, manufactured by Evico Magnetics Ltd., Germany. Angle dependent MOKE measurements were performed by varying the angle between the external magnetic field and the easy axis of the sample at 10° interval.

## 4.3 Results and discussion:

### 4.3.1 Structural analysis and morphology

The EDX analysis of the films (Fig. 4.1- a), shows a stoichiometric growth of 2(±0.01):1(±0.01):1(±0.01) of Co: Fe: Sn. The EDX spectra has no extra peak other than the CFSn and Si peak. This indicates that the film has no oxide or any other phase other than the CFSn and substrate peak.

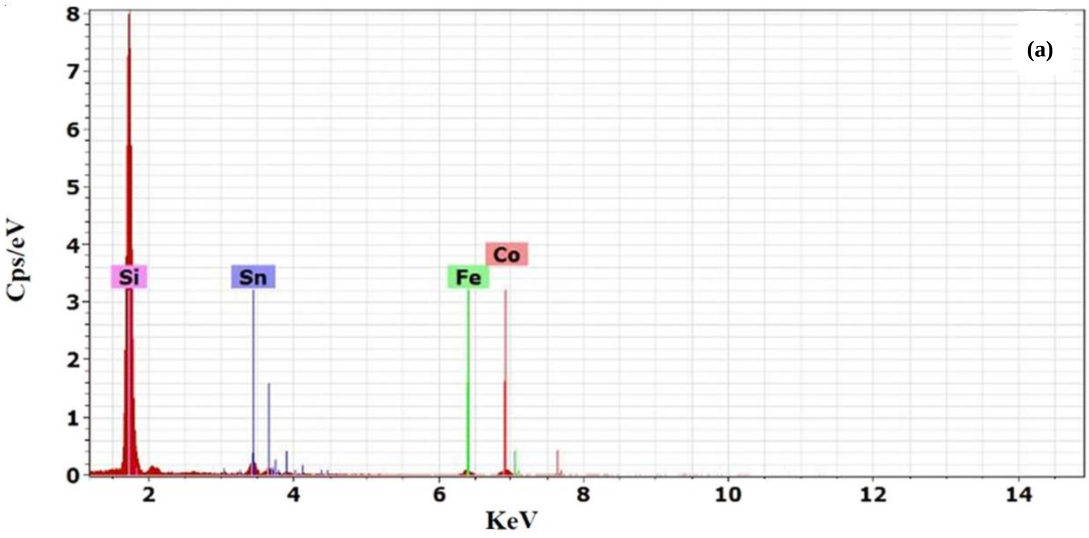

***Figure 4.1:*** *(a) EDX spectra of the deposited film.*

The AFM measurement of the CFSn films (thickness≈ 100 nm) shows a roughness of about 1.8 nm (Fig. 4.2-b). The measured roughness is less compared to the films grown on the polycrystalline copper substrate.

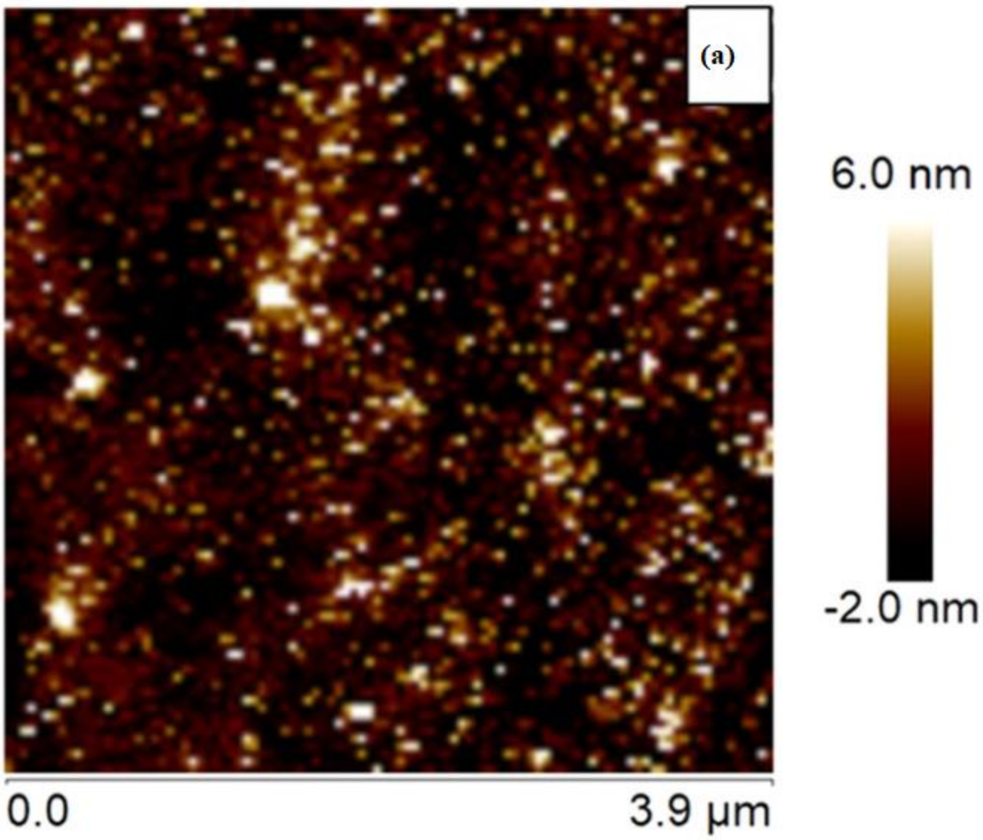

***Figure 4.2:*** *(a) AFM image of $Co_2FeSn$ film.*

The XRD data (Fig. 4.3) of CFSn film shows crystalline peaks at around 14.9°, 24.7° and 34.9°, in addition to the substrate related peaks. These peaks respectively corresponds to [111], [220] and [400] reflections of CFSn. This is consistent with the XRD simulation of $L2_1$ ordered CFSn with a lattice parameter of 5.9 Å. The diffraction pattern calculations were carried out using powdercell program, with Co, Fe and Sn occupying Wyckoff positions of 8c, 4a and 4b respectively [15]. Both the experimental data and the theoretical calculation show that the [220] reflection is the most intense diffraction peak. This is subsequently followed by the peak of [400] and [111] in the descending order of intensities. The appearance of [111] peak albeit with relatively low intensity, clearly reveals that CFSn forms an ordered crystalline phase with weak $L2_1$ order. The degree of $L2_1$ ordering could not be determined from the experimental data due to the overlapping background signal from the substrate related diffraction peaks.

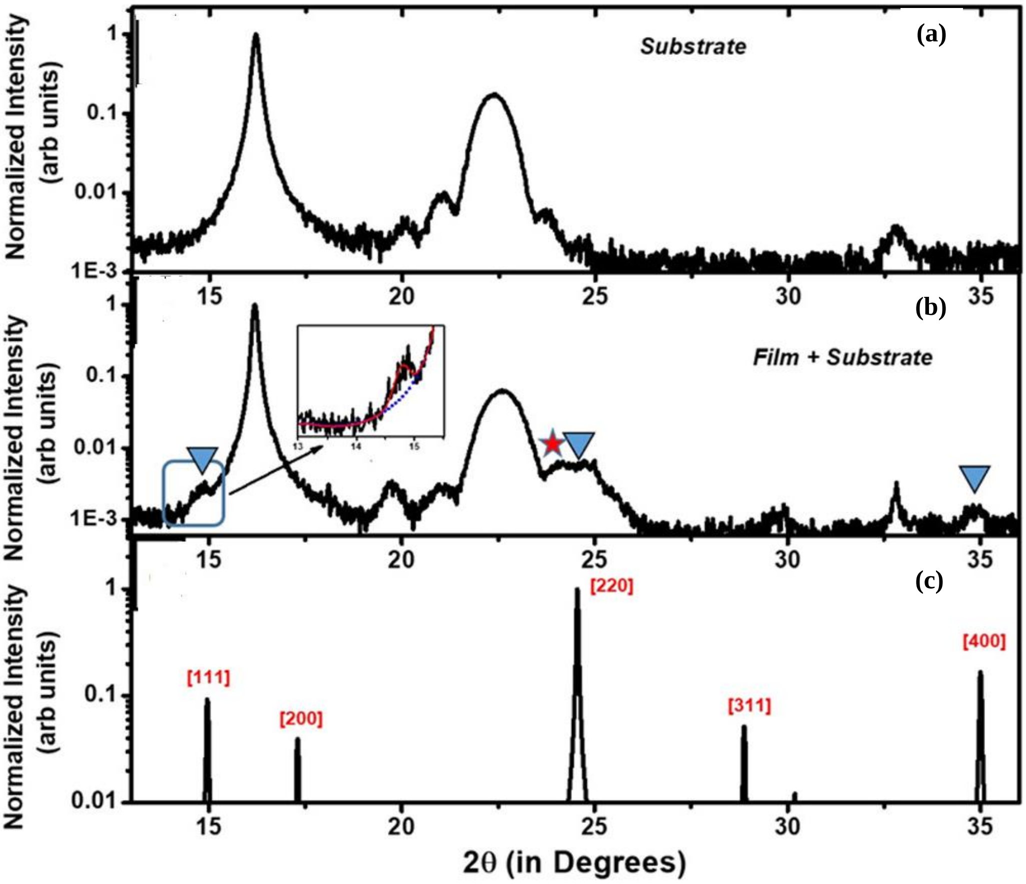

***Figure 4.3:*** *X-ray diffraction data recorded with 0.884 Å X-ray for (a) Pt/Ta/Si [111] substrate and (b) $Co_2FeSn$ film grown on Pt/Ta/ Si [111] substrate. The ∇ symbol indicates film related diffraction peak. The ⋆ symbol indicates substrate related diffraction peak adjacent to [220] diffraction peak of $Co_2FeSn$. The inset shows enlarged view of $Co_2FeSn$ related [111] diffraction peak that clearly appears on top of an extended background from the adjacent substrate related peak. The dotted line in the inset shows a representative simulated background obtained by interpolating with a spline fit. The solid line is a guide to the eye. (c) XRD simulation of $L2_1$ ordered $Co_2FeSn$ films under 0.884 Å wavelength X-ray photon excitation.*

### 4.3.2 Magnetization measurements

Figure 4.4 shows the M-H curve of the deposited film at 5K and 300K. The film shows a strong ferromagnetic with high saturation magnetization value. The coercive field is 400 Oe and 50 Oe at 5K and 300K, respectively.

Figure 4.5 shows magnetization versus temperature plot for ZFC and FC measurements. The data shows a clear branching between ZFC and FC traces at 350K.

Such branching is well known to occur when the sample is magnetically ordered. This clearly indicates that the samples have magnetic ordering temperature greater than 350K. The ordering temperature has also improved in the case of single crystalline substrate compared to the polycrystalline copper substrate. This was also expected because of higher Kerr rotation in the sample grown on single crystalline substrate.

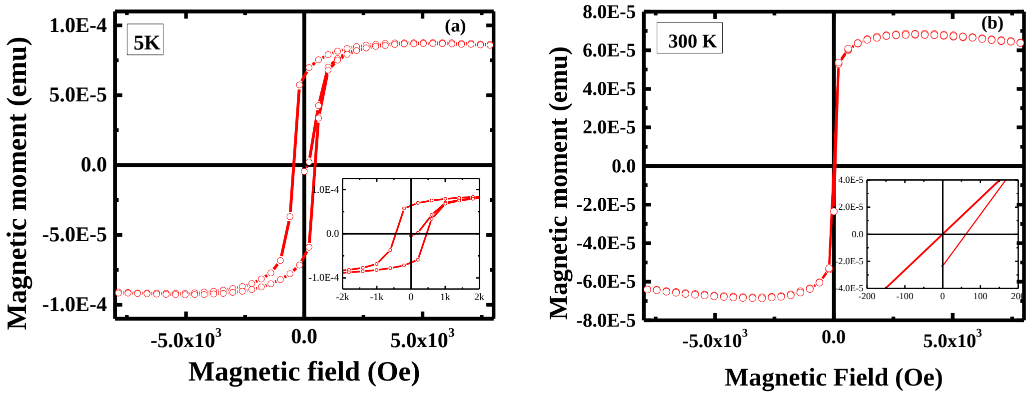

***Figure 4.4:*** *M-H curve of the deposited $Co_2FeSn$ film at (a) 5K, (b) 300K.*

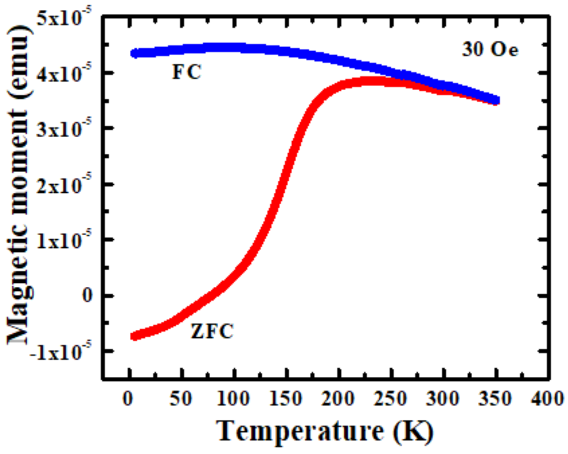

***Figure 4.5:*** *Magnetization vs temperature plot recorded using ZFC (shown red color) and FC (shown by blue solid line) protocol. The data is recorded at 30 Oe magnetic field.*

### 4.3.3 Magneto-optical Kerr effect (MOKE)

Figure 4.6-(a-d), shows MOKE hysteresis measurements on the CFSn film. With the variation of the direction of application of the magnetic field along the surface plane of the film, the shape of hysteresis loop is found to change reversibly from square to oblique and back. This change is related to the presence of a hard and an easy magnetization axis

due to strong magnetic anisotropy. The hysteresis loop is square when parallel to the easy axis (EA). The dependence of the coercivity on the angle between applied field and the easy axis shows a twofold symmetry [Fig. 4.7]. The maximum and minimum values of the coercivity are respectively around 14 Oe and 7 Oe. Such a two-fold symmetry of the hysteresis is indicative of presence of a strong uniaxial magnetic anisotropy. In an ordered cubic crystalline Heusler alloy structure a biaxial anisotropy is expected [13,16]. However uniaxial anisotropy has been previously observed in crystalline Co-based Heusler films that is attributed to weak $L2_1$ ordering [17]. This indicates that the observed change in magnetic hysteresis loop and the associated uniaxial anisotropy is related to the growth quality of the electrochemically grown film having weak $L2_1$ order.

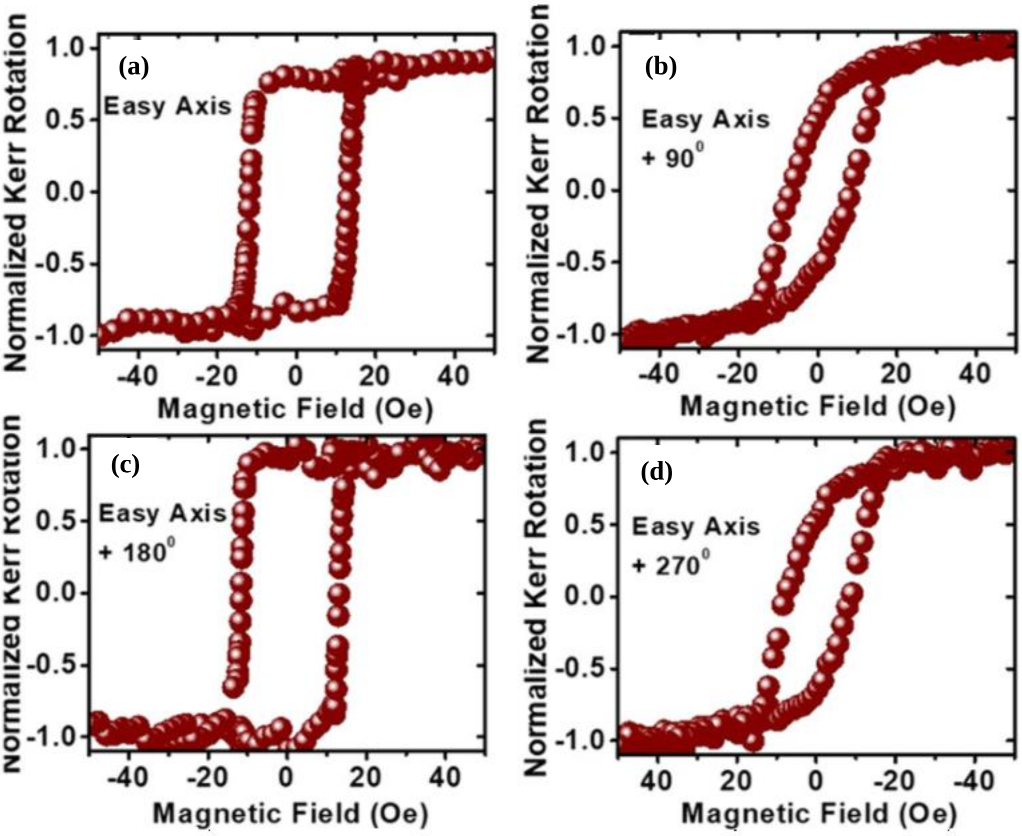

*__Figure 4.6:__ (a-d) shows MOKE hysteresis loop recorded for different directions of applied magnetic field with respect to the easy axis (EA) of magnetization. The magnetic field direction is (a) parallel to the EA (b) 90° with respect to EA (c) 180° with respect to EA and (d) 270° with respect to EA.*

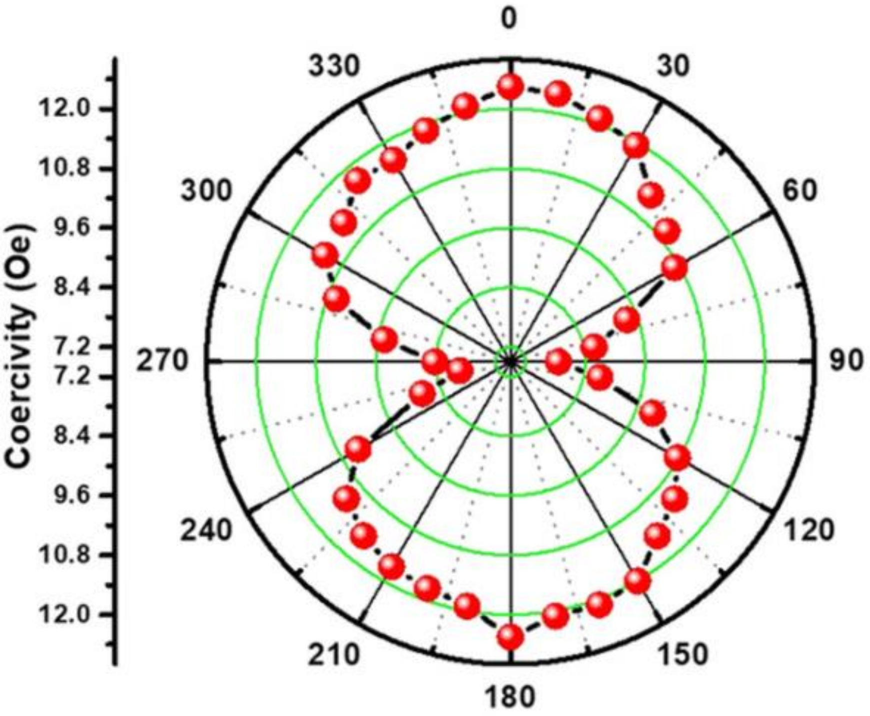

***Figure 4.7:*** *Polar plot of coercivity vs angle of applied magnetic field with respect to the EA.*

MOKE microscopy images (Fig. 4.8) of the magnetic domains measured along the easy axis, reveal the magnetization reversal process of the CFSn films, from a state magnetically saturated along one direction (Fig. 4.8(I)) to the opposite (Fig. 4(VII)). During the magnetization reversal process, only two types of magnetic domain contrast that of black and light grey are observed in the MOKE images. This indicates presence of two domains oriented opposite to each other and separated by 180° domain wall. Such a magnetization reversal along easy axis is characteristic of thin films having uniaxial anisotropy [18–20]. The reversal begins on application of a sufficiently strong magnetic field in the opposite direction that initiates nucleation of reversed magnetic domains (Fig. 4(III)). With further increase of the reversed magnetic field, the nuclei begins to grow and form larger domains (Fig. 4(IV)-(VII)). Finally reversed saturated state (Fig. 4(VII)) is achieved by the expansion of the magnetic domains at the saturation magnetic field.

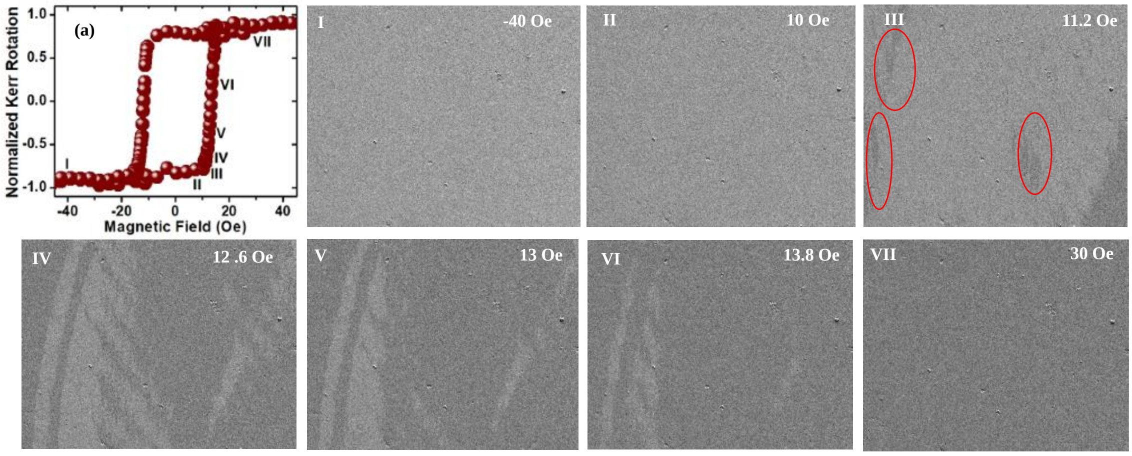

***Figure 4.8:*** *(a) Different regions of magnetization reversal marked between I to VII on the MOKE Hysteresis plot recorded along the easy axis. (I)- (VII) shows the MOKE microscopy domain images for the different regions of the hysteresis plot. (I) The regions correspond to fully saturated magnetization observed evidenced by a single light gray image. (II) Saturation remanence. (III) Magnetization reversal initiation marked by appearance of dark domains indicated by encircled area. (IV) Expansion of reversed magnetization domain. (V) Growth and expansion of reversed magnetization domain. (VI) Predominantly reversed magnetization domain. (VII) Fully saturated reversed magnetization evidenced by a single dark image.*

## 4.4 Conclusion:

In conclusion, we have demonstrated that the electrochemical growth of Co based Heusler alloy film supported on a single crystalline substrate shows improved film quality [21]. The film shows good crystalline property with a finite $L2_1$ ordering. Using Kerr microscopy studies we understand the formation and evolution of the magnetic domains in these electrodeposited films [21]. Through these studies we develop an understanding of surface magnetization reversal in the electrodeposited films [21]. The static MOKE measurements also reveal that electrodeposited samples possess strong uniaxial magneto-crystalline anisotropy which is very important for device application point of view. Furthermore angle dependent MOKE measurements reveal a two-fold symmetry in the electrodeposited CFSn films that is typical of highly ordered crystalline Heusler alloy phase [21]. The results presented here opens up opportunity to further explore electrochemically grown intermetallic alloy films on crystalline substrates, for realizing possible magneto optical and spintronics applications.

## 4.5 References:

[1] T. Graf, C. Felser, and S. S. P. Parkin, Prog. Solid State Chem. **39**, 1 (2011).

[2] G. Qin, W. Ren, and D. J. Singh, Phys. Rev. B **101**, 14427 (2020).

[3] J. Chico, S. Keshavarz, Y. Kvashnin, M. Pereiro, I. Di Marco, C. Etz, O. Eriksson, A. Bergman, and L. Bergqvist, Phys. Rev. B **93**, 214439 (2016).

[4] A. Kumar, F. Pan, S. Husain, S. Akansel, R. Brucas, L. Bergqvist, S. Chaudhary, and P. Svedlindh, Phys. Rev. B **96**, 224425 (2017).

[5] C. Sterwerf, M. Meinert, J. Schmalhorst, and G. Reiss, IEEE Trans. Magn. **49**, 4386 (2013).

[6] S. Ikeda, K. Miura, H. Yamamoto, K. Mizunuma, H. D. Gan, M. Endo, S. Kanai, J. Hayakawa, F. Matsukura, and H. Ohno, Nat. Mater. **9**, 721 (2010).

[7] Z. Wen, H. Sukegawa, S. Kasai, K. Inomata, and S. Mitani, Phys. Rev. Appl. **2**, 024009 (2014).

[8] N. Watanabe, K. Sano, N. Tasugi, T. Yamaguchi, A. Yamamoto, M. Ueno, R. Sumiyoshi, T. Arakawa, and I. Koiwa, APL Mater. **3**, 041804 (2015).

[9] J. Duan and X. Kou, J. Electrochem. Soc. **160**, D471 (2013).

[10] M. R. Karim, D. Panda, A. Adhikari, P. Sharangi, P. Mandal, S. Ghosh, S. Bedanta, A. Barman, and I. Sarkar, Mater. Today Commun. **25**, 101678 (2020).

[11] J. Noky, J. Gooth, C. Felser, and Y. Sun, Phys. Rev. B **98**, 241106 (2018).

[12] M. A. Tanaka, Y. Ishikawa, Y. Wada, S. Hori, A. Murata, S. Horii, Y. Yamanishi, K. Mibu, K. Kondou, T. Ono, and S. Kasai, J. Appl. Phys. **111**, (2012).

[13] S. Trudel, G. Wolf, J. Hamrle, B. Hillebrands, P. Klaer, M. Kallmayer, H.-J. Elmers, H. Sukegawa, W. Wang, and K. Inomata, Phys. Rev. B **83**, 104412 (2011).

[14] S. Emori and G. S. D. Beach, J. Appl. Phys. **110**, 33919 (2011).

[15] W. Kraus and G. Nolze, J. Appl. Crystallogr. **29**, 301 (1996).

[16] M. Belmeguenai, H. Tuzcuoglu, M. S. Gabor, T. Petrisor, C. Tiusan, F. Zighem, S. M. Chérif, and P. Moch, J. Appl. Phys. **115**, 43918 (2014).

[17] S. Yamada, K. Hamaya, K. Yamamoto, T. Murakami, K. Mibu, and M. Miyao,

Appl. Phys. Lett. **96**, 82511 (2010).

[18] S. Chikazumi and C. D. Graham, *Physics of Ferromagnetism 2e* (Oxford University Press on Demand, 2009).

[19] S. Mallik, A. S. Mohd, A. Koutsioubas, S. Mattauch, B. Satpati, T. Brückel, and S. Bedanta, Nanotechnology **30**, 435705 (2019).

[20] S. Mallick, S. Bedanta, T. Seki, and K. Takanashi, J. Appl. Phys. **116**, 133904 (2014).

[21] M. R. Karim, A Adhikari, S N Panda, P. Sharangi, S. Kayal, G. Manna, P. S. Anil Kumar, S. Bedanta, A. Barman, and I. Sarkar, J. Phys. Chem. C **125**, 10483-10492 (2021).

# Chapter 5

# Strain and crystallite size controlled ordering of Heusler nanoparticles having high heating rate for magneto-thermal application

Magnetic Heusler alloy has several advantageous properties that when prepared in the form of nanoparticles can render them as an important class of material for magneto-thermal applications. However, the investigation of heat dissipation due to application of oscillating magnetic field has been lacking in Heusler alloy nanoparticles. Here we present a detailed understanding of the interplay of the growth parameters that can be used to efficiently control crystallinity, disorder, and magnetic transition temperature of Heusler nanoparticles supported on silica matrix. It is found that optimization of the product of strain with crystallite size leads to higher B2 ordering and higher magnetic transition temperature. Furthermore, using magnetic hyperthermia measurements we evaluate the heat generation capability of the nanoparticles under an oscillating magnetic field. A high specific absorption rate of the order of 112 W/g is obtained under moderate magnetic field.

M. R. Karim, et.al. Nanotechnology **33**, 235701 (2022)

## 5.1 Introduction:

Magnetic Heusler alloys are an exciting class of intermetallic materials that are known to exhibit high spin polarization, high curie temperature and low magnetic damping parameter [1–3]. These unique characteristics are ideal for above room temperature magneto-thermal applications. The heat generation in magnetic systems is related to the change in their energy density in presence of time varying magnetic field. When the magnetic field varies in time, the magnetization of the system lags behind the variation. This leads to a magnetic work done that gets dissipated as heat via spin-phonon coupling [4,5]. Magnetic nanoparticles provide an excellent opportunity for heat generation under oscillatory/alternating magnetic field that has applications ranging from spintronics to hyperthermia for cancer treatment and magnetically triggered drug delivery [6,7]. Therefore, it is of urgent interest to develop Heusler alloy nanoparticles that are capable of generating heat at a high rate in presence of alternating magnetic field.

Heulser alloys are mostly intermetallic ternary alloys. The ternary HAs appear in two forms, one that of the $X_2YZ$ type, known as full Heulser alloys (FHA) and the second that of XYZ type, known as half Heusler alloy. Ternary FHAs have a cubic crystalline structure with $Fm\bar{3}m$ symmetry that can be interpreted as interpenetrating lattices of different atoms (X,Y,Z) of constituent elements [2]. A fully ordered Terneray FHA is called $L_21$ ordered. However Heusler alloys are prone to postional disorder of atoms. Depending on the extent of intermixing of atomic positions FHAs are classified as fully disordered A2 type and partially ordered B2 type. In A2 type Heulser alloys any of the X,Y and Z elemental atoms can interchange their positions amongst each other. While in B2 type ordered HAs, only partial intermixing of atomic positions of Y and Z atoms occurs. Though HAs have been extensively studied in thin film and bulk forms, but there has been limited success in growth of crystalline magnetic Heusler nanoparticles [8–10]. On the other hand, among the various magnetic nanoparticles explored for magneto-thermal studies, iron oxide has been the most extensively studied system [11,12]. Cobalt-Iron (CoFe) nanoparticle is yet another class of material that has been reported to show promising magneto-thermal effects with high rate of heat release [13–15]. Therefore, it is important to explore development of cobalt-iron based Heulser alloy nanoparticles and evaluate its heat generation capability.

There has been few reports on CoFe based HA nanoparticles that mainly includes growth of $Co_2FeGa$ nanoparticles with mixed crystalline order [9,10,16] and A2 type $Co_2FeAl$ nanoparticles having strong chemical disorder [17]. Recently $Co_2FeGe$ nanoparticles were grown for exploring catalytic applications [8]. CFeSn based FHA is yet another important class of HA that has been studied in thin film form and is predicted to support topological properties [18–22]. Here we report growth of CFSn Heusler nanoparticles supported on silica matrix and explore its heat generation. capability under oscillating magnetic field. By combining X-ray diffraction, Fourier-transform infrared (FTIR) spectroscopy and magnetic measurements, we present an understanding of how an interplay of growth parameters can be used to efficiently control crystallinity, disorder and magnetic transition temperature of Heusler nanoparticles supported on silica matrix. Our results show that by tuning the strain in nanoparticles it is possible to improve the crystalline ordering. It is found that optimization of the product of strain with crystallite size leads to improved magnetic property. Furthermore, we carry out hyperthermia measurements to evaluate the heat dissipation capacity of these nanoparticles under alternating magnetic field. Through these studies, we demonstrate growth of highly ordered B2 type CFSn nanoparticles of ≈ 10nm size embedded in silica matrix that is found to yield a high specific absorption rate of better than 112 W/g of heating under application of alternating magnetic field.

## 5.2 Experimental methods:

CFSn nanoparticles were grown using silica assisted growth by decomposition and reduction method. In this approach the Co, Fe and Sn are first impregnated in mesoporous silica. Figure 5.1 shows the systematic pathways to synthesis the nanoparticles. First, 505.99 mg cobalt sulphate (1.8 mmol, $CoSO_4.7H_2O$, 281.1mg), 278 mg iron sulphate (1 mmol, $FeSO_4.7H_2O$, 278 02mg), 150.32 mg tin sulphate (0.7 mmol, $SnSO_4$, 214.77mg) was mixed in m50mL methanol and stirred well to prepare a precursor solution. Fumed silica (MW- 60.08 g/mol, d:2.3 lb/cu.ft, n20/D 1.46(lit)) was then added to the precursor solution. The solution was further stirred for a homogeneous loading of silica pores. Finally, methanol was evaporated using a rotary evaporator. The obtained powder was then dried in vacuum oven at 60 ºC temperature. The dried powder was grounded to obtain a fine powder. Finally, the fine powder was deoxidized by heating under 20% hydrogen balanced argon atmosphere. The nanoparticles were grown under different conditions by adding different amount (200mg, 400mg, 600 mg, and 800mg) of silica.

The nanoparticles were annealed in different temperature as well and the 900 ℃ temperature was optimized for further analysis.

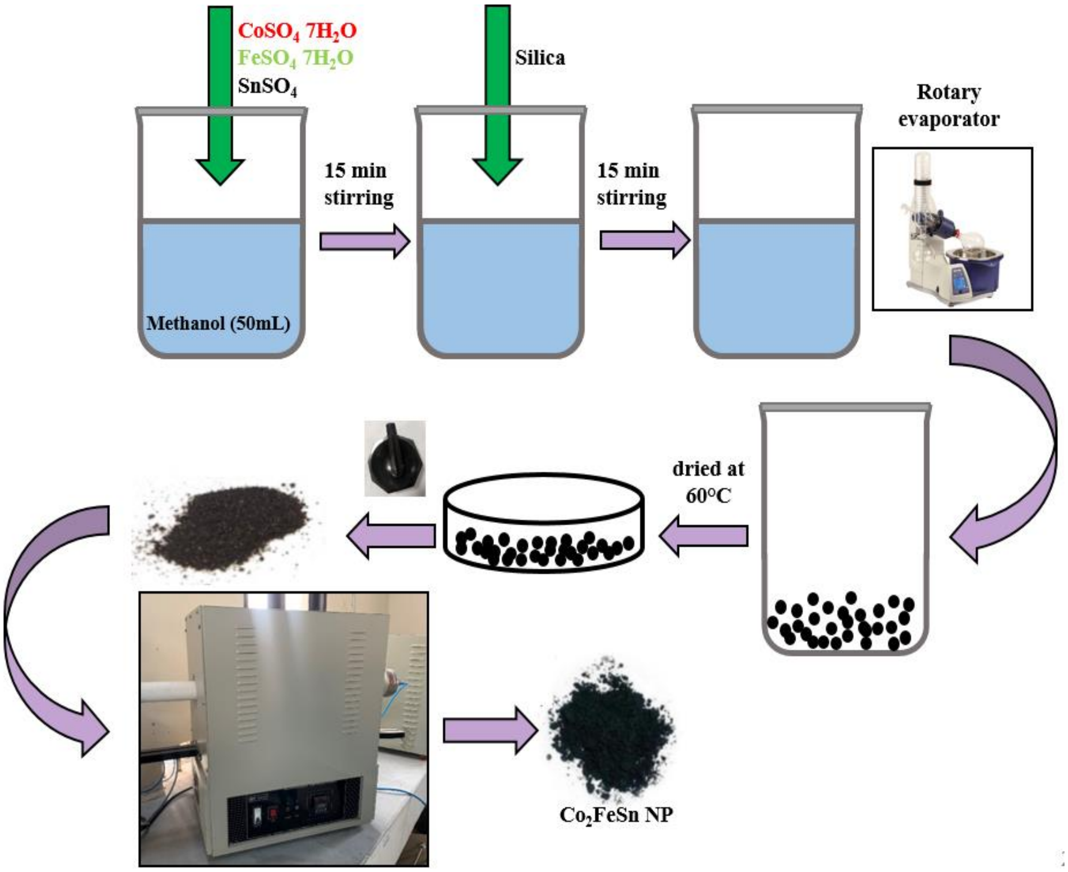

***Figure 5.1:*** *Systematic pathway to synthesis the $Co_2FeSn$ nanoparticles.*

X-ray diffraction (XRD) measurements were carried out using a Bruker D8 Advance diffractometer equipped with Cu Kα X-ray source. High-resolution transmission electron microscopy (HRTEM) images were taken using a JEOL JEM 2100 TEM operating at 200 kV acceleration voltage. FTIR spectra were recorded using ATR-FTIR Bruker Vertex 70 setup. Absorption spectra was obtained by subtracting transmittance from unity. DC magnetization studies were performed using physical property measurements system (Dynacool-PPMS, Quantum Design) equipped with vibrating sample magnetometer. Temperature dependent magnetization data was recorded by employing zero field cooled (ZFC) and field cooled (FC) measurement protocol by cooling the sample in absence and presence of 200 Oe magnetic field, respectively. To evaluate the heat generation efficiency of the Heusler nanoparticles, magnetic hyperthermia efficiency was measured using DM2-DM100 nanomagnetic heating system setup (nB nanoscale Biomagnetics, Zaragoza, Spain). For the hyperthermia measurements an aqueous colloidal solution (1mg/ml) of the nanoparticles was prepared. The data was measured by applying AC magnetic field at 380 kHz while recording the time dependence of the rise of temperature of the magnetic colloidal solution using an integrated fluro-optic thermometer fiber probe. The hyperthermia or heat generation efficiency was measured in terms of the specific absorption rate (SAR). SAR is defined as the power dissipation per unit mass of magnetic nanoparticle (W/g), and is given as [23,24]:

$$SAR = \frac{C}{m}\frac{dT}{dt} \tag{5.1}$$

where, C represents the specific heat of the solution which for these measurements is assumed to be same as that of pure water (C = 4.185 J/g/K). dT/dt is the initial rate of rise of temperature and is obtained from the initial slope of the temperature vs. time graph. m is the weight of the nanoparticles in the solution.

## 5.3 Results and Discussion:

### 5.3.1 Structural analysis and morphology

Figure 5.2 shows XRD data for the nanoparticles grown with different amount of silica in the precursor solution. The data shows three strong peaks around 45°, 65° and 83°, corresponding to [220], [400] and [422] Bragg reflection of CFSn HA [20,22,25,26]. These three reflections are well known to prominently appear in $Co_2FeX$ (X is a sp-element) type of FHAs [8,27–29]. The small peak at around 31° corresponds to [200] Bragg reflection. The [200] reflection is missing in case of disordered A2-type phase but appears when there is either a B2 or $L2_1$ type of ordering [8,28–31]. In case of $L2_1$ type of ordering [111] reflection is additionally observed. Here, the appearance of [200] reflection but absence of [111] in the measured XRD data (Fig. 5.2) is a clear signature of growth of B2 ordered CFSn nanoparticles [8,16,25–27,29].

Interestingly, the intensity of the [200] diffraction peak was found to vary with silica content (insets Fig. 5.2 a-d). The strongest [200] peak appeared in the case of the sample grown in 600 mg silica.

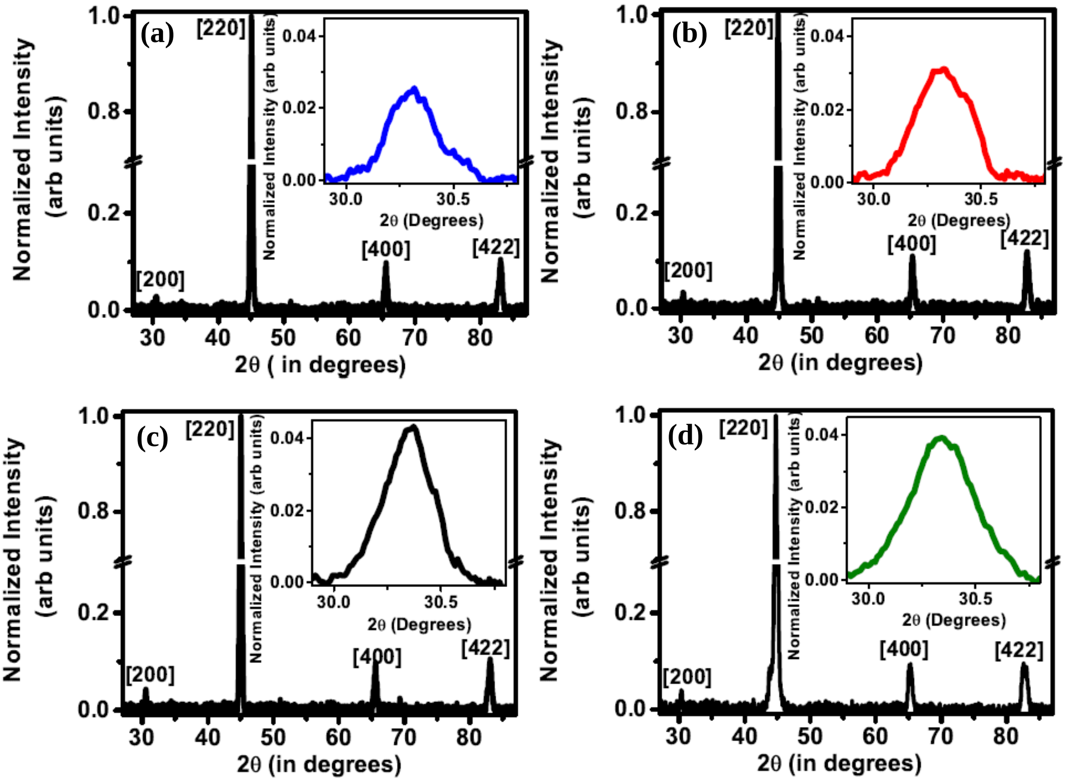

***Figure 5.2:*** *Normalized XRD data for* $Co_2FeSn$ *nanoparticles grown in a precursor solution containing (a) 200 mg (b) 400 mg (c) 600 mg and (d) 800 mg silica. The normalization is carried out with respect to the peak intensity of [220] peak. The inset shows a detailed XRD scan of [200] peak that is normalized to the intensity of [220] peak.*

The relative intensity of the [200] super lattice diffraction peak with respect to the fundamental diffraction peak provides a measure of B2 ordering in Heusler alloys [16,32,33]. The degree of B2 ordering in the nanoparticles were calculated using the formula [32–34],

$$S = \sqrt{\frac{(I_{200})_{exp})*(I_{220})_{order})}{(I_{200})_{order}(I_{220})_{exp}}} \tag{5.2}$$

Where, $(I_{200})_{exp}$ and $(I_{220})_{exp}$ are experimental observed intensities. $(I_{200})_{order}$ and $(I_{220})_{order}$ are theoretically expected intensity for fully ordered system. $(I_{200})_{order} \propto |2* f_{Co} - f_{Fe} - f_{Sn}|^2$ and $(I_{220})_{theo} \propto |2* f_{Co} + f_{Fe} + f_{Sn}|^2$, where $f_{Co}$, $f_{Fe}$ and $f_{Sn}$ are the atomic scattering factors of Co, Fe, and Sn respectively. Using the atomic scattering factors $(I_{200})_{order}/(I_{220})_{order}$ was calculated to be ≈ 0.054 [35].

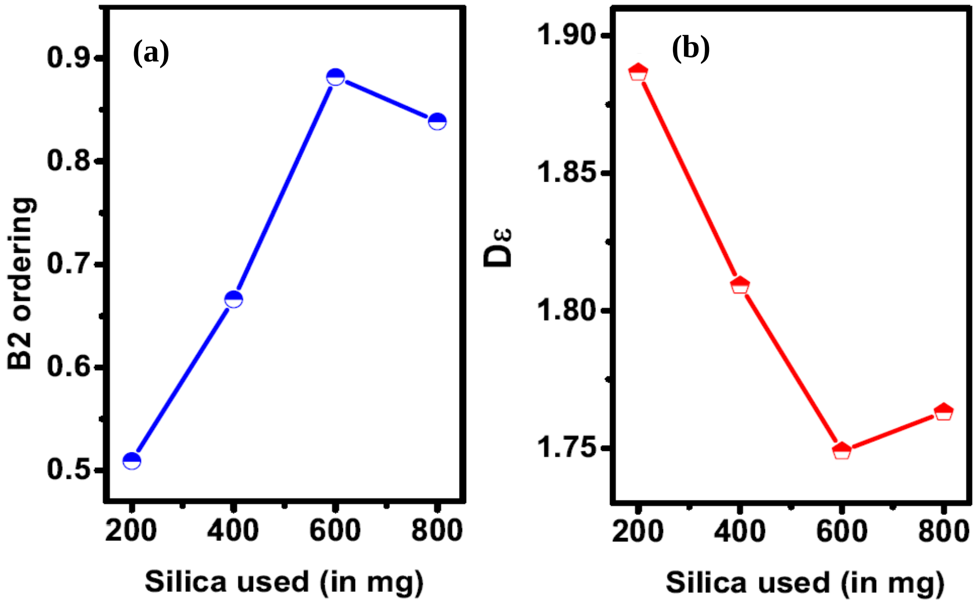

***Figure 5.3:*** *Variation of (a) the degree of B2 ordering and (b) the product D$\epsilon$ value of strain ($\epsilon$) with coherent crystallite size (D), as a function of the amount of silica used during growth of $Co_2FeSn$ nanoparticles.*

The degree of B2 ordering (Fig. 5.3-a) was found to vary non-monotonically with change in the amount of silica used for growth of nanoparticles. This indicated that by changing the silica content it is possible to control the crystalline quality and the degree of atomic positional ordering in the nanoparticles. CFSn nanoparticles that were grown in a precursor solution having 600mg of silica were found to yield the highest degree of B2 ordering. To further explore the optimization of the structural ordering of the nanoparticles as a function of silica content, the coherent crystallite size (D) and strain ($\epsilon$) of the nanoparticles were estimated (Table- 5.1) from the full width at half maxima (FWHM) (β) of the diffraction peaks using the following equation [36],

$$\beta cos\theta = \frac{K\lambda}{D} + 4\varepsilon sin\theta \qquad (5.3)$$

Figure 5.4 (a-d) shows linear plots between βcosθ and 4sinθ. The constant value is the crystallite size of the nanoparticle and slope is the strain in the nanoparticles. Though the values of D and $\epsilon$ were found not to vary in a specific manner with the silica content, but the product of crystallite size with strain of the nanoparticles exhibited (Fig. 5.3-b) an interesting dependence as a function of silica content. The variation of the D$\epsilon$ product is found to have an opposite behavior compared to that of the degree of B2 ordering [Fig.

5.3(b)], wherein with an increase in the Dϵ value, the degree of B2 ordering in the nanoparticles decreased. The Dϵ value was found to be the lowest for the nanoparticles having highest degree of B2 ordering. This clearly indicates that the product minimization of the crystallite size and strain leads to a maximization of structural ordering in the Heusler alloy nanoparticles.

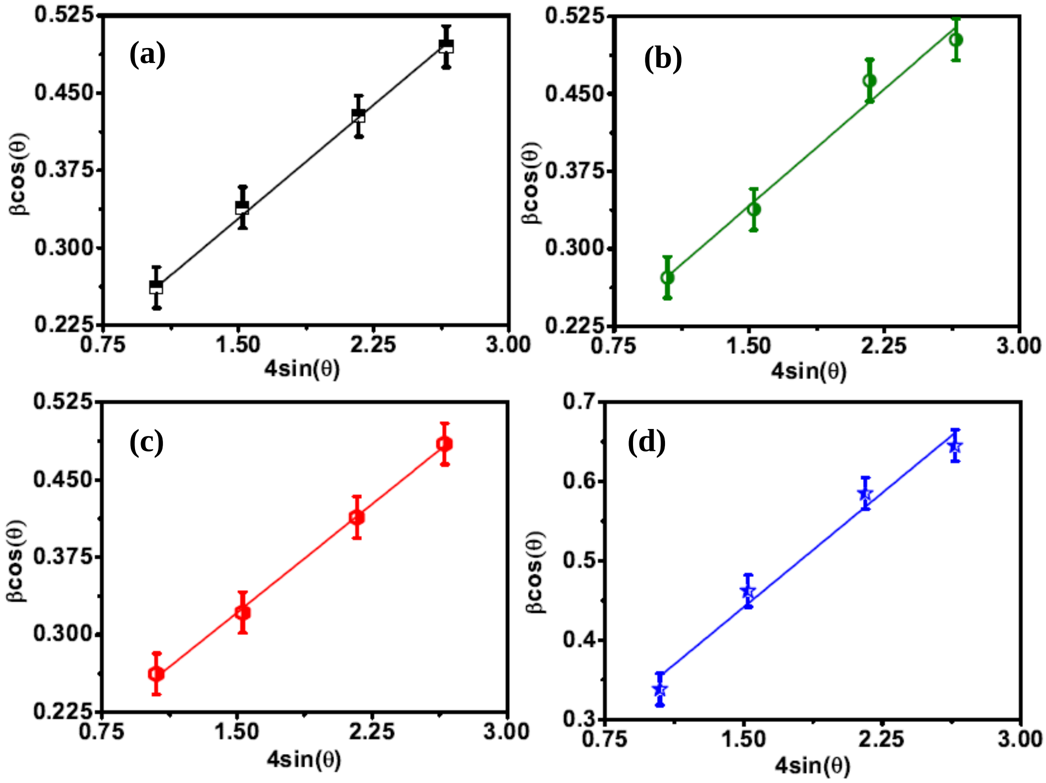

***Figure 5.4:*** *Variation of full width at half maxima (β) of diffraction peak plot with change in angle θ, plotted as βcosθ vs 4sinθ for nanoparticles prepared in (a) 200mg (b) 400 mg (c) 600 mg and (d) 800 mg silica. The solid line is the fit of using the equation* $\beta\cos\theta = K\lambda/D + 4\epsilon\sin\theta$.

***Table 5.1:*** *Calculated D and ϵ obtained for $Co_2FeSn$ nanoparticles grown in different amount of silica.*

| Silica used (mg) | Strain (ε) | Coherent Crystallite size (D) (Å) |
|---|---|---|
| 200 | 0.147 | 12.8 |
| 400 | 0.151 | 12 |
| 600 | 0.140 | 12.5 |

| | | |
|---|---|---|
| 800 | 0.192 | 9.2 |

Figure 5.5 shows HRTEM images of the nanoparticles grown using 200, 400, 600, 800mg of silica. All TEM images show that the particles are roughly spherical in nature. The particle size histograms were plotted using ImageJ software by considering a large number of individual particles from each clusters.

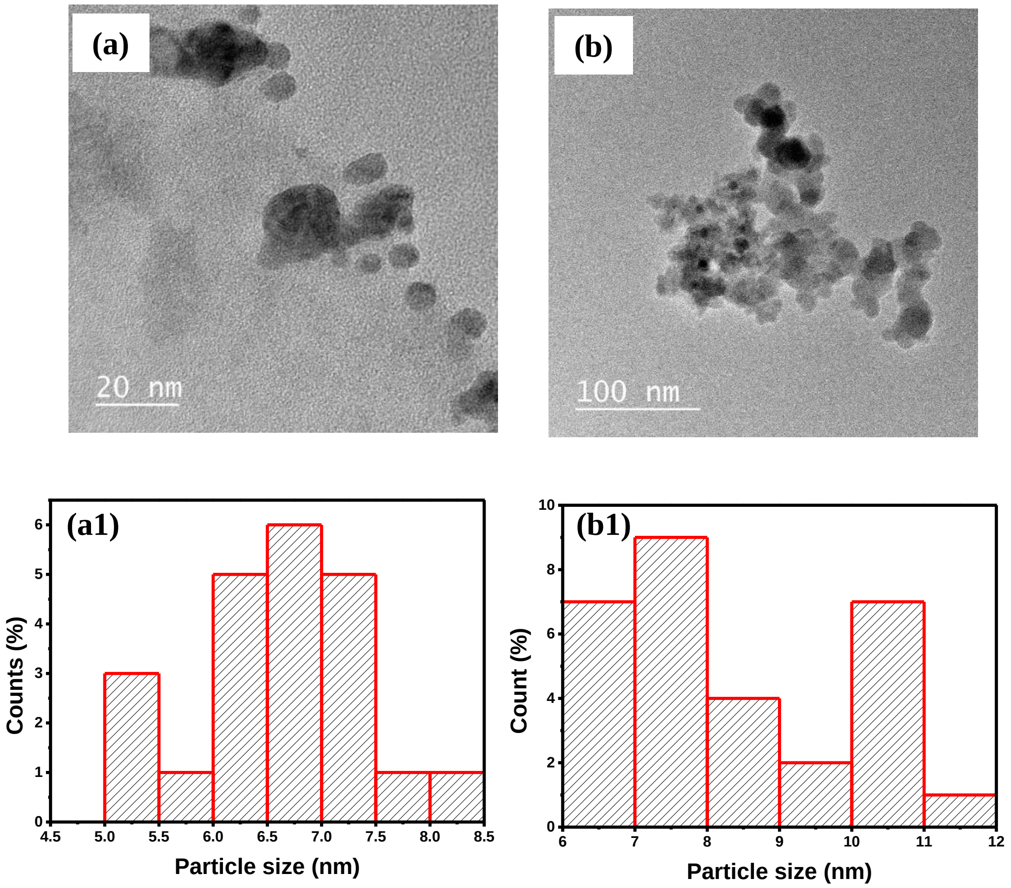

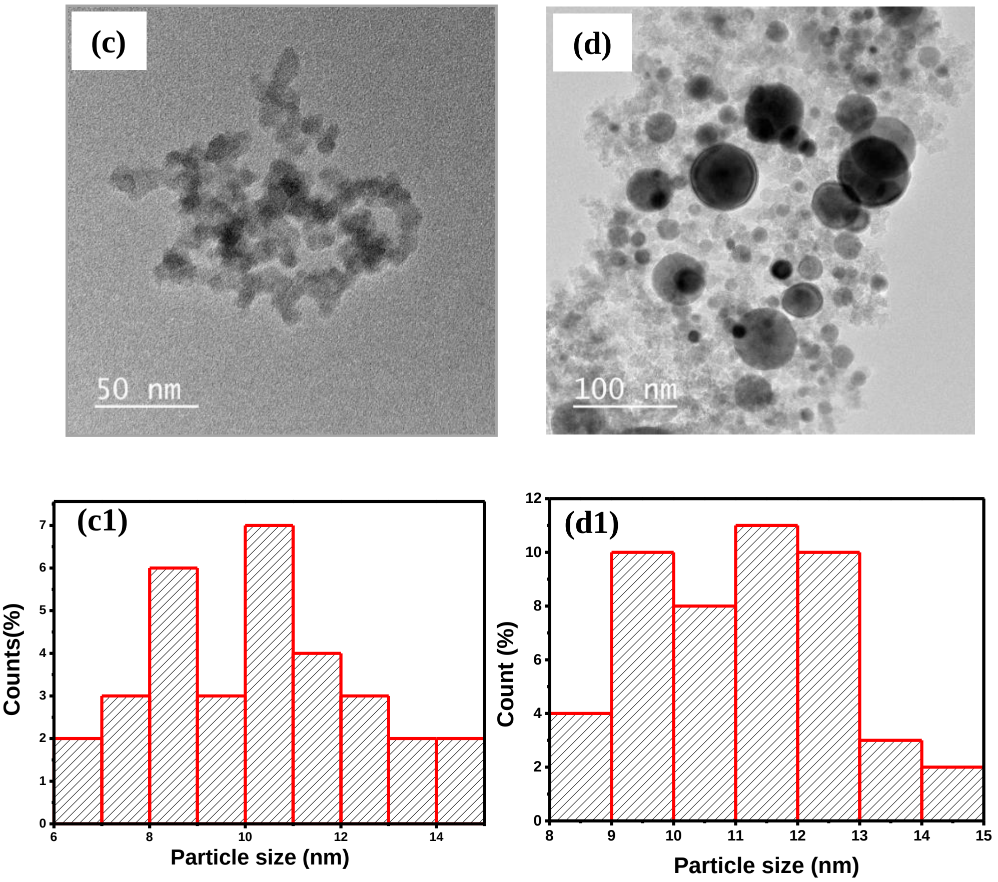

***Figure 5.5:*** *TEM micrographs of different silica loaded nanoparticles (a) cluster of particles with 200 mg silica, (a1) size distribution histogram of particle size, (b) cluster of particles with 400 mg silica, (b1) size distribution histogram of particle size, (c) cluster of particles with 600 mg silica, (c1) size distribution histogram of particle size, (d) cluster of particles with 800 mg silica, (d1) size distribution histogram of particle size.*

From the histogram, it is clearly seen that the particle size and the distribution are increasing with increasing the silica concentration (Fig. 5.5 a-d). The variation of particle size with silica loading is shown in the figure 5.6-a. We observe an increase in the particle size from 6.5 nm (200mg silica) to 11.2 nm for 800 mg silica. As the 600 mg silica loaded sample has highest B2 ordering so we did a detail study of TEM for this sample. The single particle image (600 mg silica) show clear lattice fringes indicating high crystalline quality (Fig. 5.6-b). To check the crystallinity of the nanoparticles selected area electron diffraction (SAED) (Fig. 5.6-d) was done. The SAED pattern is consistent with XRD results which confirm that nanoparticles have well defined crystalline phase. The inverse fast Fourier transform (IFFT) (Fig. 5.6-c) confirms the d-spacing of 0.21 nm which correspond to the [220] plane of CFSn nanoparticles.

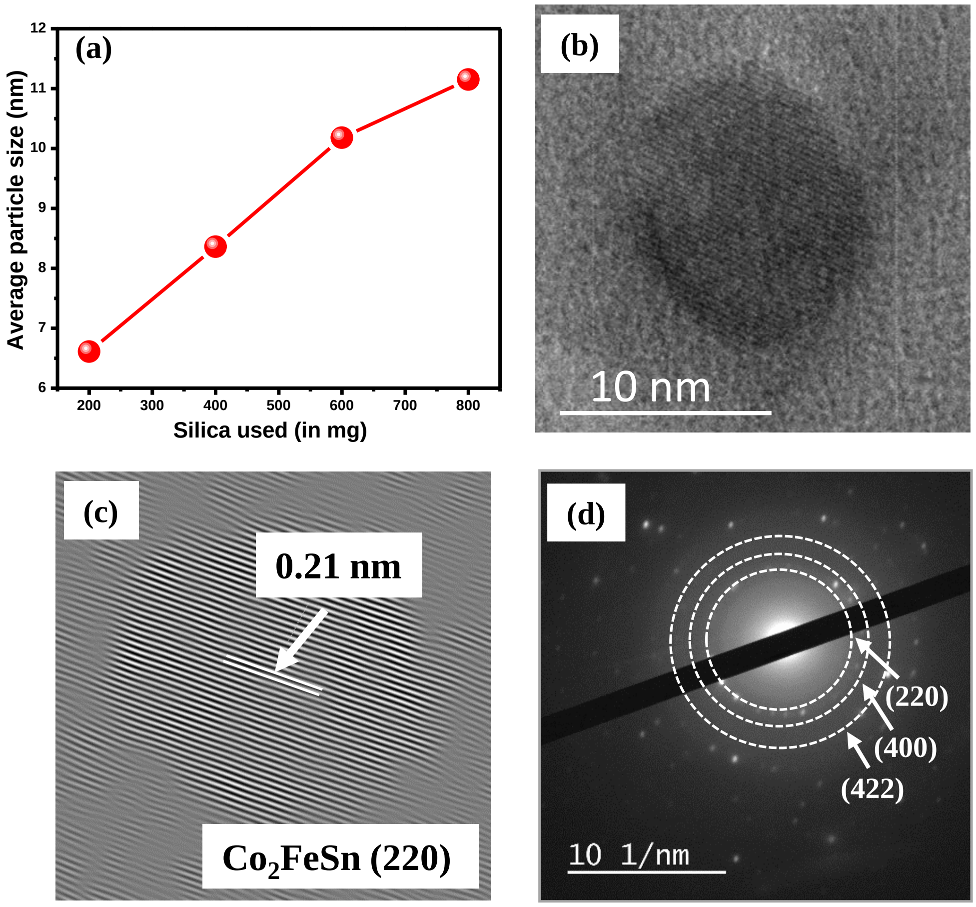

***Figure 5.6:*** *(a) Particle size with different silica concentration, (b) HR-TEM image, (c) inverse-FFT pattern of selected area from, (d) the SAED pattern, of 600 mg silica loaded sample.*

To check the chemical composition, the EDAX was done after drop casting the 600 mg silica loaded sample on copper plate. CFSn nanoparticles showed Co: Fe: Sn elements in the ratio of 2(±0.01):1(±0.01):1(±0.01) as shown in the figure 5.7. There is no other impurity in the sample.

### 5.3.2 Fourier transform infrared spectroscopy

FTIR measurements were carried out to further understand the interaction of the silica with the nanoparticles. The FTIR measurements (Fig. 5.8 a-c) show presence of three well known absorption peaks of silica centered around ≈ 1080 $cm^{-1}$, 800 $cm^{-1}$ and 456 $cm^{-1}$ that respectively corresponds to antisymmetric stretching (A), symmetric stretching (S) and rocking vibrations (R) of Si-O-Si bridges in the silica network [37–40].

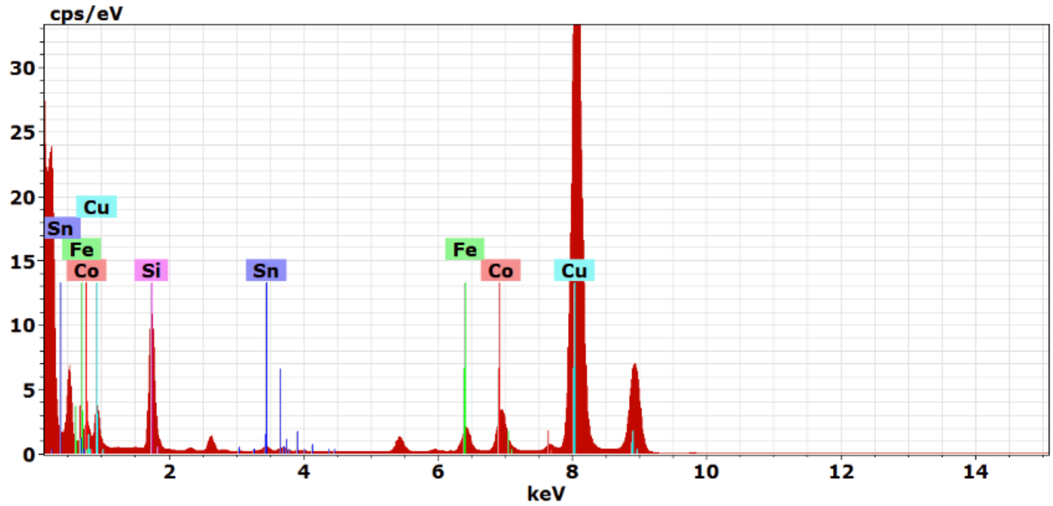

***Figure 5.7:*** *EDAX spectra of $Co_2FeSn$ nanoparticles prepared in 600 mg silica.*

Figure 5.8 (d-e) presents the relative peak intensity ratio of R-peak (around 456 $cm^{-1}$) and S-peak (around 800 $cm^{-1}$) normalized by intensity of the A-peak at 1080 $cm^{-1}$. Interestingly, the R/A peak intensity ratio (Fig. 5.8-d) shows significant variation with the amount of silica used for growth of nanoparticles, though the S/A peak ratio (Fig. 5.8-e) remains mostly unchanged with change in the amount of silica used. The R/A peak ratio (Fig 5.8-d) is highest for nanoparticles prepared in 600mg silica compared to that of the nanoparticles grown in presence of 400mg and 800mg silica. This indicates that the rocking vibrations are less constrained in nanoparticles prepared using 600mg silica that as discussed earlier have the highest degree of B2 ordering. This indicates a lower constraint on rocking vibrations of silica in the better structurally ordered Heusler nanoparticles compared to that of less ordered ones. This is indicative of weaker surface interaction of silica with the Heusler nanoparticles in case of better ordered system that allows greater degree of freedom for different possible vibrations. This weaker surface interaction can be a possible cause for lowering of the product value of strain with crystallite size ($D\epsilon$) for the nanoparticles having higher B2 ordering, as observed from the diffraction results.

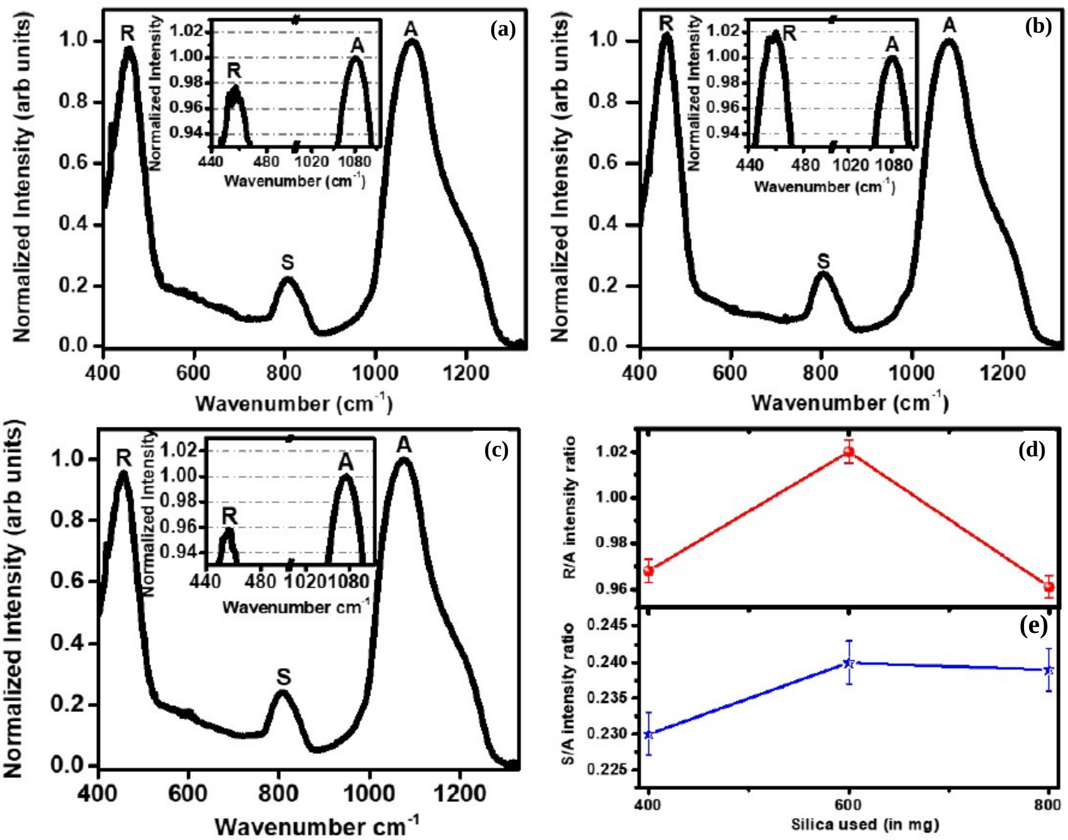

***Figure 5.8:*** *Normalized FTIR spectra of $Co_2FeSn$ nanoparticles prepared in (a) 400 mg (b) 600 mg and (c) 800 mg silica. Normalization is done with respect to the intensity of A-peak corresponding to antisymmetric stretching vibration. The inset shows the zoomed section for comparison of intensities of R-peak and A-peak. Variation of (d) R/A peak intensity ratio and (e) S/A peak intensity ratio as a function of the amount of silica used for the growth of nanoparticles.*

### 5.3.3 DC Magnetic studies

DC magnetization measurements were carried out to study the effect of structural ordering on the magnetic property of the nanoparticles. Figure 5.9 (a-d) shows ZFC-FC plot of the nanoparticles grown in presence of 200mg, 400mg, 600mg and 800 mg silica. The ZFC-FC plot for all the nanoparticles show clear branching above room temperature which is a signature of magnetic ordering in these nanoparticles. The branching temperature varied with the nanoparticles having different degree of B2 ordering. The magnetic ordering temperature is highest for nanoparticles having the highest degree of B2 ordering grown in the presence of 600mg silica and is found to be 380K. The magnetic ordering temperature of the nanoparticles grown in 200mg silica, 400 mg silica and 800 mg silica are around 340K, 350K and 360K respectively. This is consistent with the observation of highest degree of B2 ordering in nanoparticles grown in 600 mg silica and

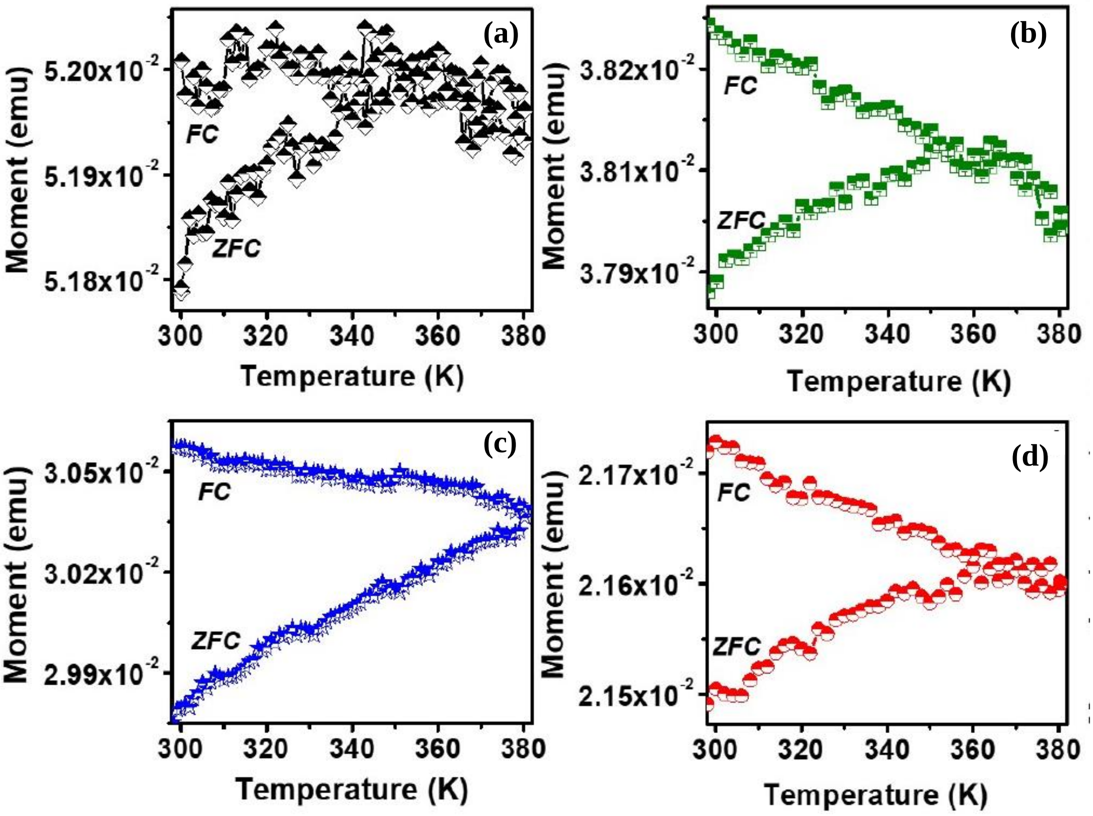

***Figure 5.9:*** *ZFC-FC plot of magnetization vs temperature for nanoparticles prepared in (a) 200 mg (b) 400 mg (c) 600 mg and (d) 800mg silica.*

lowest degree of B2 ordering in 200mg. Clearly the magnetic ordering temperature is found to improve with the degree of B2 ordering (Fig. 5.10-a). The magnetization measurements as function of the magnetic field (Fig. 5.10-b) clearly demonstrates ferromagnetic nature in the nanoparticles marked by presence of hysteresis.

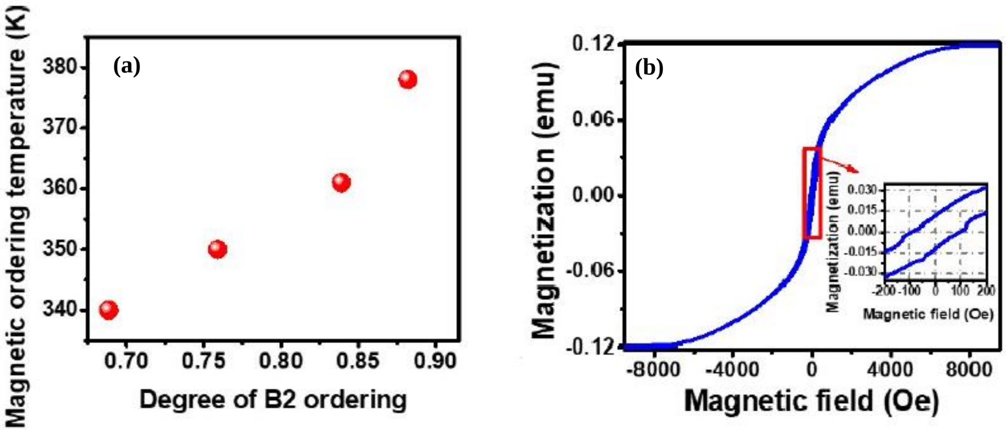

***Figure 5.10:*** *(a) Degree of B2 ordering vs magnetic ordering temperature plot. (b) Magnetization versus magnetic field plot for nanoparticles having highest degree of B2 ordering prepared in 600 mg silica.*

The corresponding coercive field for the nanoparticles having highest degree of B2 ordering is 200 Oe (inset Fig. 5.10-b).

### 5.3.4 The hyperthermia measurements

Magnetic hyperthermia measurements were performed to evaluate the heat generation capability of the B2 ordered CFSn nanoparticles by applying alternating magnetic field. The measurements were performed on an aqueous colloidal solution (1mg/ml) containing the nanoparticles. Figure 5.11 shows results of hyperthermia measurements for colloidal solutions containing HA nanoparticles grown in different amount of silica. The measurements clearly demonstrate the heat release by the nanoparticles that consequently lead to an increase in the temperature of the colloidal solution. The rise in temperature (Fig. 5.11) was found to be maximum in the colloidal solution containing nanoparticles prepared in 600mg silica that corresponded to the highest B2 ordered samples.

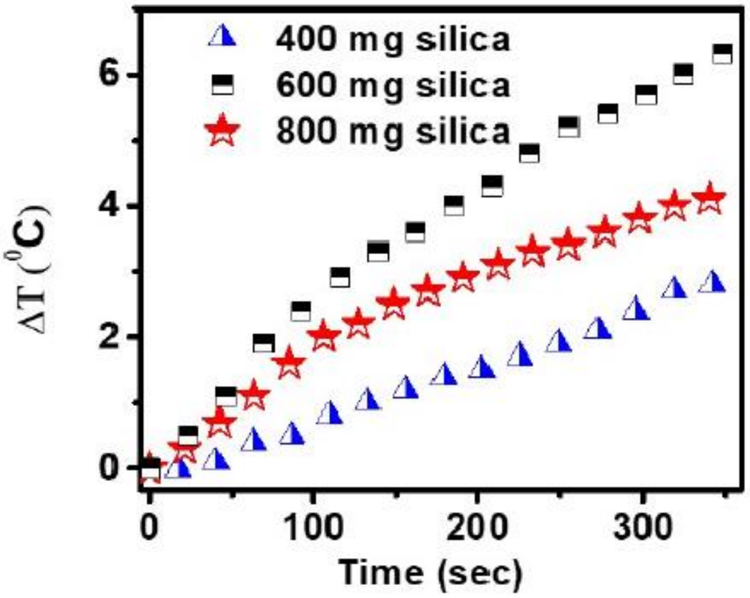

***Figure 5.11:*** *Hyperthermia measurements taken at 380 Oe and 380 KHz on solution containing $Co_2FeSn$ nanoparticles grown in 400mg, 600mg and 800mg silica.*

This indicated improvement in heat generation capability of the Heusler nanoparticles with improvement in their structural ordering. A large specific absorption rate (SAR) value of about 112 W/g was obtained for the highest structurally ordered samples under the application of 380 Oe AC magnetic field at 380 kHz. Furthermore, hyperthermia measurements were carried out for varying magnetic field strength (Fig. 5.12-a). The

SAR value shows a quadratic dependence on the strength of the applied magnetic field (Fig. 5.12-b).

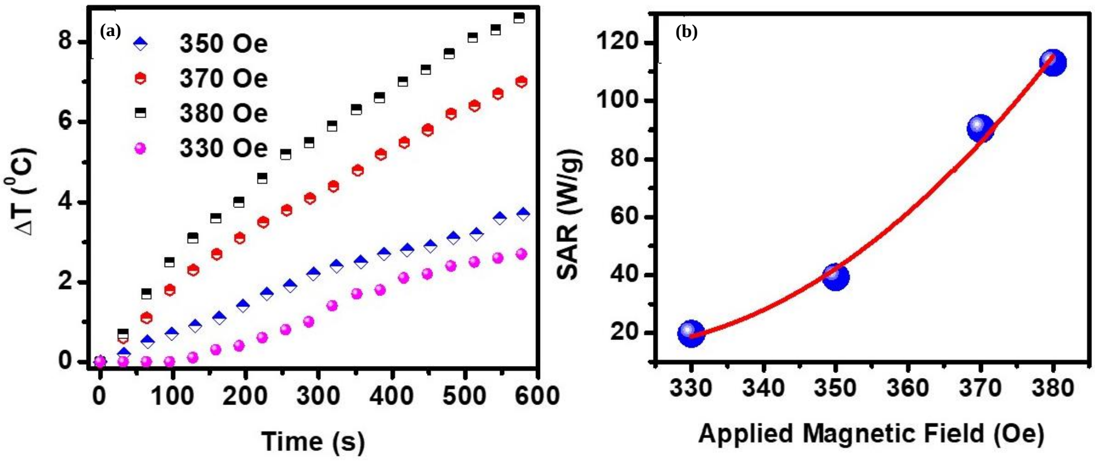

***Figure 5.12:*** *(a) Hyperthermia measurements plot of rise in temperature ΔT versus time taken at varying alternating magnetic field strength. The measurements are performed at 380 kHz on* $Co_2FeSn$ *nanoparticles grown in 600mg silica that has highest degree of B2 ordering. (b) SAR value vs magnetic field strength plot. The solid line is guide to the eye that shows a quadratic dependence on magnetic field strength*.

Similar magnetic field dependence of the SAR has been earlier observed in the hyperthermia studies of magnetic iron oxide nanoparticles and is attributed to the fact that magnetic power dissipation is proportional to the square of the magnetic field strength [41–45].

## 5.4 Conclusion:

To summarize the results presented here demonstrates a novel possibility of growth of Heusler alloy nanoparticles having high rate of heat dissipation [46]. The results present an important finding of a unique parameter related to the product of strain and coherent crystallite size of the nanoparticles, which when optimized can lead to the enhancement of crystalline and structural ordering in Heusler nanoparticles [46]. This improvement of the structural ordering of the nanoparticles is found to lead to higher magnetic transition temperatures. This work provides a new understanding and opportunity for the development of Heusler alloy nanoparticles capable of heat generation that will stimulate further studies on finding magneto-thermal applications using this less explored class of materials.

## 5.5 References:

[1] S. Kurdi, M. Ghidini, M. Ghidini, M. Ghidini, G. Divitini, B. Nair, A. Kursumovic, P. Tiberto, S. S. Dhesi, and Z. H. Barber, Nanoscale Adv. **2**, 2602 (2020).

[2] T. Graf, C. Felser, and S. S. P. Parkin, Prog. Solid State Chem. **39**, 1 (2011).

[3] K. Nawa and Y. Miura, RSC Adv. **9**, 30462 (2019).

[4] C. Muñoz-Menendez, D. Serantes, O. Chubykalo-Fesenko, S. Ruta, O. Hovorka, P. Nieves, K. L. Livesey, D. Baldomir, and R. Chantrell, Phys. Rev. B **102**, 1 (2020).

[5] J. Leliaert, J. Ortega-Julia, and D. Ortega, Nanoscale **13**, 14734 (2021).

[6] J. Kim, J. E. Lee, S. H. Lee, J. H. Yu, J. H. Lee, T. G. Park, and T. Hyeon, Adv. Mater. **20**, 478 (2008).

[7] H. Belkahla, G. Herlem, F. Picaud, T. Gharbi, M. Hémadi, S. Ammar, and O. Micheau, Nanoscale **9**, 5755 (2017).

[8] T. Kojima, Y. Nakaya, H. Ham, S. Kameoka, and S. Furukawa, RSC Adv. **11**, 18074 (2021).

[9] C. H. Wang, Y. Z. Guo, F. Casper, B. Balke, G. H. Fecher, C. Felser, and Y. Hwu, Appl. Phys. Lett. **97**, 103106 (2010).

[10] C. Wang, A. A. Levin, S. Fabbrici, L. Nasi, J. Karel, J. Qian, C. E. V. Barbosa, S. Ouardi, F. Albertini, and W. Schnelle, J. Mater. Chem. C **4**, 7241 (2016).

[11] J.-H. Lee, B. Kim, Y. Kim, and S.-K. Kim, Sci. Rep. **11**, 4969 (2021).

[12] H. Chen, D. Billington, E. Riordan, J. Blomgren, S. R. Giblin, C. Johansson, and S. A. Majetich, Appl. Phys. Lett. **117**, 73702 (2020).

[13] J. Marbaix, N. Mille, L.-M. Lacroix, J. M. Asensio, P.-F. Fazzini, K. Soulantica, J. Carrey, and B. Chaudret, ACS Appl. Nano Mater. **3**, 3767 (2020).

[14] Ö. Çelik and T. Fırat, J. Magn. Magn. Mater. **456**, 11 (2018).

[15] L. M. Lacroix, R. B. Malaki, J. Carrey, S. Lachaize, and M. Respaud, J. Appl. Phys. **2009**, 105 (2009).

[16] L. Basit, C. Wang, C. A. Jenkins, B. Balke, V. Ksenofontov, G. H. Fecher, C. Felser, E. Mugnaioli, U. Kolb, S. A. Nepijko, G. Schönhense, and M. Klimenkov, J. Phys. D. Appl. Phys. **42**, 84018 (2009).

[17] A. Ahmad, S. Mitra, S. K. Srivastava, and A. K. Das, J. Magn. Magn. Mater. **474**, 599 (2019).

[18] M. R. Karim, D. Panda, A. Adhikari, P. Sharangi, P. Mandal, S. Ghosh, S. Bedanta, A. Barman, and I. Sarkar, Mater. Today Commun. **25**, 101678 (2020).

[19] M. R. Karim, A. Adhikari, S. N. Panda, P. Sharangi, S. Kayal, G. Manna, P. S. A. Kumar, S. Bedanta, A. Barman, and I. Sarkar, J. Phys. Chem. C **125**, 10483 (2021).

[20] M. A. Tanaka, Y. Ishikawa, Y. Wada, S. Hori, A. Murata, S. Horii, Y. Yamanishi, K. Mibu, K. Kondou, T. Ono, and S. Kasai, J. Appl. Phys. **111**, 53902 (2012).

[21] J. Noky, J. Gooth, C. Felser, and Y. Sun, Phys. Rev. B **98**, 241106 (2018).

[22] N. Watanabe, K. Sano, N. Tasugi, T. Yamaguchi, A. Yamamoto, M. Ueno, R. Sumiyoshi, T. Arakawa, and I. Koiwa, APL Mater. **3**, 41804 (2015).

[23] S. Moise, J. M. Byrne, A. J. El Haj, and N. D. Telling, Nanoscale **10**, 20519 (2018).

[24] R. Gupta and D. Sharma, Nanoscale Adv. **3**, 3663 (2021).

[25] H. Lu, Y. Liu, and X. Kou, J. Electrochem. Soc. **165**, D813 (2018).

[26] L. Galdun, P. Szabo, V. Vega, E. D. Barriga-Castro, R. Mendoza-Reséndez, C. Luna, J. Kovac, O. Milkovic, R. Varga, and V. M. Prida, ACS Appl. Nano Mater. **3**, 7438 (2020).

[27] A. Ahmad, S. Mitra, S. K. Srivastava, and A. K. Das, J. Magn. Magn. Mater. **474**, 599 (2019).

[28] R. Mahat, S. KC, U. Karki, J. Y. Law, V. Franco, I. Galanakis, A. Gupta, and P. LeClair, Phys. Rev. B **104**, 14430 (2021).

[29] M. Zhang, E. Brück, F. R. de Boer, Z. Li, and G. Wu, J. Phys. D. Appl. Phys. **37**, 2049 (2004).

[30] J. H. Du, Y. L. Zuo, Z. Wang, J. H. Ma, and L. Xi, J. Mater. Sci. Technol. **29**, 245 (2013).

[31] B. Lv, Z. Lian, Y. Miao, C. Gao, M. Si, D. Xue, F. Yu, and J. Yao, Appl. Phys. Lett. **116**, 132404 (2020).

[32] T. Kojima, S. Kameoka, and A.-P. Tsai, ACS Omega **2**, 147 (2017).

[33] S. Husain, A. Kumar, S. Akansel, P. Svedlindh, and S. Chaudhary, J. Magn. Magn. Mater. **442**, 288 (2017).

[34] A. Kumar, F. Pan, S. Husain, S. Akansel, R. Brucas, L. Bergqvist, S. Chaudhary, and P. Svedlindh, Phys. Rev. B **96**, 224425 (2017).

[35] P. J. Brown, A. G. Fox, E. N. Maslen, M. A. O’Keefe, and B. T. M. Willis, Int. Tables Crystallogr. **C**, 554 (2006).

[36] H. P. Klug and L. E. Alexander, *X-Ray Diffraction Procedures: For Polycrystalline and Amorphous Materials* (1974).

[37] P. Innocenzi, P. Falcaro, D. Grosso, and F. Babonneau, J. Phys. Chem. B **107**, 4711 (2003).

[38] A. Borba, J. P. Vareda, L. Durães, A. Portugal, and P. N. Simões, New J. Chem. **41**, 6742 (2017).

[39] D. J. Rosenberg, S. Alayoglu, R. Kostecki, and M. Ahmed, Nanoscale Adv. **1**, 4878 (2019).

[40] G. Jian, Y. Liu, X. He, L. Chen, and Y. Zhang, Nanoscale **4**, 6336 (2012).

[41] P. de la Presa, Y. Luengo, M. Multigner, R. Costo, M. P. Morales, G. Rivero, and A. Hernando, J. Phys. Chem. C **116**, 25602 (2012).

[42] R. Hiergeist, W. Andrä, N. Buske, R. Hergt, I. Hilger, U. Richter, and W. Kaiser, J. Magn. Magn. Mater. **201**, 420 (1999).

[43] F. Shubitidze, K. Kekalo, R. Stigliano, and I. Baker, J. Appl. Phys. **117**, 94302 (2015).

[44] J. S. Anandhi, T. Arun, and R. J. Joseyphus, Phys. B Condens. Matter **598**, 412429 (2020).

[45] N. A. Usov, R. A. Rytov, and V. A. Bautin, Sci. Rep. **11**, 6999 (2021).

[46] M. R. Karim, S. N. Panda, A. Barman, and I. Sarkar, Nanotechnology **33**, 235701 (2022).

# Chapter 6

## *Growth, magnetic and hyperthermia property study of $L2_1$ ordered $Co_2FeAl$ Heusler nanoparticles*

$Co_2FeAl$ is an extremely important class of cobalt iron based Heuser material that has been widely studied in thin film and bulk. There is an urgent need to develop nanoparticle of $Co_2FeAl$ that has been mostly restricted to A2 disordered phase. Here we report growth of less than 10 nm size well ordered crystalline $Co_2FeAl$ nanoparticles having $L2_1$ type of ordering. We further study its magnetic property that shows high saturation magnetization value of 190 emu/gm. Through these measurements we estimate their internal Neel and diffusive Brownian relaxation time. Hyperthermia measurements are carried out to evaluate their heat generation capability under oscillating magnetic field.

## 6.1 Introduction:

Cobalt iron based Heulser alloys are an important class of intermetallic alloys due to its possible spintronic applications. In this class of materials $Co_2FeAl$ is considered to be one of the unique system that has useful properties like high spin polarization, high saturation magnetization, high transition temperature and large magnetic anisotropy [1]. These useful properties have led to extensive studies on thin films of $Co_2FeAl$ for possible use in magneto resistive device structures [2–5]. There has been considerable interest in developing Heulser nanoparticles especially those of $Co_2FeX$ (X being sp-element). Recently giant magnetocaloric effect has been reported in disordered $Co_2FeAl$ nanoparticles having a size of about 16 nm, wherein a huge change in entropy has been observed during transition from ferromagnetic (FM) to paramagnetic (PM) state around 1250 K [6]. This opens an important question of exploring other useful magneto thermal effects such as hyperthermia that may be significant in $Co_2FeAl$ in the magnetically ordered state below the FM to PM transition temperature.

Magnetic nanoparticles are known to release heat under application of alternating or oscillating magnetic field [7–12]. The heat released is associated to change in internal energy as magnetization lags in following the variation of magnetic field [13,14]. This property is useful for applications like hyperthermia which is related rise of temperature of ferrofluids containing magnetic nanoparticle due to heat release under oscillating magnetic field [15]. Recently hyperthermia measurements on partially ordered $Co_2FeSn$ based nanoparticles have shown high rate of heat generation [16]. Therefore it is intriguing to explore the possibility of heat generation using $Co_2FeAl$ nanoparticles in oscillating magnetic field.

The degree to which magnetic nanoparticles can generate heat in presence of time varying magnetic field depends upon the rate of relaxation of magnetic moments. The magnetic moment of nanoparticles dispersed in ferro fluid undergoes two kind of rotations in presence of oscillating magnetic field. The application of magnetic field can lead to diffusive rotation of the complete nanoparticle along with internal rotation of magnetic moment within the nanoparticle itself. The former rotation leads to Brownian relaxation and the later to Neel relaxation [17]. The two relaxation process adds up to give the effective magnetic relaxation in the nanoparticles. The rate of heat release strongly depends on the effective magnetic relaxation time. Therefore it is useful to estimate the Neel relaxation time ($\tau_N$) and Brownian relaxation time ($\tau_B$) of the magnetic nanoparticles.

A major problem in development of Heusler nanoparticles is to attain good crystalline and chemical order with minimal atomic site mixing of constituent elements. There has been reports on partially ordered $Co_2FeX$ Heulser nanoparticles that includes $Co_2FeGa$ [18–20], $Co_2FeSn$ [16], and $Co_2FeGe$ [21]. Using coprecipitation method disordered A2 type $Co_2FeAl$ nanoparticles has been prepared of size ranging between 50-400nm [22] and around 16nm [6,23] having saturation magnetization value of 135 emu/g and 180 emu/g respectively. A2 type disorder in Heulser structures of type $X_2YZ$ corresponds to atomic site mixing among all constituent elements [24,25]. There has been also reports on growth of A2 type disordered $Co_2FeAl$ nanoparticles of size more than 10 nm using hydrothermal method [26] and thermal decomposition method [27,28]. Interestingly, A2 type $Co_2FeAl$ antiparticles have been also functionalized for effcient detection of SARS COV-2 [29]. Hollow A2 disordered $Co_2FeAl$ nanoparticles capped with polyethylene glycol (PEG) has been also reported [29].

Here we report growth, magnetic property and hyperthermia studies on less than 10 nm size $Co_2FeAl$ nanoparticles capped with PEG. The nanoparticles show good crystalline quality with $L2_1$ ordering which indicates no mixing of atomic sites of constituent element. The nanoparticles show high saturation magnetization and a large magnetic anisotropy constant. The saturation magnetization is found to be larger than those reported for A2 disorderd nanoparticles [6,23] Furthermore we estimate the Brownian relaxation and Neel relaxation time scales of these Heulser nanoparticles. The results show that the size and the magnetic property of these nanoparticles are such that $\tau_B$ about two orders of magnitude higher than $\tau_N$. Furthermore hyperthermia studies on the $L2_1$ ordered nanopartcles reveal that these Heusler nanoparticles can effciently generate heat under alternating magnetic field.

## 6.2 Experimental methods:

$Co_2FeAl$ nanoparticles were grown using co-precipitation method using PEG as capping agent followed by and thermal annealing. The synthesis was carried out by first preparing a precursor solution of all the metal ions, i.e. Co, Fe and Sn. For this $CoSO_4 .7H_2O$ (1.8 mmol), $FeSO_4 .7H_2O$ (1 mmol), and $Al_2(SO_4)_3$ (1 mmol) were dissolved in 5 mL of distilled water and was stirred for 15 minutes for homogeneous mixing. Separately a solution of 2gm PEG (molecular weight 600 gm/mole) in 5 ml distilled water was prepared. The PEG solution was added drop wise to the precursor solution. The mixed solution was stirred for 10 hours. For the co-precipitation of metal ions, the pH of the mixed solution was adjusted to 9 by slowly dropping 12 mmol NaOH solution (prepared in 80 mL distilled water). The pH controlled solution was stirred for 16 hours followed by filtering and washing several times in distilled water to obtain residue. The residue obtained was dried at 80 °C for 3 hours. The dried residue was gently grinded to get the fine and homogenous powder. The powder was deoxidized by annealing at 900 °C in 20% balanced hydrogen and argon gas mixture. The sample grown at 9 pH and at 900 °C showed partial signature of $L2_1$ ordering. Growth of nanoparticles in carried out at lower or higher than 9 pH led to disordered Heuser phase. These results are later discussed in details. Figure 6.1 describes the pathway to synthesis the $Co_2FeAl$ nanoparticles.

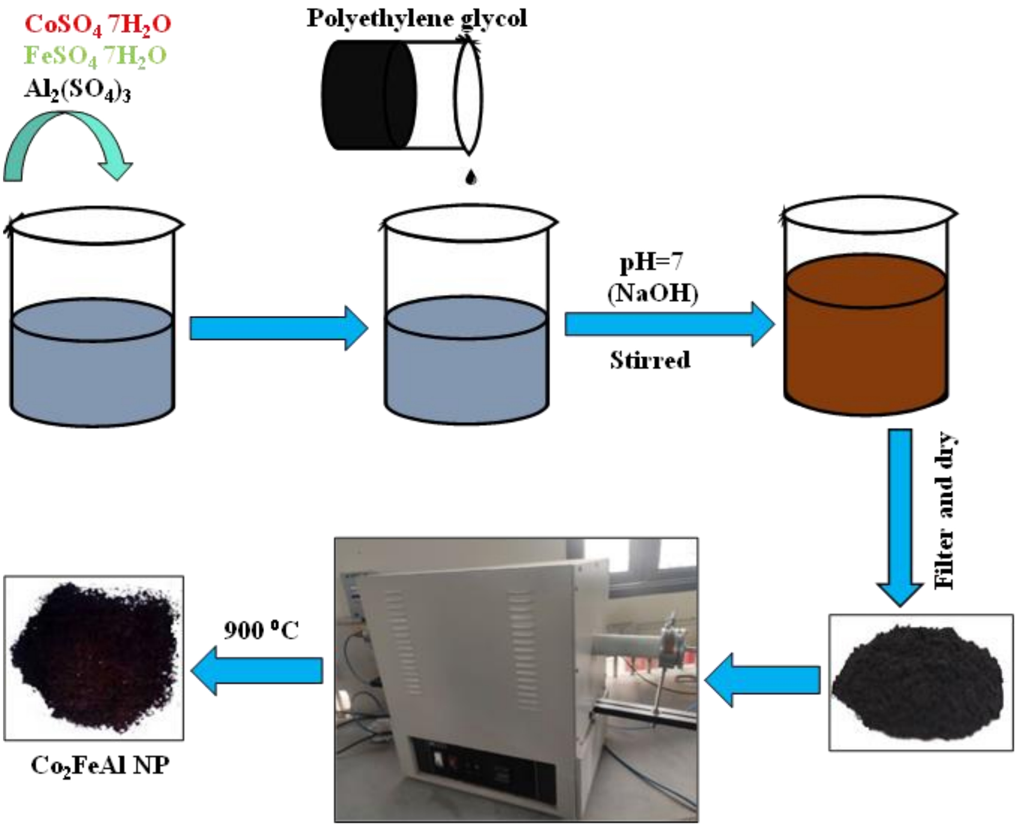

***Figure 6.1:*** *Systematic way to synthesis the ordered $Co_2FeAl$ nanoparticles.*

X-ray diffraction (XRD) measurements were carried out using a Bruker D8 Advance diffractometer equipped with Cu Kα X-ray source. High-resolution transmission electron microscopy (HRTEM) images were taken using a JEOL JEM 2100 TEM operating at

200 kV acceleration voltage. DC magnetization studies were performed using magnetic property measurements system (Evercool SQUID, Quantum Design) equipped with super conducting quantum interference device (SQUID). Temperature dependent magnetization data was recorded by employing zero field cooled (ZFC) and field cooled (FC) measurement protocol by cooling the sample in absence and presence of 200 Oe magnetic field, respectively. To evaluate the heat generation efficiency of the Heusler nanoparticles, magnetic hyperthermia efficiency was measured using DM2-DM100 nano-magnetic heating system setup (nB nanoscale Biomagnetics, Zaragoza, Spain). For the hyperthermia measurements an aqueous colloidal solution (1mg/ml) of the nanoparticles was prepared. The data was measured by applying AC magnetic field at 380 kHz while recording the time dependence of the rise of temperature of the magnetic colloidal solution using an integrated fluoro-optic thermometer fiber probe. The hyperthermia or heat generation efficiency was measured in terms of the specific absorption rate (SAR). SAR is defined as the power dissipation per unit mass of magnetic nanoparticle (W/g), and is given as [31,32]:

$$SAR = \frac{C}{m}\frac{dT}{dt} \tag{6.1}$$

where, C represents the specific heat of the solution which for these measurements is assumed to be same as that of pure water (C = 4.185 J/g/K). dT/dt is the initial rate of rise of temperature and is obtained from the initial slope of the temperature vs. time graph and m is the weight of the nanoparticles in the solution.

## 6.3 Results and Discussion:

### 6.3.1 Structural analysis and morphology

Figure 6.2 (a)-(c) shows X-ray diffraction (XRD) data for the nanoparticles grown at different pH conditions. All the nanoparticles show presence of three peaks around 44.8°, 65.2° and 82.8°, corresponding to [220], [400] and [422] Bragg reflection of $Co_2FeAl$ Heuser compound [6]. These three reflections are well known to prominently appear in $Co_2FeX$ (X is a sp-element) type of FHAs [20, 22, 31]. The XRD data (Fig. 6.2-(a)) of the sample grown at 8 pH is typical of A2 disordered Heuser phase of $Co_2FeAl$ [23]. The nanoparticles grown at 10 pH shows additional diffraction peaks (marked by arrows in Fig. 6.2-(b)) beyond those belonging to the Heusler phase, indicating poor growth quality. Interestingly the nanoparticles grown at pH 9 shows an additional peak at 26.5°.

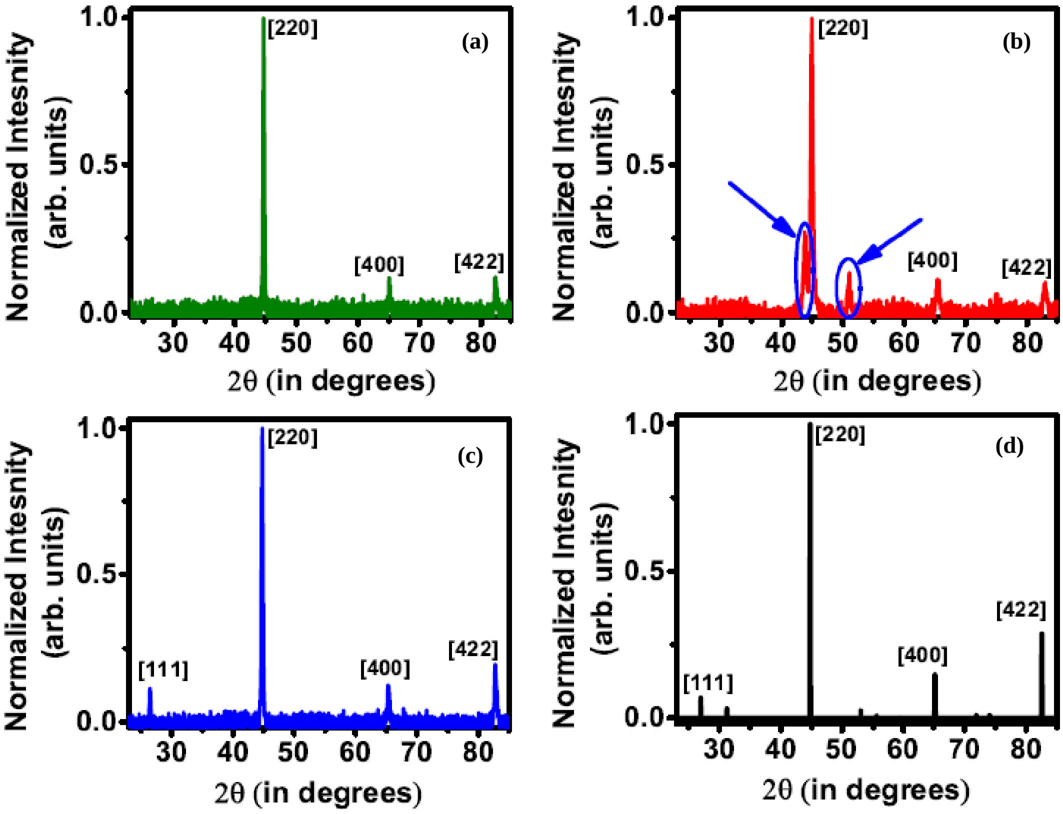

***Figure 6.2:*** *Normalized XRD data of $Co_2FeAl$ nanoparticles grown at (a) 8 pH (b) 10 pH and (c) 9pH. The normalization is with respect to the most intense peak of [220] reflection. (d) Normalized XRD data simulated for B2 ordered $Co_2FeAl$ having lattice parameter of 5.72 Å.*

This peak at around 26.5° corresponds to [111] Bragg reflection of $Co_2FeAl$ [33]. The [111] Bragg reflection is known to appear only in $L2_1$ ordered Heusler phase and not in A2 disordered phase [32]. This indicates $L2_1$ ordering in the nanoparticles grown at 9 pH. The XRD peaks measured are in confirmation of the corresponding Bragg reflections found in the powder diffraction simulation of an $L2_1$ ordered $Co_2FeAl$ having lattice parameter of 5.72 Å. The simulation is done using powdercell program [34]. In the simulation Co, occupies Wyckoff positions of 8c with the crystal having Fm3m space group symmetry. Atoms of Fe and Al are assumed to occupy 4a and 4b positions respectively.

Figure 6.3 shows HRTEM images of the nanoparticles grown at 9 pH and that exhibit $L2_1$ ordering. The average size of the nanoparticles is ≈ 8nm (Fig. 6.3-(b)). The high resolution image (Fig. 6.3-(c)) show clear lattice fringes indicating high crystalline quality of the nanoparticles.

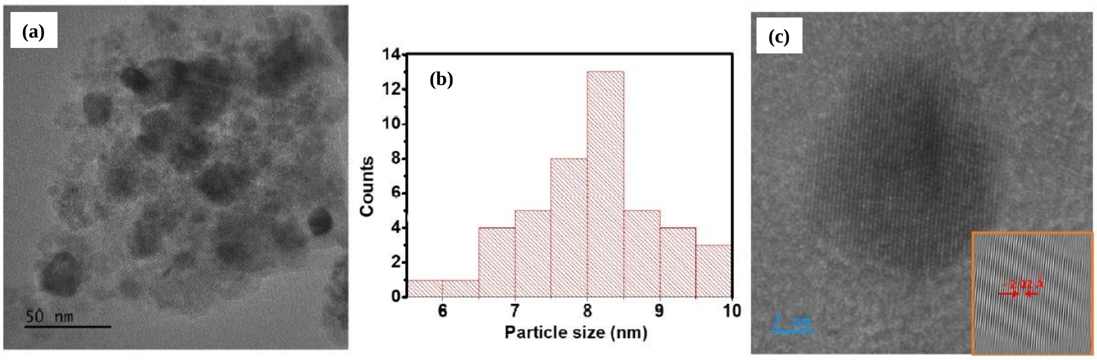

***Figure 6.3:*** *(a) HRTEM image of $Co_2FeAl$ nanoparticles grown at 9 pH. (b) Size distribution analysis of $Co_2FeAl$ nanoparticles. (c) High resolution TEM image clearly showing presence of lattice fringes revealing the highly crystalline nature. The inset shows inverse fast Fourier transform pattern of an area selected over the lattice fringes.*

The inverse fast Fourier transform (inset Fig. 6.3-(c)) of the HRTEM image of the nanoparticle shows fringes corresponding to an inter-planar spacing of $\approx$ 2.02 Å between [220] planes of $Co_2FeAl$ which is consistent to the XRD data.

### 6.3.2 DC magnetization study

DC magnetization measurements were carried out to study the magnetic property of the $L2_1$ ordered nanoparticles. The ZFC-FC plot (Fig. 6.4-(a)) for the nanoparticles show clear branching between ZFC and FC data. The branching temperature was above room temperature and beyond the measurement range of 400 K. This is a signature that the magnetic transition temperature of these nanoparticles are higher than 400 K. This is consistent with the fact that $Co_2FeAl$ has high Curie temperature of 1250 K in bulk [6]. The branching of ZFC-FC indicates a blocked magnetic state for nanoparticles wherein the orientation of magnetic moment is frozen in a stable state against thermal fluctuation [35,36]. The isothermal field dependent magnetization measurements at 300 K (Fig. 6.4-(b)) shows opening of a hysteresis with coercive field of 150 Oe. The coercive field is seen to increase up-to 250 Oe at 10 K (Fig. 6.4-(c)). The magnetization versus field plot (Fig. 6.5) recorded up-to high magnetic field shows a large saturation magnetization value of 190 emu/gm at 300K. The $M_S$ value is higher than those reported earlier for disordered $Co_2FeAl$ nanoparticle [6,23].

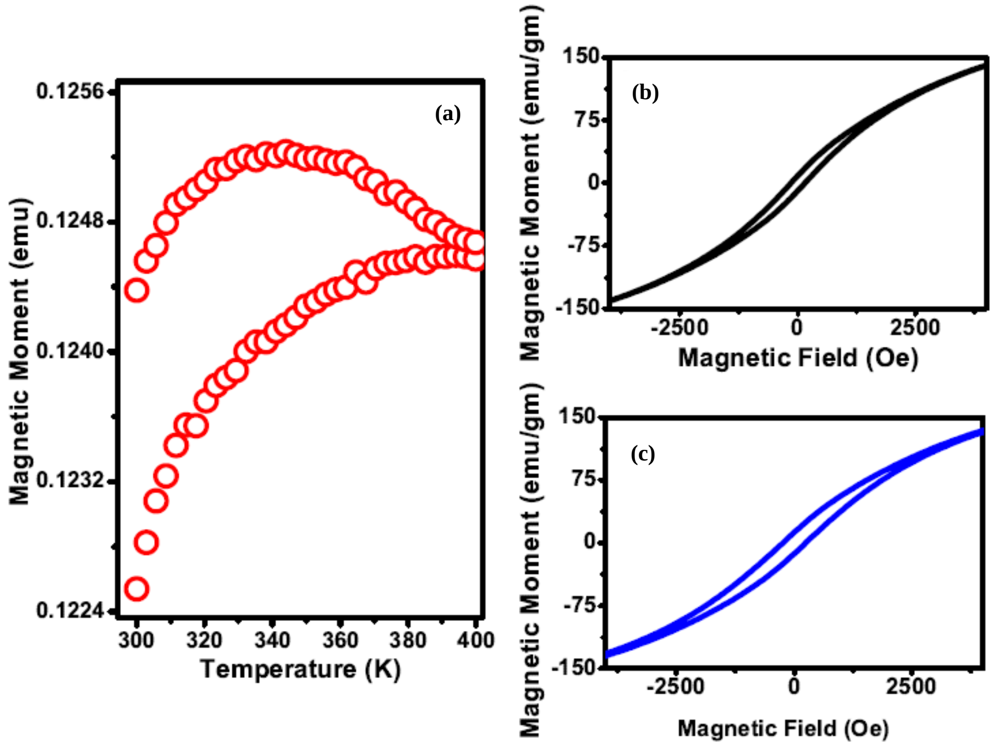

***Figure 6.4:*** *(a) ZFC-FC plot of magnetization vs temperature for $L2_1$ ordered $Co_2FeAl$ nanoparticles prepared at 9 pH. The measurements were done under 200 Oe magnetic field. Isothermal hysteresis measurements $L2_1$ ordered $Co_2FeAl$ nanoparticles recorded at (b) 300 K and (c) 10 K.*

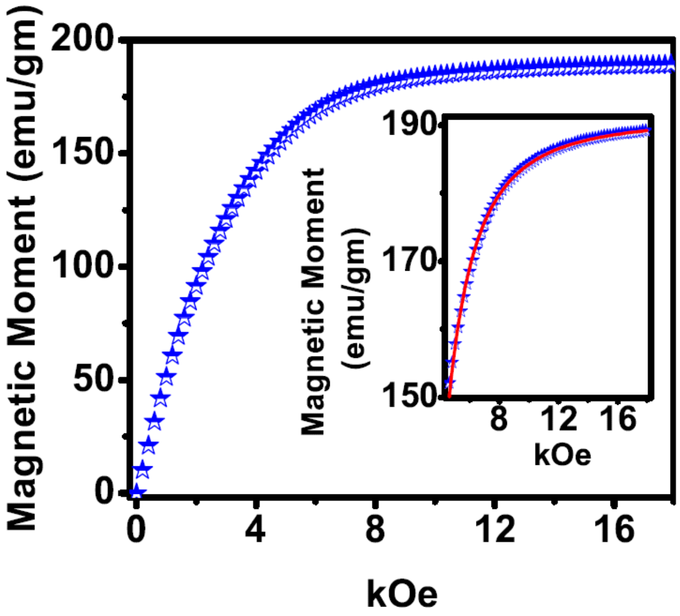

***Figure 6.5:*** *Magnetization versus magnetic field data taken up-to saturation field for $Co_2FeAl$ nanoparticles. The inset shows the high field data. The line shows the fit to the data using eqn. 6.2.*

The magnetic anisotropy (K) of the Heusler alloy nanoparticles can be obtained by fitting the high field magnetization versus field data using the equation [20,37]:

$$M(H) = M_S\left(1 - \frac{0.07619K^2}{H^2M_S^2} - \frac{0.0384K^3}{H^3M_S^3}\right) + \chi_P H \tag{6.2}$$

where, $M_S$ is the saturation magnetization, and $\chi_P$ is high field paramagnetic susceptibility. The fit yields a value of 1.074 X $10^5$ J/m$^3$. The temperature dependence of the anisotropy constant (Fig. 6.6) shows a decrease with increasing temperature. This is consistent to the earlier observation of reduction of K with increase in temperature in cobalt ferrite nanoparticles [37,38]. Using the values obtained for anisotropy constant and an average size ( ≈ .8nm) for the nanoparticles as obtained from TEM measurements, the Neel relaxation time was calculated using the relation $\tau_N = \tau_0 \frac{KV}{K_BT}$ [39]. Here, $V$ is the volume of nanoparticle and $\tau_0$ is of the order of $10^{-9}$ s - $10^{-10}$ s. This leads to a Neel relaxation time of $\tau_N \approx 6.7 \times 10^{-7}$ s.

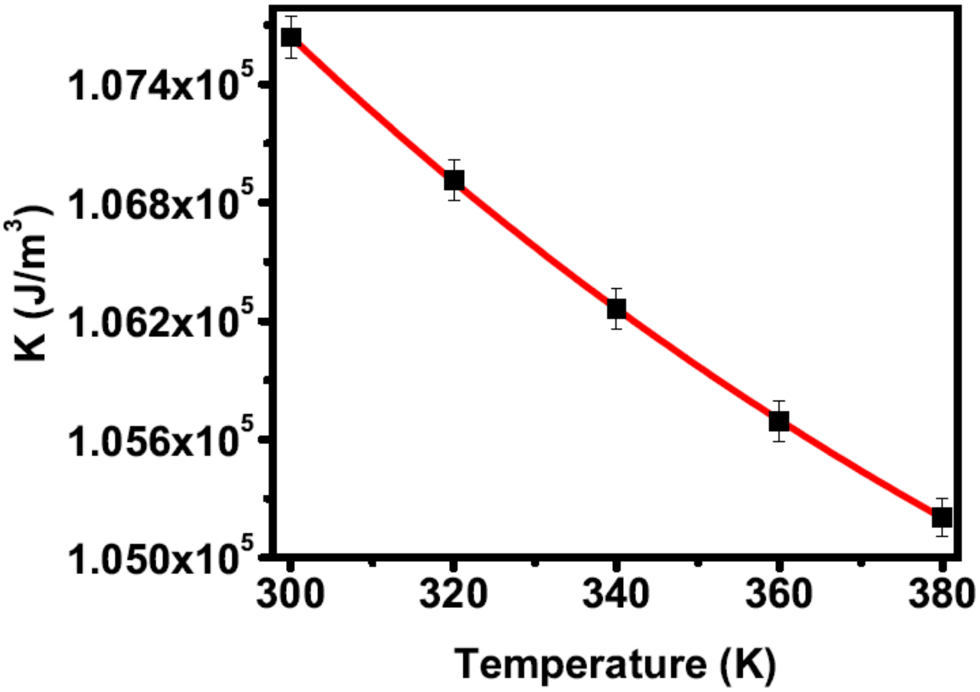

***Figure 6.6:*** *Temperature dependence of anisotropy constant of L2$_1$ ordered Co$_2$FeAl nanoparticles. Solid line is guide to the eye.*

In order to compare this with the Brownian relaxation time of these nanoparticles in water, the corresponding relaxation time $\tau_B$ was calculated using the relationship [40].

$\tau_B = \frac{3\eta V_H}{K_B T}$, here $V_H$ is the hydrodynamic volume of the nanoparticles in the aqueous solution and η is the viscosity coefficient of water. The hydrodynamic size was obtained by carrying out DLS measurements on the aqueous solution of the $Co_2FeAl$ nanoparticles dispersed in water. The measurements yielded a hydrodynamic particle size of ≈ 60 nm. Using a value of $\eta = 8.90 \times 10^{-4}$ Pa·s for water at room temperature, the corresponding Brownian relaxation time was obtained to be around $2.5 \times 10^{-5}$ s. The high values of relaxation times makes these nanoparticles suitable for heat generation.

### 6.3.3 Hyperthermia measurements

Magnetic hyperthermia measurements were performed to evaluate the heat generation capability of the $L2_1$ ordered $Co_2FeAl$ nanoparticles by applying alternating magnetic field. The measurements were performed on an aqueous colloidal solution (1mg/ml) containing the nanoparticles. Fig. 6.7-(a) shows results of hyperthermia measurements for colloidal solutions containing Heusler nanoparticles measured under an oscillating magnetic field excitation of 370 Oe strength and 387 kHz frequency.

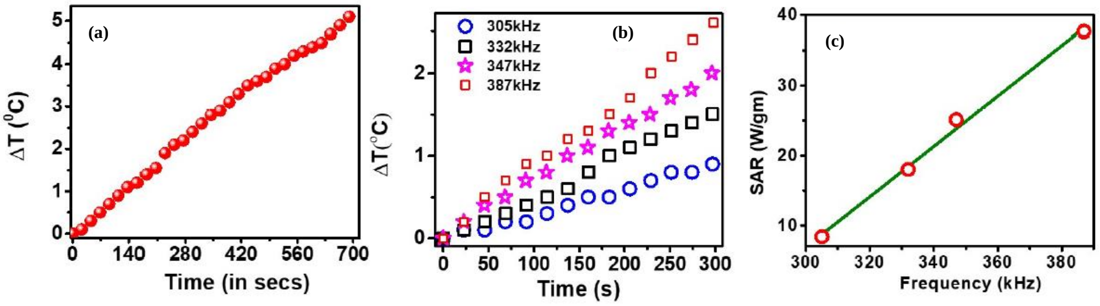

***Figure 6.7:*** *(a) Hyperthermia measurements plot of rise in temperature ΔT versus time measured under application of oscillating magnetic field of 370 Oe strength and 387 kHz. (b) Hyperthermia measurements recorded under application of 370 Oe magnetic field strength for different excitation frequency. (c) SAR value vs Excitation frequency plot. The solid line is guide to the eye that shows a linear dependence on excitation frequency.*

The measurements clearly demonstrate the heat release by the nanoparticles that consequently lead to an increase in the temperature of the colloidal solution. The rise in temperature (Fig. 6.7- (a)) was found to be more than 5 °C after application of field for 700 s. The heat release capacity was found to decrease with decrease in excitation frequency (Fig. 6.7-(b)). A specific absorption rate (SAR) value of about 38 W/g was obtained for the $Co_2FeAl$ Heusler nanoparticles under the application of 380 Oe AC magnetic field at 380 kHz. The SAR value is found to vary linearly as a function of excitation frequency (Fig. 6.7-(c)).

*Table 6.1: Comparison of SAR value with other materials*

| Compounds | Coating | Magnetic Field (Oe) | Frequency (kHz) | SAR value (W/gm) | Ref. |
|---|---|---|---|---|---|
| $Co_2FeSn$ | Silica | 370 | 387 | 120 | [16] |
| $Co_2FeAl$ | PEG | 370 | 387 | 38.5 | This work |
| $Fe_3O_4$ | Chitosan | 335 | 265 | 118.8 | [41] |
| $Fe_3O_4$ | Tetramethyl ammonium hydroxide | 791 | 126 | 135.9 | [42] |
| $Fe_3O_4$ | Lauric acid | 188 | 300 | 120 | [43] |
| $MnFe_2O_4$ | Lauric acid | 188 | 300 | 97 | [43] |
| $CoFe_2O_4$ | Lauric acid | 188 | 300 | 37 | [43] |
| Ag@ $Fe_3O_4$ | brick-like coreshell | 402 | 313 | 100 | [44] |
| $Fe_3O_4$ |  | 157 | 500 | 108 | [45] |
| $Fe_3O_4$ | Oleic acid | 335 | 265 | 91.4 | [46] |

## 6.4 Conclusion:

To summarize the results presented here demonstrates the possibility of growth of $Co_2FeAl$ Heusler nanoparticles of size less than 10 nm and having good crystalline order of $L2_1$ type. The results show that these nanoparticles have high saturation magnetization and high magnetic transition temperature. Hyperthermia studies on these nanoparticles show heat generation capability under the application of oscillating magnetic field. This work provides an opportunity for further development of Heusler compound nanoparticles capable of heat generation for possible magneto-thermal applications.

## 6.5 References:

[1] H. J. Elmers, S. Wurmehl, G. H. Fecher, G. Jakob, C. Felser, and G. Schönhense, Appl. Phys. A **79**, 557 (2004).

[2] W. Wang, H. Sukegawa, R. Shan, S. Mitani, and K. Inomata, Appl. Phys. Lett. **95**, 182502 (2009).

[3] M. S. Gabor, T. Petrisor Jr, C. Tiusan, M. Hehn, and T. Petrisor, Phys. Rev. B **84**, 134413 (2011).

[4] S. Husain, V. Barwal, A. Kumar, R. Gupta, N. Behera, S. Hait, N. K. Gupta, P. Svedlindh, and S. Chaudhary, J. Magn. Magn. Mater. **486**, 165258 (2019).

[5] R. S. Malik, E. K. Delczeg-Czirjak, R. Knut, D. Thonig, I. Vaskivskyi, D. Phuyal, R. Gupta, S. Jana, R. Stefanuik, and Y. O. Kvashnin, Phys. Rev. B **104**, L100408 (2021).

[6] A. Ahmad, S. Mitra, S. K. Srivastava, and A. K. Das, J. Phys. D. Appl. Phys. **54**, 385001 (2021).

[7] J. Kim, J. E. Lee, S. H. Lee, J. H. Yu, J. H. Lee, T. G. Park, and T. Hyeon, Adv. Mater. **20**, 478 (2008).

[8] H. Belkahla, G. Herlem, F. Picaud, T. Gharbi, M. Hémadi, S. Ammar, and O. Micheau, Nanoscale **9**, 5755 (2017).

[9] J. Marbaix, N. Mille, L.-M. Lacroix, J. M. Asensio, P.-F. Fazzini, K. Soulantica, J. Carrey, and B. Chaudret, ACS Appl. Nano Mater. **3**, 3767 (2020).

[10] Ö. Çelik and T. Fırat, J. Magn. Magn. Mater. **456**, 11 (2018).

[11] L.-M. Lacroix, R. B. Malaki, J. Carrey, S. Lachaize, M. Respaud, G. F. Goya, and B. Chaudret, J. Appl. Phys. **105**, 23911 (2009).

[12] B. Mehdaoui, J. Carrey, M. Stadler, A. Cornejo, C. Nayral, F. Delpech, B. Chaudret, and M. Respaud, Appl. Phys. Lett. **100**, 52403 (2012).

[13] C. Muñoz-Menendez, D. Serantes, O. Chubykalo-Fesenko, S. Ruta, O. Hovorka, P. Nieves, K. L. Livesey, D. Baldomir, and R. Chantrell, Phys. Rev. B **102**, 214412 (2020).

[14] J. Leliaert, J. Ortega-Julia, and D. Ortega, Nanoscale **13**, 14734 (2021).

[15] I. Andreu, E. Natividad, L. Solozabal, and O. Roubeau, ACS Nano **9**, 1408 (2015).

[16] M. R. Karim, S. N. Panda, A. Barman, and I. Sarkar, Nanotechnology **33**, 235701 (2022).

[17] S. Ota and Y. Takemura, J. Phys. Chem. C **123**, 28859 (2019).

[18] C. H. Wang, Y. Z. Guo, F. Casper, B. Balke, G. H. Fecher, C. Felser, and Y. Hwu, Appl. Phys. Lett. **97**, 1 (2010).

[19] L. Basit, C. Wang, C. A. Jenkins, B. Balke, V. Ksenofontov, G. H. Fecher, C. Felser, E. Mugnaioli, U. Kolb, S. A. Nepijko, G. Schönhense, and M. Klimenkov, J. Phys. D. Appl. Phys. **42**, 84018 (2009).

[20] P. Nehla, C. Ulrich, and R. S. Dhaka, J. Alloys Compd. **776**, 379 (2019).

[21] T. Kojima, Y. Nakaya, H. Ham, S. Kameoka, and S. Furukawa, RSC Adv. **11**, 18074 (2021).

[22] J. H. Du, Y. L. Zuo, Z. Wang, J. H. Ma, and L. Xi, J. Mater. Sci. Technol. **29**, 245 (2013).

[23] A. Ahmad, S. Mitra, S. K. Srivastava, and A. K. Das, J. Magn. Magn. Mater. **474**, 599 (2019).

[24] T. Graf, C. Felser, and S. S. P. Parkin, Prog. Solid State Chem. **39**, 1 (2011).

[25] M. R. Karim, A. Adhikari, S. N. Panda, P. Sharangi, S. Kayal, G. Manna, P. S. A. Kumar, S. Bedanta, A. Barman, and I. Sarkar, J. Phys. Chem. C **125**, 10483 (2021).

[26] F. Yang, D. Liu, W. Li, P. Xiong, Y. Jia, X. Chen, and C. Yang, J. Alloys Compd. **735**, 1206 (2018).

[27] A. Kumar and P. C. Srivastava, Mater. Sci. **31**, 501 (2013).

[28] L. T. Huynh, S. N. Bonvicini, A. C. Pinon, and S. Trudel, Can. J. Chem. **94**, 367 (2016).

[29] U. R. Dahiya, G. D. Gupt, R. S. Dhaka, and D. Kalyanasundaram, ACS Appl. Nano Mater. **4**, 5871 (2021).

[30] M. Almasi-Kashi, A. Ramazani, S. Alikhanzadeh-Arani, Z. Pezeshki-Nejad, and A. H. Montazer, New J. Chem. **40**, 5061 (2016).

[31] S. Moise, J. M. Byrne, A. J. El Haj, and N. D. Telling, Nanoscale **10**, 20519 (2018).

[32] R. Gupta and D. Sharma, Nanoscale Adv. (2021).

[33] S. Qiao, S. Nie, J. Zhao, Y. Huo, Y. Wu, and X. Zhang, Appl. Phys. Lett. **103**, 152402 (2013).

[34] W. Kraus and G. Nolze, J. Appl. Crystallogr. **29**, 301 (1996).

[35] N. A. Usov and Y. B. Grebenshchikov, J. Appl. Phys. **106**, 23917 (2009).

[36] K. L. Livesey, S. Ruta, N. R. Anderson, D. Baldomir, R. W. Chantrell, and D. Serantes, Sci. Rep. **8**, 1 (2018).

[37] B. H. Liu, J. Ding, Z. L. Dong, C. B. Boothroyd, J. H. Yin, and J. B. Yi, Phys. Rev. B **74**, 184427 (2006).

[38] S. Yoon, J. Magn. Magn. Mater. **324**, 2620 (2012).

[39] J. Leliaert, A. Coene, G. Crevecoeur, A. Vansteenkiste, D. Eberbeck, F. Wiekhorst, B. Van Waeyenberge, and L. Dupré, J. Appl. Phys. **116**, 163914 (2014).

[40] M. T. Rietberg, S. Waanders, M. M. Horstman-Van de Loosdrecht, R. R. Wildeboer, B. Ten Haken, and L. Alic, Nanomaterials **11**, 3396 (2021).

[41] P. B. Shete, R. M. Patil, N. D. Thorat, A. Prasad, R. S. Ningthoujam, S. J. Ghosh, and S. H. Pawar, Appl. Surf. Sci. **288**, 149 (2014).

[42] B. B. Lahiri, S. Ranoo, and J. Philip, Infrared Phys. Technol. **80**, 71 (2017).

[43] P. Pradhan, J. Giri, G. Samanta, H. D. Sarma, K. P. Mishra, J. Bellare, R. Banerjee, and D. Bahadur, J. Biomed. Mater. Res. Part B Appl. Biomater. An Off. J. Soc. Biomater. Japanese Soc. Biomater. Aust. Soc. Biomater. Korean Soc. Biomater. **81**, 12 (2007).

[44] M. E. F. Brollo, J. M. Orozco-Henao, R. López-Ruiz, D. Muraca, C. S. B. Dias, K. R. Pirota, and M. Knobel, J. Magn. Magn. Mater. **397**, 20 (2016).

[45] A. Jordan, T. Rheinländer, N. Waldöfner, and R. Scholz, J. Nanoparticle Res. **5**, 597 (2003).

[46] R. M. Patil, N. D. Thorat, P. B. Shete, S. V Otari, B. M. Tiwale, and S. H. Pawar, Mater. Sci. Eng. C **59**, 702 (2016).

# Chapter 7

## *Conclusion and Future perspectives*

## 7.1 Conclusion:

The Heusler alloys are extremely useful materials due to their exotic properties and possible integration in future generation spintronics devices. This thesis aims to find beyond physical vapor deposition methods for developing Heusler alloy nanostructures that may be useful for spintronics such as magneto optical and magneto thermal applications. To conclude this thesis, consists of two parts. In the first part, development of thin films of an extremely important Heusler material namely $Co_2FeSn$ is being explored and it's magnetic and magneto optical properties have been studied in detail. In the second part, we have developed highly ordered and high crystalline quality $Co_2FeSn$ and $Co_2FeAl$ Heusler nanoparticles. Further we have studied their magnetic and hyperthermia properties for magneto-thermal applications.

The deposition of $Co_2FeSn$ Heusler alloy film is very difficult due to phase segregation and is thermodynamically difficult to prepare. So, in the first part of this thesis, we have successfully developed an electrochemical deposition based method for growing thin films of $Co_2FeSn$. The three step electrodeposition process developed in this thesis leads to a smooth and crystalline thin film on polycrystalline copper substrate. Through a systematic study, the deposition voltage, deposition temperature, molarity of the precursors, stoichiometry ratio, thickness, post-annealing temperatures were optimized in this work. The magnetic and magneto-optical properties of these electrodeposited films has been investigated in detail.

However for application, low roughness and high crystallinity are important consideration. For this, we further developed method to replace the polycrystalline copper substrate with single crystalline silicon substrate. The deposited film show improved morphology and crystalline quality with a finite $L2_1$ ordering. Magneto optic Kerr measurements show Kerr rotation reaching up to a maximum value of $\approx 0.8°$ which is comparable with the films grown by conventional vapor deposition techniques. Samples possess strong uniaxial magneto-crystalline anisotropy. Angle dependent MOKE measurements reveals that two-fold symmetry exists in the electrodeposited Co2FeSn films.

Apart from thin films, growth of highly ordered Heusler nanoparticles is a subject of intense research but has been mostly limited to disordered A2 type nanoparticles. In this thesis we show development of B2 type ordered $Co_2FeSn$ and $L2_1$ type ordered $Co_2FeAl$

nanoparticles. Furthermore the magneto-thermal effect has not been much explored in the Heusler alloy nanoparticles. Here we present for the first time hyperthermia studies to demonstrate the possibility of generating heat under application of oscillating magnetic field using highly ordered $Co_2FeSn$ and $Co_2FeAl$ nanoparticles. The results show that $Co_2FeSn$ has heating rate better than those reported for non Heusler alloy CoFe based nanoparticles.

## 7.2 Future perspectives:

In 2015, H. Atsufumi et al. [1] showed a roadmap for all possible magnetic tunnel junctions and spin-valve junctions using Heusler materials to inject the spin-polarized electrons efficiently into a non-magnet. The fascinating and unusual properties such as half metallicity at room temperature, large perpendicular magnetic anisotropy, small damping constant make them interesting to study their fundamental aspects as well. However, thermodynamic difficulty in preparing many Heusler materials using conventional physical vapor deposition methods and high cost has been a limiting factor in their development. The work in thesis opens up opportunity to explore beyond physical vapor deposition method for developing such Heusler alloy systems

The demonstration of the possibility of generating heat using Heusler alloy nanoparticles through hyperthermia measurements, presented in this thesis brings in a new material class for such applications. These may be used for application like hyperthermia based cancer treatment.

To summarize this thesis presents several new results that promises to open new avenues both for development and application of Heusler alloys.

## 7.3 References:

[1] A. Hirohata, H. Sukegawa, H. Yanagihara, I. Žutić, T. Seki, S. Mizukami, and R. Swaminathan, IEEE Trans. Magn. **51**, 1 (2015).

# Appendix A

## List of publications

[1] M. R. Karim, D. Panda, A. Adhikari, P. Sharangi, P. Mandal, S. Ghosh, S. Bedanta, A. Barman, and I. Sarkar*, **Mater. Today Commun.** 25, 101678 (2020).

[2] M. R. Karim, A. Adhikari, S. N. Panda, P. Sharangi, S. Kayal, G. Manna, P. S. A. Kumar, S. Bedanta, A. Barman, and I. Sarkar*, **J. Phys. Chem. C** 125, 10483 (2021).

[3] M. R. Karim, S. N. Panda, A. Barman, and I. Sarkar*, **Nanotechnology** 33, 235701 (2022).

[4] M. R. Karim, S. Mohanty, S. Bedanta, and I. Sarkar*, (manuscript under preparation).

## List of conferences/workshop attended

[1] AtC-AtG Magnetics Conference 2021 by IEEE magnetics, **Poster Presentation**, August 24th, 2021.

[2] ICTN-KLC-2021 International Conference on Thin Film Nanotechnology, **Poster Presentation**, August 24th – 25th, 2021, IIT Delhi, India.

[3] Physics of Nano Materials (PNM)-2021 National Conference on Quantum materials and devices, **Oral Presentation**, August 20th – 21st, 2021, INST-Mohali, India.

[4] Nano-Day meeting at Institute of Nano Science and Technology, **Poster Presentation**, December 31st, 2021, Mohali, India.

[5] Attended one day workshop on “Vacuum Technology and its application in Optical Science” organized by SPIE IITG student chapter and Pfeiffer Vacuum Association with Department of Physics, IIT Guwahati.

# *Curriculum Vitae*

***MD REJAUL KARIM***

*Ph.D. Research Scholar*
*Institute of Nano Science and Technology (INST) &*
*Indian Institute of Science Education and Research (IISER)*
*Mohali, Punjab, 140306, India*

Md Rejaul Karim completed B.Sc. (H) and M.Sc. Physics in 2013 and 2015 from the Department of Physics, Aligarh Muslim University, UP, India. He joined the Institute of Nano Science and Technology (INST) in August 2018 as a junior research scholar under the guidance of Dr. Indranil Sarkar and registered with the Indian Institute of Science Education and Research (IISER) Mohali for the Ph.D. program. He authored several research articles and presented his research work in several National and International conferences. His research interests includes the synthesis of intermetallic alloys (Heusler alloys), Spintronics based devices, magneto-optical Kerr effect (MOKE), Ferromagnetic resonance (FMR), ultrafast spin dynamics and domain wall study.